Non-rigid medical image registration with extended free form deformations: modelling general tissue transitions

R. Hua

The University Of Sheffield.

A thesis submitted for the degree of

Doctor of Philosophy (PhD)

2016

Non-rigid medical image registration with extended free form deformations: modelling general tissue transitions

Rui Hua

Department of Electronic and Electrical Engineering

The University of Sheffield

A thesis submitted for the degree of

Doctor of Philosophy (PhD)

November, 2016

To my beloved husband, Isaac Castro,

for his valuable comments and support.

Abstract

Image registration seeks pointwise correspondences between the same or analogous objects in different images. Conventional registration methods generally impose continuity and smoothness throughout the image. However, there are cases in which the deformations may involve discontinuities. In general, the discontinuities can be of different types, depending on the physical properties of the tissue transitions involved and boundary conditions. For instance, in the respiratory motion the lungs slide along the thoracic cage following the tangential direction of their interface. In the normal direction, however, the lungs and the thoracic cage are constrained to be always in contact but they have different material properties producing different compression or expansion rates. In the literature, there is no generic method, which handles different types of discontinuities and considers their directional dependence.

The aim of this thesis is to develop a general registration framework that is able to correctly model different types of tissue transitions with a general formalism. This has led to the development of the eXtended Free Form Deformation (XFFD) registration method. XFFD borrows the concept of the interpolation method from the eXtended Finite Element method (XFEM) to incorporate discontinuities by enriching B-spline basis functions, coupled with extra degrees of freedom. XFFD can handle different types of discontinuities and encodes their directional-dependence without any additional constraints.

XFFD has been evaluated on digital phantoms, publicly available 3D liver and lung CT images. The experiments show that XFFD improves on previous methods and that it is important to employ the correct model that corresponds to the discontinuity type involved at the tissue transition. The effect of using incorrect models is more evident in the strain, which measures mechanical properties of the tissues.

Acknowledgement

During this PhD programme, I have enjoyed doing research and meeting wonderful people at CISTIB. First of all, I would like to express my gratitude to my supervisor Prof. Alejandro Frangi for offering me the opportunity to pursue the PhD. I deeply appreciate his helpful guidance and insightful advice throughout the programme. I would like to thank José Pozo for his excellent co-supervision. He has guided me into the world of research, going through technical details with me and helped me to develop a deeper understanding. I will be always grateful to him. I also would like to thank Zeike Taylor, who is a co-author in most of my publications during the PhD. He has provided valuable scientific inputs and helped to reformulate my article writing to be more comprehensive.

I would like to thank all CISTIB staff for their support and help. I am grateful to my all colleagues who are wonderful companies. I have spent a lot of great moments with Matthias, Serkan and his wife Meva, Helena and Miguel in the fun gaming nights. I would like to thank Ed, Nishant and Chris for memorable get-togethers. Above all, I sincerely thank my husband, Isaac, who has always been by my side and shared this fantastic journey with me.

Finally, I cannot thank enough to my parents, who have always been loving me and believing in me. Without their support and help, I would never be where I am.

DECLARATION

I, Rui Hua, hereby declare that this thesis is the result of my original work and does not include the outcome of work done in collaboration or by other people except where it is specified, acknowledged or cited. I further state that this dissertation as a whole, or part of it, has not been submitted, or, is being concurrently submitted for a degree, diploma or any other qualification at the University of Sheffield or any other University or similar institution.

Part of this thesis have been extracted from a number of publications, all of which were written primarily by the author of this dissertation, Rui Hua, during and as a result of this Ph.D. research. Co-authors provided technical advice, feedbacks on the manuscripts and/or experiments.

Publications

Published Journal articles during the thesis

[1] **Hua, Rui**; Pozo, José M.; Taylor, Zeike; and Frangi, Alejandro F. "Multiresolution eXtended Free-Form Deformations (XFFD) for Non-rigid Registration with Discontinuous Transforms." *Medical Image Analysis*, 36 (2017): 113-122. .

[2] Castro-Mateos, Isaac; **Hua, Rui**; Pozo, José M.; Lazary, Aron; and Frangi, Alejandro F. "Intervertebral disc classification by its degree of degeneration from T2-Weighted Magnetic Resonance Images." *The European Spine Journal*, 25.9 (2016): 2721-2727.

Published Conference papers during the thesis

[3] **Hua, Rui**; Pozo, José M.; Taylor, Zeike A.; and Frangi, Alejandro F. "Discontinuous nonrigid registration using extended free-form deformations." *SPIE Medical Imaging. International Society for Optics and Photonics*, 2015.

[4] Zhang, Le; Gooya, Ali; Bo, Dong; **Hua, Rui**; Petersen, Steffen E.; Medrano-Gracia, Pau; and Frangi, Alejandro F.. "Automated Quality Assessment of Cardiac MR Images Using Convolutional Neural Networks." *International Workshop on Simulation and Synthesis in Medical Imaging*, 2016.

To be published journal articles

[5] **Hua, Rui**; Pozo, José M.; Castro-Mateos, Isaac; Taylor, Zeike A.; and Frangi, Alejandro F. "Anisotropic eXtended Free-Form Deformations (χFFD): A non-rigid registration framework accounting for general discontinuities at tissue transitions." Submitted for publication in *IEEE Transitions on Medical Imaging*.

Contents

List of Figures

List of Tables

List of Abbreviations

COPD . . . . . Chronic Obstructive Pulmonary Disease

CC . . . . . Cross Correlation

CT . . . . . Computed Tomography

DFP . . . . . Davidon-Fletcher-Powell

EBS . . . . . Elastic Body Splines

fast-PD . . . . . fast Primal-Dual

FEM . . . . . Finite Element Methods

FFD . . . . . Free Form Deformation

ITK . . . . . Insight Segmentation and Registration Toolkit

IGRT . . . . . Image-Guided Radiation Therapy

IVD . . . . . Intervertebral Disc

KM . . . . . Kiefer-Wolfowitz

LBFGS . . . . . Limited memory Broyden-Fletcher-Goldfarb-Shanno

LDDMM . . . . . Large Deformation Diffeomorphic Metric Mapping

MI . . . . . Mutual Information

MRF . . . . . Markov Random Fields

MRI . . . . . Magnetic Resonance Imaging

NCC . . . . . Normalised Cross Correlation

NMI . . . . . Normalised Mutual Information

PDE . . . . . Partial Differential Equation

PET . . . . . Positron Emission Tomography

PGM . . . . . Probabilistic Graphical Models

RBF . . . . . Radial Basis Function

RM . . . . . Robbins and Monro

SAD . . . . . Sum of Absolute Differences

SOR . . . . . Successive Over Relaxation

SP . . . . . Simultaneous Perturbation

SPET . . . . . Single-Photon Emission Computed Tomography

SSD . . . . . Sum of Square Difference

TDFFD . . . . . Temporal Diffeomorphic Free Form Deformation

TPS . . . . . Thin-Plate Splines

TRE . . . . . Target Registration Error

XFEM . . . . . eXtended Finite Element Method

XFFD . . . . . eXtended Free From Deformation

Chapter 1

Introduction

1.1 Motivation

Image registration is a fundamental task in image processing. The aim of image registration is to find spatial alignment of corresponding structures between images acquired from different views, with different image modalities, from different subjects, or at different time points. This general objective provides image registration with a wide rage of applications in diverse domains, such as remote sensing [7], computer vision [8] and medical imaging [9].

In the medical field, image registration is an essential tool for a wide range of clinical applications, including image fusion [10], image-guided surgery [10], population study [11], atlas based segmentation [12], motion analysis [13] and longitudinal study [14].

Registration requires a transformation model to describe the type of motion that is allowed in the process of image alignment. The simplest model is rigid, which only allows rotation and translation of rigid objects [15], whereas affine transformation also allows shear and scale [9] and more complex localised deformations can be described by nonrigid models, such as elastic [16], fluid [17] or FFD [18]. Tissue deformations are commonly involved in medical images. Thus, nonrigid registration is widely employed for recovering the motion of tissues or accommodating anatomical variability across individuals.

When images are acquired from the same subject, the anatomical correspondence is expected to represent the same material point, following the motion and deformation of the tissues. In general, conventional non-rigid registration methods are based on the assumption that the deformation field is continuous and smooth across the image. This smoothness constraint is typically imposed by explicit regularisation or a smooth transformation model. However, this assumption is only valid when the properties of the tissues involve continuous variation. In a temporal image sequence, organs or tissues can have different material properties and be bound by different types of contact conditions. When these structures are subject to stretching or compression, different types of discontinuities may occur in the overall deformation field. In that case, the deformation field is not necessarily continuous nor smooth. Imposing continuity and smoothness in the registration will introduce artefacts in the resulting deformations and any quantities derived from it. An important quantity to estimate from registration is strain, which measures tissue elastic properties and is a significant clinical parameter for evaluating the kinetics and functionality of the corresponding organs [19–22]. In addition, strain is sensitive to the correct modelling of discontinuities in the deformation field.

A variety of discontinuities can be present in the underlying deformations of medical images. The type of discontinuities depends on the physical properties of tissue transitions. Despite of the importance of correct modelling of these discontinuities, very little research has been carried out on this direction. Moreover, the models employed in the literature are not based on a physically motivated classification of discontinuities.

1.2 Thesis Aim

The aim of this thesis is to develop a non-rigid registration framework that is able to correctly describe and model the different discontinuity types existing in tissue transitions. Such framework should treat different types of discontinuities correspondingly including the directional properties of those discontinuities.

This aim has led to the development of a registration framework, named eXtended Free Form Deformation (XFFD) with the following objectives:

Physically motivated classification of discontinuities at tissue transitions: Various types of discontinuities may exist in the deformation field. In addition, the discontinuity type can also vary in different directions. The characteristics of discontinuities will be studied and a physically motivated classification will be proposed.

Development of a registration framework handling general tissue transitions: a general registration framework will be developed to handle the various discontinuity types accompanying tissue transitions. Such framework should be able to handle different types of discontinuities in different directions at tissue transitions.

The methods developed during this thesis have been evaluated on digital phantoms mimicking different types of tissue transitions to demonstrate the importance of correct modelling discontinuities. Its applicability on clinical images is illustrated on the publicly available 3D liver CT images, because of the apparent discontinuous motion of the liver and other abdominal organs, such as the kidney. In addition, the DIR-lab dataset [23] of 3D lung CT images is employed, due to the complexity and medical relevance of lung registration. The lungs and the rib cage slide along and have very different material properties. Thus, the discontinuities in lung images exhibit directional dependence at the tissue interface.

1.3 Potential clinical applications

Image registration is crucial for detecting and monitoring abnormalities or diseases to support clinical decisions, diagnosis and treatment planning. Many of these applications require the correct displacements at the interface of tissues with discontinuous deformations.

In general, images registration is employed to extract motion information from medical images, from which a number of clinical relevant parameters can be computed, such as strain. Strain measures local tissue elastic properties, which are important for

many clinically relevant questions [19, 21]. Handling discontinuities incorrectly may introduce artefacts near the tissue interface in the resulting displacement field. Furthermore, errors from these artefacts will propagate to any quantity derived from the displacements, which implies a direct negative impact on the assessment of the tissue functionality and clinical decisions.

Lung images exhibit evident discontinuous deformations at the interface between the lungs and the thoracic cage. Thus, it is important for clinical applications to employ lung motion analysis that handles discontinuities properly. Failing to do so would hamper the accuracy of the clinical parameters. For instance, lung injury is characterised by heterogeneity of regional mechanical properties, which can be assessed by clinical parameters based on the volumetric strain (the determinant of Jacobian) [24, 25]. In addition, Chronic Obstructive Pulmonary Disease (COPD) is a progressive disease that causes an overall decrement in the lung tissue elasticity. The presence of COPD and its severity can be predicted from the local tissue mechanical properties measured by metrics based on image registration [26]. Examples of these metrics are: the Jacobian determinant, strain, and anisotropic deformation index, which measures the magnitude of directional preference in volume change computed from the eigenvalues of the strain [27].

In addition, motion information based on registration, like displacements and strain, can also be employed for the assessment of cardiac diseases and conditions [28, 29], such as cardiac dyssynchrony [30]. In the cardiac images, the myocardium slides along surrounding tissues and is always in contact with the blood, producing continuous displacement field. However, the heart has different material properties from this surrounding structures, which produces different rate of expansion and contraction resulting in discontinuous strain field. Without handling discontinuities in the registration, the strain would be continuous across the interface of the myocardium and its surrounding tissues. This would introduce a smoothing effect that would artificially reduce the cardiac strain near the tissue interface. This would adversely affect any clinical parameter computed from the strain, leading to an adverse impact on the clinical decisions. Thus, discontinuities should be handled in the image registration in order to

obtain realistic cardiac strain.

Another important clinical application of the proposed framework is Image-Guided Radiation Therapy (IGRT), which employs imaging during radiation therapy to improve the precision and accuracy of treatment delivery for the tumour. Registration is used to align the pre-therapy CT image and a treatment planning scan. This alignment affects the radiotherapy field, which should cover the whole tumour and a margin around it for an effective treatment. The aim is to reduce as much as possible the dose in the surrounding healthy tissue to reduce the risk of side effects. For example, radiation fibrosis may develop when normal lung tissue is damaged during radiotherapy [31]. In this case, handling discontinuities is especially important, since registration that simply masks the moving organ cannot provide sufficient information for treatment planning, in which not only the motion of the tumour but also the surrounding tissue should be studied [32].

Finally, the proposed registration method could also be used in the construction of biomechanical models towards personalised medicine. For instance, in the case of the spine, it is necessary to combine the information from different image modalities to characterise the vertebrae, intervertebral discs (IVD) and muscles [33]. However, IVDs are soft tissues whereas vertebrae are bone tissues. Thus, they need to be treated differently in the registration process, while maintaining their attachment. Deforming the IVDs and vertebrae separately will lead to gaps and overlaps between the two structures resulting in unrealistic displacement fields. In contrast, the proposed registration framework can handle discontinuities due to different material properties and, thus, could potentially perform this task straightforwardly.

1.4 Thesis Structure

This thesis has been structured into five chapters.

Chapter 2 introduces the general concepts of image registration, providing alongside an overview of existing methods in general. A more detailed literature review of methods dealing with discontinuity is provided in the methodology chapters (Chapter

3, 4).

Chapter 3 and 4 present the methods in two stages. In Chapter 3, the XFFD framework is developed for the most generic discontinuity type. Other types of discontinuity can be considered as a constrained version of this general type. More complex models for other types of discontinuities will be introduced in the following chapter.

Chapter 4 introduces the complete classification of discontinuity types corresponding to the possible tissue transition properties. Different models are developed and incorporated in XFFD to handle different tissue transitions. This includes modelling all types of discontinuities and incorporating their directional properties.

Chapter 5 discusses limitations and key points of the methodology and provides potential directions of future research.

Chapter 2

Image registration

2.1 Introduction

Image registration is a fundamental task in medical image processing. The aim of image registration is to find point correspondences of anatomical structures between images acquired using different modalities, from different subjects or at different time points.

Over the past 20 years, image registration has undergone remarkable advances. General image registration reviews can be found in [8, 15, 34–36]. For an in-depth explanation of image registration techniques, the reader may consider the books [9, 37]. This chapter aims at providing a broad overview of the existing methods for each of the main components of registration. More specific reviews on registration methods modelling discontinuous deformations are presented in Chapter 3 and 4. This chapter follows a similar structure to the one proposed by Sotiras et al. [36], who provided a very comprehensive survey with advances in image registration until 2013. Notwithstanding, the organization of the chapter has been adapted to include new registration methods.

In the medical field, image registration is an essential tool for a wide range of clinical applications, which can be summarised into the following categories [36]:

Image fusion: The combination of images from different modalities into the same space can provide more information on the patient's anatomy or function [38]. For

instance, CT images provide good visualisation of bone structures and calcified tissues, whereas MRI is more suitable for soft tissues. The most typical fusion (regularly used in the clinics) is of PET or SPET with CT or MRI. As the first step, image fusion requires multimodal registration [39] to align the images [10] (Fig. 2.1).

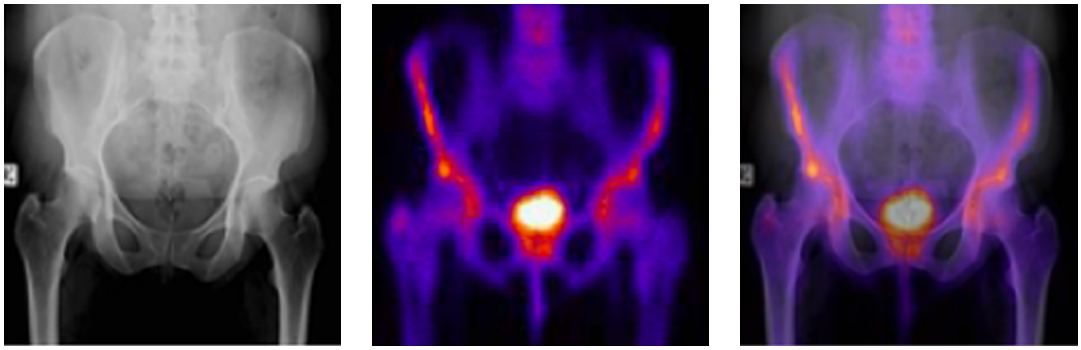

(a) (b) (c)

Figure 2.1: An example of image fusion of hip scans: (a) X-ray image, (b) bone lesion, (c) fused image.

Image-guided surgery: CT and/or MR imaging are often required for planning a surgery, providing high quality 3D images. However, during the intervention, lower resolution modalities, such as 2D ultrasound or X-ray fluoroscopy, are used for real-time imaging. Registration is used in this case to align the high-resolution pre-operative images with the low resolution ones during the intervention to help physician to analyse anatomical changes during the surgery process [40]. This procedure involves registration of images of different dimensions, namely from 3D to 2D [1] (Fig. 2.2).

Population study and statistical models: The analysis of the anatomy or morphological changes of a population can help to identify differences between healthy and unhealthy subjects for future diagnosis, such as age related pathologies in the brain [11] and cardiac motion atlas for coronary heart disease diagnosis [41]. An important requirement for such tasks is the inter-patient registration [42] to obtain point correspondences. Moreover, The population normal variability or the differences due to certain diseases can be encoded by statistical models. Similarly, the generation of shape and appearance statistical models [43] require inter-patient registration.

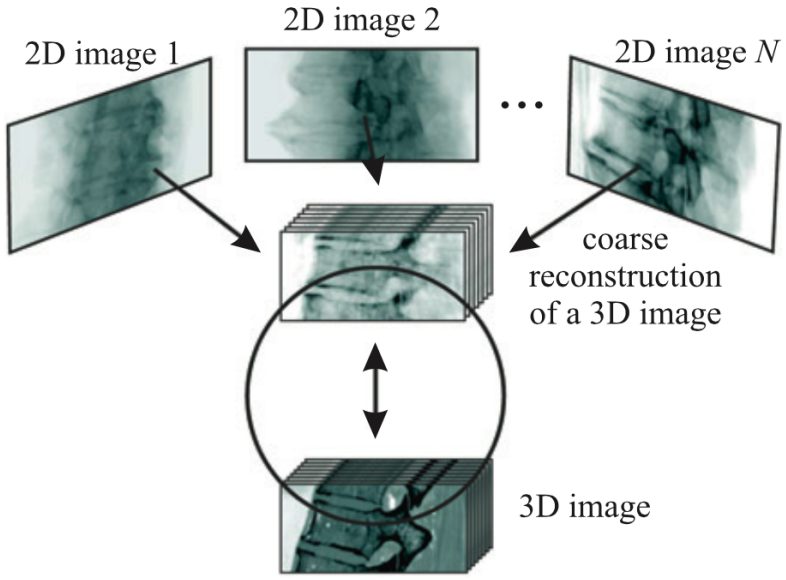

Figure 2.2: 3D/2D registration for image-guided interventions [1]

Atlas based segmentation: Registration can be employed for atlas based image segmentation [12, 44]. This requires one or more images to be initially segmented (the atlas). In order to segment a new case, the segmentations of the atlas are propagated using image registration (Fig. 2.3). In case that the atlas is composed of more than one images, the label of each voxel is determined by fusing the results, for instance, using majority vote [45] or weighted voting [46].

Motion analysis: Image registration can be applied to a temporal image sequence for the analysis of organ motion (Fig. 2.4), which is key in assessing the organ's kinetics and functionality. This has been applied in the motion analysis of organs, such as the heart [3, 47] or lungs [48, 49]. For instance, evaluating regional cardiac wall motion can help to detect structural and functional abnormalities causing heart failure [50], or the analysis of lung motion can be used to assess regional lung function for detecting diseases, such as chronic obstructive pulmonary disease [13].

Longitudinal study: Registration can also be applied on images taken at different time points for monitoring long-term progression of diseases or the follow-up of the outcome of a treatment [14].

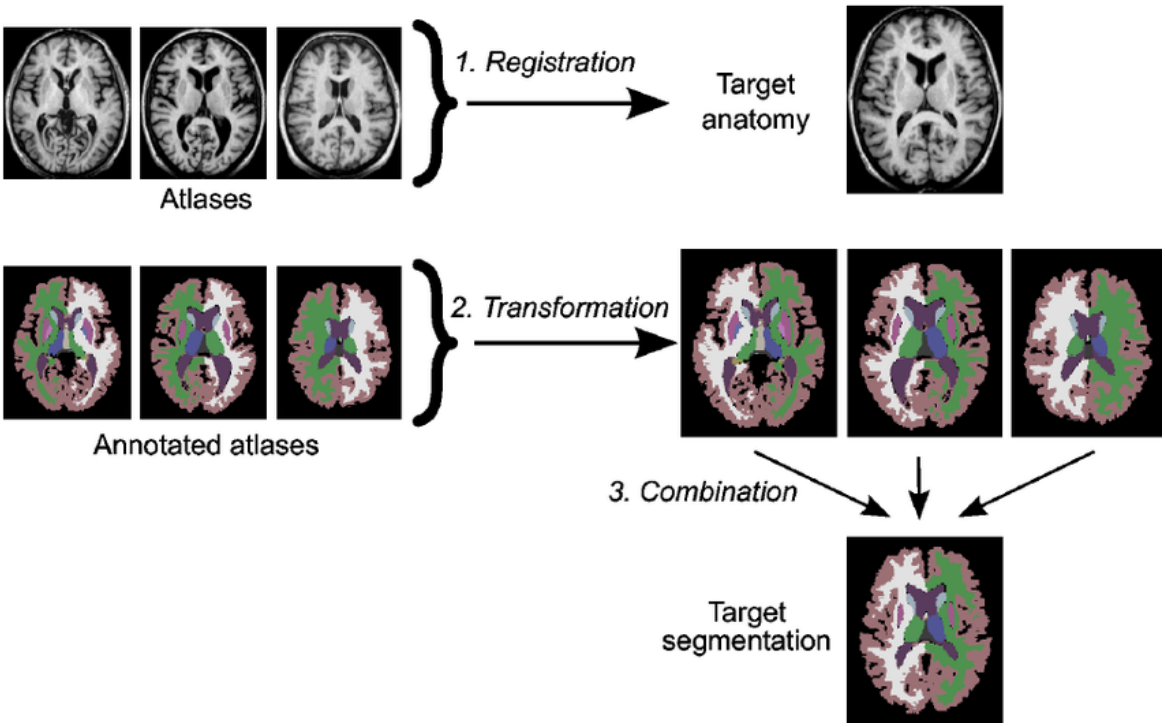

Figure 2.3: An example of the framework for multi-atlas segmentation of brain MR images [2].

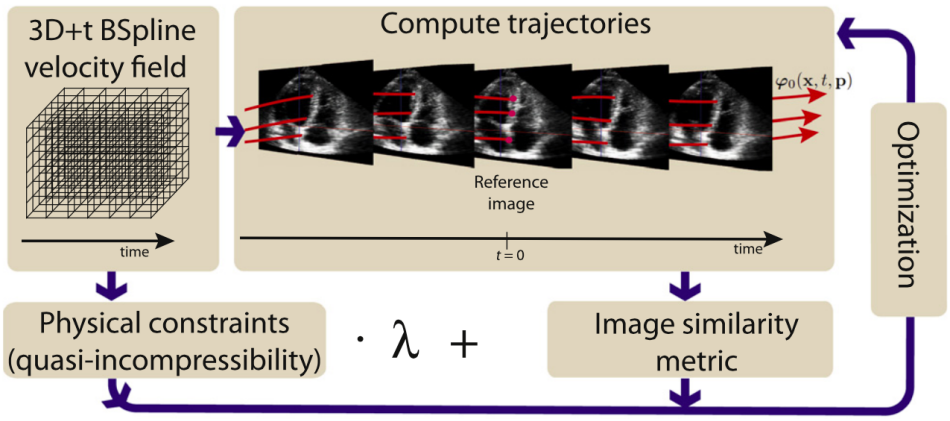

Figure 2.4: An example of temporal image registration for motion analysis. Continuous spatiotemporal trajectories are computed from the 3D+t velocity field, parameterised by a 3D+t grid of control points with B-Spline kernels [3].

2.2 Principles of image registration

The objective of image registration is to establish the optimal transformation between different images, capturing anatomical correspondences between the structures present

in the images. In the simplest case, image registration involves a target image I_t, also known as fixed image, and a moving image, I_m, also referred to as source image

$$\begin{aligned} I_t :\ \Omega_t \to \mathbb{R}, \quad \Omega_t \subset \mathbb{R}^{n_t} \\ I_m :\ \Omega_m \to \mathbb{R}, \ \ \Omega_m \subset \mathbb{R}^{n_m} \end{aligned} \tag{2.1}$$

where n_t and n_m are the spatial dimension of the target and moving image respectively. The idea of registration is to seek the optimal transformation $T : \Omega_t \to \Omega_m$ according to a designed objective function. Thus, the transformed image can be expressed as $I_m \circ T$, where $\circ$ is the composition operator. The transformation at any point $\boldsymbol{x} = (\boldsymbol{x}^1, \boldsymbol{x}^2, ..., \boldsymbol{x}^{n_t})$ is usually described in terms of the displacement field $\boldsymbol{u}(\boldsymbol{x})$

$$T(\boldsymbol{x}) = \boldsymbol{x} + \boldsymbol{u}(\boldsymbol{x})$$

Image registration is usually formulated as an energy minimisation problem with respect to an objective function:

$$-S(I_t,\, I_m \circ T) + \lambda R(T) \tag{2.2}$$

The objective function includes two terms:

- Similarity metric (S): It measures how similar the transformed image is to the target one.
- Regulariser (R): It constrains the transformation to ensure certain properties of the deformation field, such as smoothness. It is weighted by a coefficient, λ.

In general, image registration consists of three components (Fig. 2.5):

- Transformation model: It defines a geometric transformation to map the moving image to the target one.
- Objective function: It consists of a similarity measure and possibly a regulariser.
- Optimisation: it minimises the objective function to achieve the optimal alignment of the images.

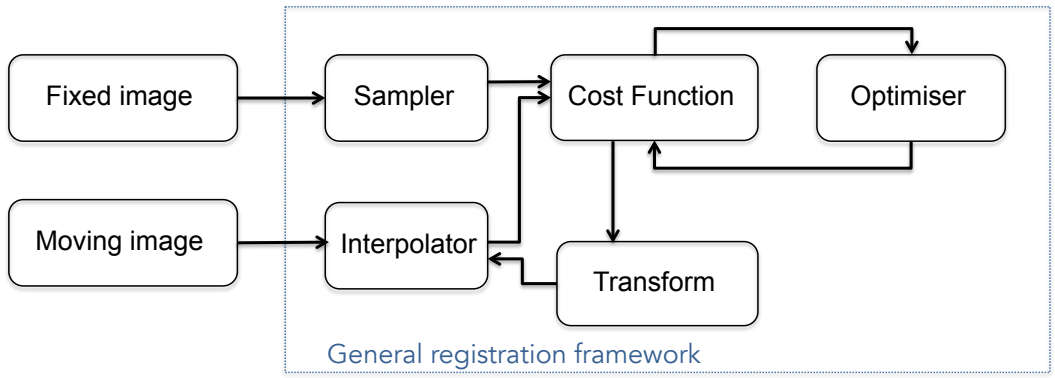

Figure 2.5: A general image registration framework with basic registration components. The complete scheme is annotated by a dashed box. The moving image is going to be deformed to be as similar as possible to the fixed image. The type of deformations are parameterised by the transform model and the cost function is based on a similarity metric with the possible addition of one or more regularisation terms.

The following sections present a review of classical methods together with recent advances in image registration following these four aspects: transformation model, similarity measure, regularisation and optimisation.

2.3 Transformation model

The transformation model determines the class of deformations that are considered for transforming the moving image to match the target one. It restricts the type of acceptable or desired deformations and, thus, limits the search space of possible solutions [51]. The simplest transformation models are used in rigid registration, where no actual deformation is considered, only a global translation and rotation. More general and complex transformation models are considered when non-linear deformations are expected. The number of degrees of freedom in the transformation model is equivalent to the number of parameters to estimate in the optimisation. Higher number of degrees of freedom allows richer description of the deformations. However, this may cause excessive deformations and also increase the complexity of the model, implying higher computational cost and more challenging optimisation problem. For instance, the optimiser may be more likely to get stuck at a local minima in a high-dimensional search space. Therefore, a desirable transformation model should seek a balance between the

descriptive power and computational performance.

Transformation models can be classified, based on the underlying theoretical insight, following similar criteria to the ones proposed in [36, 52] with an extension to include recent advances in image registration. The transformation models are classified into two main categories: 1) physical models; 2) basis function representation.

2.3.1 Physical models

This class of transformation models are based on physical models representing some assumptions on the physical properties and behaviours of the tissues involved. These models can be further divided into four sub-categories following similar classification to that in [53]: 1) elastic models, 2) fluid models, 3) diffusion models, 4) Polyaffine models.

Elastic models

Elastic models consider the moving image as a linear elastic solid, which is deformed under two counteracting forces: 1) the external force that deforms the shape of the object driven by the image similarity measure; 2) the internal force which resists any changes from its equilibrium shape, due to the elastic property of the material. The matching process stops when the two forces reach an equilibrium state, which can be described by Navier linear elastic Partial Differential Equation (PDE) [9]:

$$\mu\nabla^2\boldsymbol{u} + (\lambda+\mu)\nabla(\nabla\cdot\boldsymbol{u}) + \boldsymbol{f} = 0 \tag{2.3}$$

where $\boldsymbol{f}$ represents the external force applied on the elastic body, $\boldsymbol{u}$ the displacement field, and μ and λ denote the Lamé's elastic constants.

This model was first proposed by Broit *et al.* [16] and was later extended to multiresolution by Bajscy and Kovačič [54]. Davatzikos *et al.* [55] modelled the moving image as inhomogeneous elastic objects by employing spatially varying elasticity properties. This allows different tissues to deform to different extent. For instance, the brain ventricles are allowed to deform more freely than other stiffer structures in the

images.

The main drawback of the linear elastic models is that they cannot handle large deformations. To mitigate this weakness, nonlinear elastic models were proposed. Rabbitt *et al.* [56] modelled the moving image as hyperelastic materials, which allows large magnitude material deformations. The nonlinear equations are solved by local linear approximation using finite element method.

Later, the elastic registration was studied as an energy minimisation problem employing elastic energy as regularisation. Droske *et al.* [57] adopted nonlinear elastic energy as a regularisation term. Pennec *et al.* [58] adopted St Venant-Kirchoff elasticity to account for nonlinear elastic deformations and employed log-Euclidean metrics instead of Euclidean ones ensuring inverse-consistency. Recently, Burger *et al.* [59] proposed a hyper elastic regularisation to ensure diffeomorphic and mass-preserving transformations.

Fluid models

A main limitation of the linear elasticity model is its assumption of small deformations. In contrast, fluid models overcome this limitation by representing the moving image as a viscous fluid. The deformations are described by the Navier-Stokes equation [17]:

$$\mu\nabla^2\boldsymbol{v} + (\lambda+\mu)\nabla(\nabla\cdot\boldsymbol{v}) + \boldsymbol{f} = 0 \tag{2.4}$$

where $\boldsymbol{v} = (x, y, z)$ describes the velocity field in a 3D case. This equation is similar to Equation (2.3) but it considers the velocity field instead of the displacement field. The resulting displacements can be estimated by integrating the velocities over time.

Equation (2.4) can be solved using successive over realaxation (SOR) [17]. Bro-Nielsen *et al.* [60] presented a faster implementation using a convolution filter assuming constant viscosity. However, this assumption does not always hold true. To overcome this limitation, Lester *et al.* [61] proposed a fluid model with spatially-varying viscosity to allow different degrees of deformations in different tissues in the image.

Beg *et al.* [62] proposed Large Deformation Diffeomorphic Metric Mapping (LDDMM) method. In LDDMM, deformations are modelled by time dependent velocity

field according to Euler-Lagrange equations. The cost function employs geodesic image metric and a smoothness regulariser and it is minimised by gradient descent. By employing time-varying velocity field, LDDMM allows the estimation of large deformations. However, it has high computational cost and memory demands. An alternative to improve the computational efficiency is to decrease the number of degrees of freedom by employing stationary velocity field. Arsigny *et al.* [63] employed stationary velocities that belong to the Log-Euclidean space. This allows the computation of vectorial statistics of deformations in a well studied space that also guarantees their invertibility. Based on this method, Vercauteren *et al.* [64] proposed LogDemons algorithm, which is computationally more efficient. LogDemons allows all the computation of vectorial statistics in the log-Euclidean space without the need of using the log and exponential mappings as required in [63].

Diffusion models

Thirion *et al.* [65] proposed a diffusion model, considering the deformation process as a diffusion process, which is modelled by the equation:

$$\triangle \boldsymbol{u} + \boldsymbol{f} = 0 \tag{2.5}$$

This model was inspired by Maxwell's Demons in thermodynamics. The basic idea is that each point of an object in the moving image can be determined as inside or outside the same object in the target image. Demons are effectors situated at the object boundary to push the outside points into the object, and to pull the inside points outside the boundary. The forces are based on optical flow [66, 67], which was developed to recover motion between objects in two images in a temporal sequence, assuming constant intensities of the objects along time.

The Demons method was remarkably faster than elastic and fluid registration methods at that time. However, it lacked a sound theoretical justification. Pennec *et al.* [68] investigated nonrigid registration as an optimisation problem and showed that Demons method is equivalent to a second order gradient descent on the similarity measure of the sum of square difference (SSD) with a Gaussian smoothing regulariser. This work

shed insight on Thirion's algorithm, which led to a large number of extensions of the method. A set of the most well-known extensions are: Vercauteren *et al.* endowed Demons method with symmetric [64] and diffeomorphic properties [69]. Stefanescu *et al.* [70] proposed adaptive smoothing to account for varying elasticity of different tissues. Mansi *et al.* [71] developed the logDemons algorithm [64] to ensure incompressible deformations.

2.3.2 Basis function models

Instead of being described by physical models, transformations can also be modelled by a set of basis functions based on interpolation or approximation theory. Unlike employing a dense deformation field as in physical models, basis function models employ much fewer degrees of freedom. In this class, some models describe deformations by basis functions, which are normally continuous and smooth, producing smooth deformation field. In other models, displacements are recovered in limited locations in the image and a dense displacement field can be obtained by interpolation. These models can be further classified into four sub-categories following [36]: i) Radial Basis Functions, ii) Elastic Body Splines, iii) Free-Form Deformations iiii) polyaffine.

Radial Basis Functions

In Radial Basis Function (RBF), the interpolation value of a point $\boldsymbol{x}$ is computed based on its distance from the landmarks $\boldsymbol{x}_i$

$$\boldsymbol{u}(\boldsymbol{x}) = \sum_{i=1}^{N} \omega_i \phi(\|\boldsymbol{x} - \boldsymbol{x}_i\|) \tag{2.6}$$

where ω_i are weights, obtained by solving a set of linear equations [72,73]. In general, RBFs have global support and allow irregular landmark locations. However, their global support requires sufficient landmarks to describe local deformations.

Bookstein *et al.* [74] employed Thin-Plate Splines (TPS) for landmark-based image registration. TPS is the most commonly used RBF [8]. It minimises the bending energy of splines assuring smooth deformations. The main drawback of these

models is that they have global support, which hinders its capability of modelling localized deformations and also leads to high computational cost with a large number of landmarks. Therefore, TPS was extended to have local support [75–77]. Rohr *et al.* [78, 79] proposed to approximate thin-plate splines to accommodate for landmark errors. Zagorchev and Goshtasby [80] conducted a comparative study of RBFs to evaluate their performances in nonrigid image registration.

Elastic Body Splines

Davis *et al.* [81] introduced Elastic Body Splines (EBS), inspired by a physical model, which describes a homogeneous and isotropic elastic body subject to a force. The basis of EBS is obtained from the analytical solutions of Navier equilibrium equation (2.3), which can be solved analytically, when the force is defined as a radial symmetric function.

The original EBS model cannot handle local deformations. To cope with this drawback, later methods employ forces that have compact support. Kohlrausch *et al.* [82] proposed Gaussian EBS employing a Gaussian function as the force. As a result, the compactness of the support of the landmarks can be controlled by the standard deviation of the Gaussian function. This method was extended by Wörz and Rohr *et al.* [83] to consider landmark errors by adjusting the Gaussian forces to allow varying weights of the landmarks with respect to the reliability of their localisation.

Free Form Deformation

The Free From Deformation (FFD) was initially proposed as a method to deform 3D objects in computer graphics [84, 85]. It was introduced in nonrigid image registration as a transformation model based on B-splines [18, 86, 87]. FFD can deform objects by manipulating the control points, producing continuous and smooth deformations (Fig. 2.6).

In general, RBF and EBS have global support. Each control point has influence in the entire transformation and, thus, cannot handle local deformations. When using a large number of control points, RBF can be computationally demanding. In contrast,

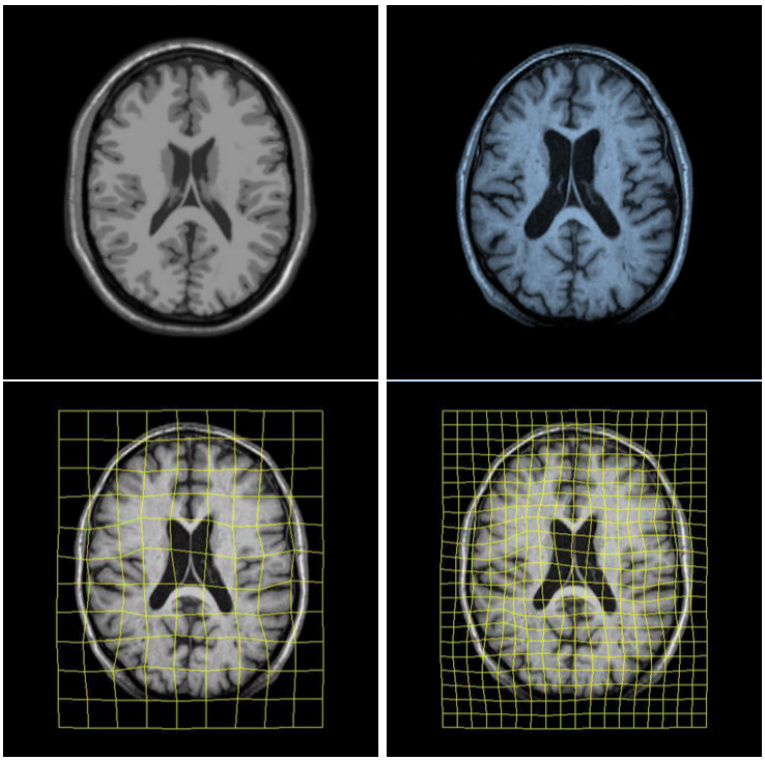

Figure 2.6: An example of the FFD registration framework. This figure depicts the concept of FFD, showing deformations of the grid points and how this is translated to the deformations of the image. First row: target and moving images; second row: transformed images after FFD registration using grid spacing of 20 mm (left) and 10 mm (right) [4].

FFD has compact local support. Changes in a control point will only influence its neighbourhood. This enables FFD to model localised deformations with fewer degrees of freedom than RBF and, thus, being more computationally efficient. RBF and EBS work with irregularly placed control points and can be employed for feature-based registrations, while the FFD requires regular grid, which is suitable for intensity-based registration.

FFD is commonly based on B-splines, in which the displacement of any point $\boldsymbol{x} = (x_1, \ldots, x_n) \in \mathbb{R}^n$ is expressed as a linear combination of the displacements of the corresponding control point $\boldsymbol{\mu}_I$:

$$\boldsymbol{D}(\boldsymbol{x}) = \sum_{\boldsymbol{I} \in \mathcal{C}} B_{\boldsymbol{I}}(\boldsymbol{x}) \boldsymbol{\mu}_{\boldsymbol{I}} \tag{2.7}$$

where the index $\boldsymbol{I} = (I_1, \ldots, I_n)$ runs along the set of supporting control points, distributed in a regular grid at positions $\boldsymbol{x_I} = (x_{I_1}, \ldots, x_{I_n})$.

The B-spline basis functions are tensor products of 1D B-spline functions centred at each control point:

$$B_I(\boldsymbol{x}) \equiv B\left(\frac{\boldsymbol{x} - \boldsymbol{x}_I}{\boldsymbol{L}}\right) \equiv \prod_{i=1}^{n} \beta\left(\frac{x_i - x_{I,i}}{L_i}\right) \tag{2.8}$$

where L_i is the spacing between control points along the i^{th} axis. The most commonly used basis is the cubic B-splines [88],

$$\beta(u) = \begin{cases} \frac{2}{3} - \frac{1}{2}|u|^2(2 - |u|) & \text{if } |u| < 1 \\ \frac{1}{6}(2 - |u|)^3 & \text{if } 1 \leq |u| < 2 \\ 0 & \text{if } |u| \geq 2 \end{cases} \tag{2.9}$$

which is a symmetric C^2-differentiable piece-wise cubic function.

Non-uniform rational basis spline (NURBS) is another type of basis that has been employed in the FFD framework. Uniform B-spline requires a regular grid, while NURBS generalises the nonrational parametric form and can be applied in a non-uniformly distributed control points. NURBS includes the weights of the control points as extra degrees of freedom

$$\boldsymbol{D}(\boldsymbol{x}) = \frac{\sum_{\boldsymbol{I} \in \mathcal{C}} B_{\boldsymbol{I}}(\boldsymbol{x})\, \boldsymbol{w_I}\, \boldsymbol{\mu_I}}{\sum_{\boldsymbol{I} \in \mathcal{C}} B_{\boldsymbol{I}}(\boldsymbol{x})\, \boldsymbol{w_I}} \tag{2.10}$$

where $\boldsymbol{w_I}$ are the weights of the control points.

Uniform B-splines can be considered as a special case of NURBS when the control points are located in a regular grid and the weights of the control points are 1. NURBS contains more degrees of freedom, and therefore, they are more flexible and can better describe local deformations. However, the user must specify the initial location of the control points and the initialisation often requires segmentation of the region of interest [89, 90]. In contrast, uniform B-spline is easy to use and it has simpler formulation allowing faster computation when the number of grid points is elevated [3, 47].

The FFD has a number of advantages over RBF. It produces smooth transformations and has compact support requiring fewer degrees of freedom than the RBF to describe local deformations. Thus, it is more efficient and more suitable for modelling local deformations than RBF [36]. The FFD have been rapidly extended for solving different problems and gained popularity in various applications. Tustison *et al.* [91] observed that conventional FFD with steepest gradient descent exhibits problematic energy topographies. This is caused by the nature of FFD formulation, which produces disproportionate weighting of the gradient at different control points. They proposed to solve this problem by normalising the gradient using B-spline weights. Schnabel *et al.* [92] proposed multi-level FFDs, in which a subset of control points across different scales are activated and optimised simultaneously. The activation of the control points is determined based on the local image entropy in the target image and the local alignment of the image pair. Recently, Shi *et al.* [47] developed multi-level FFDs with sparsity constraint, based on the principles of compressed sensing, assuming that the multi-level representation of the transformation is sparse in the parametric space. The sparse FFDs were extended to temporal registration of image sequences [93]. Other works on temporal registration based on 4D FFD were developed by Ledesma-Carbayo *et al.* [94] and Chandrashekara *et al.* [95]. Based on this idea, De Crane *et al.* [96] proposed temporal diffeormorphic FFD, which models the velocity field and integrated it over time to obtain temporal consistent displacements.

Polyaffine models

Arsigny *et al.* [97] proposed the polyaffine models to parameterise deformations with a finite number of rigid or affine transformation components. Similar to FFD, a group of control points, named anchor points, are located in the image. Each of these points influence a defined region and they do not need to be in a regular grid. In order to have a smooth transition between regions, a Gaussian function is used to represent the influence of each anchor point. The global displacements are obtained by integrating the weighted average velocities associated to each transformation component. The polyaffine models can produce invertible and smooth deformation fields. In addition,

since they are locally rigid, they are an excellent choice for registering locally rigid or affine structures, such as bones and histological slices.

The computation efficiency of the polyaffine models was improved by Arsigny *et al.* [98], who also extended them to guarantee that their inverse is also polyaffine. A recent work carried out by McLeod *et al.* [99] employed polyaffine models for the statistical analysis of the motion of the left ventricle of the heart.

2.4 Similarity measure

The similarity measure is employed to quantify the degree of likeness between the transformed image and the target image. These metrics can be categorised into feature- and intensity-based [100]. Feature-based similarity measures require a prior step to extract features, such as salient points, edges and surfaces [8]. In contrast, intensity-based metrics do not need such pre-processing and can be computed directly from the images. Feature-based similarity metrics require the images to have rich details of distinctive objects. Nevertheless, medical images often lack such details [8]. In addition, feature selection is highly application dependent, making it less general than intensity-based metrics. Thus, in this thesis, intensity-based similarity measures are adopted. The selection of such metrics highly relies on the application and the image modalities involved. Specifically, the selection should be based on the relationship expected between the corresponding intensities in the images.

The goal of optimisation is to minimise the dissimilarity between the images. To be consistent with energy minimisation of the cost function, similarity metrics that compute image difference are directly included in the cost function, while others measuring image similarity are negated.

2.4.1 Image difference measure

The simplest similarity measure is the Sum of Square Difference (SSD) of the intensities between the target and transformed moving images, defined as

$$S_{SSD}(I_t, I_m) = \frac{1}{N} \sum_{\boldsymbol{x} \in \Omega} |I_t(\boldsymbol{x}) - I_m(T(\boldsymbol{x}))|^2 \tag{2.11}$$

where $\boldsymbol{x}$ is a voxel position and $T(\boldsymbol{x})$ is the voxel location after transformation, N the number of voxels in the image domain Ω.

The SSD is sensitive to outliers of high intensity difference. A simple approach to improve the robustness to such outliers is to use Sum of Absolute Differences (SAD), defined as:

$$S_{SAD}(I_t, I_m) = \frac{1}{N} \sum_{\boldsymbol{x} \in \Omega} |I_t(\boldsymbol{x}) - I_m(T(\boldsymbol{x}))| \tag{2.12}$$

The SSD is easy to implement and efficient. Viola *et al.* [101] have shown that SSD is the optimal measure if the images have identical intensities in the corresponding structures, only differing by Gaussian noise. Thus, it has been widely employed, for instance, in intra-patient registration [102, 103]. However, it is restricted to monomodal registration, as it assumes that corresponding structures in the images have the same intensities. It also requires that the images are equally calibrated, without difference in intensity normalization or field bias.

2.4.2 Image correlation

Cross Correlation (CC) assumes linear relationship of the image intensities [53].

$$S_{CC}(I_t, I_m) = -\frac{1}{N} \sum_{\boldsymbol{x} \in \Omega} I_t(\boldsymbol{x}) \cdot I_m(T(\boldsymbol{x})) \tag{2.13}$$

The Normalized Cross Correlation (NCC), also known as correlation coefficient, has been widely used in image registration [34, 104, 105], as it is more robust to intensity and contrast changes than CC [53].

$$S_{NCC}(I_t, I_m) = -\frac{\sum_{\boldsymbol{x} \in \Omega} (I_t(\boldsymbol{x}) - \mu_t)(I_m(T(\boldsymbol{x})) - \mu_m)}{\sqrt{\sum_{\boldsymbol{x} \in \Omega} (I_t(\boldsymbol{x}) - \mu_t)^2} \sqrt{\sum_{\boldsymbol{x} \in \Omega} (I_m(T(\boldsymbol{x})) - \mu_m)^2}} \tag{2.14}$$

where $\mu_t, \mu_m, \sigma_t, \sigma_m$ are the mean and standard deviation of the intensities of the target and moving images.

2.4.3 Mutual information

In terms of the information theory, image registration can be considered as a process to maximise the amount of shared information between the target and transformed images [9]. The information of the image content can be measured by Shannon entropy [106]:

$$H = -\sum_{i} p(i) \log(p(i)) \tag{2.15}$$

where $p(i)$ is the probability of a voxel in an image having intensity i. This probability is estimated from the intensity histogram. The joint entropy can be defined as [9]:

$$H(I, J) = -\sum_{i,j} p(i, j) \log(p(i, j)) \tag{2.16}$$

where $p(i, j)$ is the joint probability distribution of intensity i, j in the moving and target image respectively. Low values of joint entropy is normally related to good alignment of the images. However, it highly depends on the overlaps of the images. For instance, when the overlap is only a region in the background, this misalignment also produces low joint entropy [42]. To mitigate this problem, mutual information includes the marginal entropies of the images, so that it is less sensitive to overlaps than joint entropy. Collignon *et al.* [107,108] and Viola and Wells *et al.* [101,109,110] independently proposed mutual information in multi-modal registration [9]

$$I(I, J) = H(I) + H(J) - H(I, J) = \sum_{i} \sum_{j} p(i, j) \log \frac{p(i, j)}{p(i) \cdot p(j)} \tag{2.17}$$

The mutual information $I(I, J)$ represents how well I explains J and vice versa. When the two images are optimally aligned, mutual information is maximised (the cost function is minimised)

$$S_{MI}(I, J) = -I(I, J) \tag{2.18}$$

However, mutual information can still increase in case of misalignment with decreasing overlap [42]. To make it more robust to changes in overlap, Studholme *et al.* [111]

introduced normalised mutual information:

$$S_{NMI}(I, J) = -\frac{H(I) + H(J)}{H(I, J)} \tag{2.19}$$

Mutual information globally measures the difference of statistical distribution of intensities in the images. This restriction has been relaxed to locally computing the similarity measure [112–117]. Alternatively, spatial information of the image can also be included by incorporating local geometric information, such as image gradient [118], higher order mutual information [119, 120] and employing prior segmentation [121–123]. Mutual information can also be computed from label representation of image patches using dictionary learning [124].

2.4.4 Other types of similarity for multi-modal registration

Mutual information can be employed for multi-modality registration, in contrast with SSD and cross-correlation, which are not suitable for multi-modality. However, the original mutual information does not provide a good local representation of image structure, since it quantifies similarity using a global statistical measure. Heinrich *et al.* [125] proposed the modality independent neighbourhood descriptor to describe local image structure by measuring the similarities of voxels in a neighbourhood of image patches. The similarity measure is the vector difference of the descriptors computed from the images. Lee *et al.* [126] and Bronstein *et al.* [127] employed machine learning techniques to measure similarity between images from different modalities.

2.5 Regularisation

Image registration is an ill-posed problem due to the existence of multiple solutions. This issue may be alleviated by including a regularisation term in the cost function. This term allows the inclusion of prior knowledge of the physical properties of the underlying deformations to restrict the outcome of the registration. There is a myriad of different regularisations in the literature, however, this thesis focuses on those used in an FFD framework.

An important characteristic of deformations involving soft tissues is smoothness. In FFD registration, the transformation is implicitly regularised to be continuous and smooth by parameterising the deformations with smooth B-spline basis. To Further improve smoothness of the deformations, Rueckert *et al.* [18] proposed the bending energy term. This regularisation term penalises high curvature of the transformation. Thus, it is zero for any linear or affine transform and only relevant for nonrigid transformations.

Topology preservation is equivalent to invertibility of the transformation. This property can be imposed to avoid singularities in the deformation field. Rueckert *et al.* [128] introduced two ways to ensure diffeomorphic transformation: (1) hard constraint on the maximum displacements of the control points, (2) a penalty term to avoid the determinant of the Jacobian falling below a pre-defined threshold.

When the images involves rigid objects, such as bones, nonrigid registration may result in undesired deformations in the rigid structures. To address this problem, Loeckx *et al.* [129] imposed orthogonality of the Jacobian matrix of the transformation to guarantee local rigidity. Staring *et al.* [130] proposed a local rigidity penalty term based on three conditions: (1) the second order derivatives of the transformation are kept close to zero; (2) the rotation matrix is controlled to be orthogonal; (3) the determinant of the Jacobian of the transformation is maintained close to one. This penalty term is computed efficiently by being expressed in terms of B-spline coefficients.

In medical images, many soft tissues are known to be nearly incompressible when undergoing small deformations in a short time period [131]. Based on this observation, Rohlfing *et al.* [132] included a local volume-preservation constraint based on the logarithm of the Jacobian determinant, which is zero when the local volume is preserved.

In addition, prior knowledge of the expected deformations can be described by statistical deformation models built from registration on training data [133]. These models were employed to guide the registration process [134–136]. Similarly, in atlas registration, expected shape information of the organ of interest can also be included. Berendsen *et al.* [137] employed statistical shape model as a penalty term for atlas segmentation.

2.6 Optimisation

The aim of image registration is to seek the optimal transformation that minimises the objective function, which is based on a similarity metric with the possible addition of one or more regularisation terms. The detailed description of optimisation methods can be found in [138–140]. Depending on the nature of the search space, optimisers can be classified into two types: continuous and discrete, in which the parameters are searched in continuous values or in a discrete set [36].

2.6.1 Continuous optimisation

In continuous optimisation methods, variables take real values and a solution is found by iterative search, until a minimum is reached. The parameters $\boldsymbol{\mu}$ are updated following the rule:

$$\boldsymbol{\mu}_{k+1} = \boldsymbol{\mu}_k + \alpha_k \boldsymbol{d}_k, \quad k = 0, 1, 2, ... \tag{2.20}$$

where α_k denotes the step size, also referred to as gain factor at the k^{th} iteration. Continuous optimisation methods differ in computing the step size α_k and search direction $\boldsymbol{d}_k$. The step size can be set to be constant, decaying with each iteration or computed by exact or inexact line search to minimise the objective function [141]. The search direction is normally computed from the first-order or second-order derivatives of the cost function. Multiple methods provide different ways of computing the search direction, as discussed in the following subsections.

Gradient descent

Gradient descent methods optimise the cost function in the direction of its negative gradient, in which the function value decreases

$$\boldsymbol{d}_{k+1} = -\boldsymbol{g}_k \tag{2.21}$$

where $\boldsymbol{g}_k$ is the gradient direction. Variants of gradient descent differs in their ways of computing step size. The step size can be simply set to be fixed, computed as a

decaying function of the number of iteration [141], using monotone line search [142], inexact line search [143], or golden section search [144]. Gradient descent methods have been applied to various registration problems, such as in the LDDMM [62] and FFD registration framework [18].

Computing the exact derivatives required for gradient descent is costly. To mitigate the computational burden, stochastic gradient descent was proposed, based on an approximation of the gradient direction. Different ways of approximating the gradient have been studied in [141]. The Kiefer-Wolfowitz (KW) method is the most basic approach employing finite difference approximation of the gradient [145]. Simultaneous Perturbation (SP) computes the approximation of the gradient at each iteration using only two measurements of the objective function, obtained by randomly varying all variables simultaneously [146]. This differs from the KW, in which the variables are varied one at a time. The Robbins and Monro (RM) is a more general method, since it does not assume the way of approximating the gradient, it only assumes the existence of an approximation of the gradient [147]. The convergence of the method is artificially forced by reducing the step size. In [141], the RM method performed the best among the three methods and was later extended to use adaptive step size [148].

Conjugate gradient descent has a better convergence rate than other gradient descent methods [36]. It employs a search direction that is conjugate to the search direction in the previous step. It is a linear combination of the current gradient direction and the previous search direction [138].

$$\boldsymbol{d}_k = -\boldsymbol{g}_k + \beta_k \boldsymbol{d}_{k-1} \tag{2.22}$$

The weights of the directions can be defined in various ways, such as formulas proposed in [149–152]. Mored detailed reviews on the conjugate gradient methods can be found in the survey by Hager and Zhang [153].

Quasi-Newton methods

The Newton method, also known as the Newton-Raphson method, employs first and second order derivatives. In each iteration, it constructs a quadratic local approxima-

tion of the cost function and moves to the minimiser of this quadratic function until convergence [138]. Thus, each step is given by

$$\boldsymbol{\mu}_{k+1} = \boldsymbol{\mu}_k - |H(\boldsymbol{\mu}_k)|^{-1}\boldsymbol{g}_k(\boldsymbol{\mu}_k) \tag{2.23}$$

where $H(\boldsymbol{\mu}_k)$ is the Hessian matrix of the objective function. The Newton method converges faster than gradient descent. However, computing the Hessian matrix and its inverse is computationally expensive. To alleviate the computational burden, quasi-Newton method approximates the inverse of the Hessian matrix using first order derivatives

$$\boldsymbol{\mu}_{k+1} = \boldsymbol{\mu}_k - \alpha_k L_k \boldsymbol{g}(\boldsymbol{\mu}_k) \tag{2.24}$$

where $L_k \approx |H(\boldsymbol{\mu}_k)|^{-1}$. The approximation L_k can be computed in different ways, among which the most important ones are the Davidon-Fletcher-Powell (DFP) and the Broyden-Fletcher-Goldfarb-Shanno (BFGS) [154]. BFGS formula is more efficient than DFP [154, 155]. A variant of BFGS, limited memory BFGS (LBFGS), is widely employed, because it requires less memory for storing L_k and, thus, it is suitable for high dimensional problems [156, 157]. Quasi-Newton methods have been applied in various image registration problems [49, 116, 158]. Stochastic quasi-Newton was also developed to improve the computational efficiency [159].

2.6.2 Discrete optimisation

In discrete optimisation, variables have discrete values and the optimal solution is searched in a discrete set. This optimisation approach usually employs Probabilistic Graphical Models (PGM), and most of the time Markov Random Fields (MRF) [160]. A PGM consists of nodes representing random variables taking values in a discrete set of labels and edges representing the relationship between the variables. In this setting, the set of labels is related to a set of possible deformations. Thus, the optimisation searches for the best label for each grid point in order to minimise the cost function. Methods for solving a PGM problem can be classified into: min-cut, belief propagation and dual decomposition.

Min-cut

Min-cut problems are usually solved using max-flow. In a binary label problem, a directed graph has two special nodes, called the source s and the sink t. The cost of a cut is the total flow passing through the edges of the graph. This value is control by the weights of the edges and the capacity of the nodes. Finding the minimum cut is performed by searching the path that maximizes the flow from s to t [161]. Tang and Chuang [162] employed a dense displacement field representing each pixel as a node and the cost function is optimised using graph-cut [163]. So *et al.* extended this work to multi-level [164], replacing SSD to mutual information [165] and applied it to brain images [166]. Graph-cut can find the global minimum or close to the global minimum. But due to the computational complexity, the number of nodes and search space are limited.

Belief propagation

Belief propagation is also known as message passing. The idea is that each node sends a message with their belief about the optimal label to their neighbours. These neighbouring nodes update their beliefs and send messages to the next neighbours. This process is repeated until all the belief of the nodes does not change [167]. Yang *et al.* [168] improved the efficiency of the belief propagation method by hierarchically reducing the search space. Heinrich *et al.* [169] adapted this algorithm in a FFD registration framework.

Dual decomposition

Dual decomposition is based on decomposing a complex problem into a set of sub-problems, called slaves, together with linear constraints to enforce an agreement in the solution of each sub-problem. The set of linear constraints is controlled and modified by a master to ensure that the global solution is close to that of the original complex problem. The fast Primal-Dual (fast-PD) [170] is an efficient algorithm of this type. Glocker *et al.* [171, 172] reformulated the cost function of FFD registration using an

MRF definition and optimised it using fast-PD method [170, 173]. This work was applied to atlas-based segmentation [174] and extended to include prior knowledge of the deformation using pairwise potentials estimated from statistical correlation of the deformations in the training data [175]. Sotiras *et al.* employed fast-PD for diffusion tensor registration [176], symmetric iconic registration [177] and group-wise registration [178]. Fast-PD is computationally efficient and obtained comparable accuracy to continuous optimisation methods. However, due to the large memory requirement, it only takes sparse sampling of the displacements, leading to reduced accuracy [172]. Heinrich *et al.* [179] employed dynamic programming on minimum spanning tree to reduce the demand for large memory and, thus, was able to employ denser displacement sampling to achieve more accurate results. This method was later extended to replace FFD by supervoxel graphs [180].

The discrete optimisation methods can find the global minimum or a solution close to the minimum. They do not require the derivatives of the cost function and, thus, allows a larger range of similarity measures and regularisers. A common drawback of this type of methods is that the discretization of the search space limits the registration accuracy. Furthermore, it is not straightforward to introduce them to the existing registration frameworks, as they are not directly compatible with other existing components of registration and often require reformulation of the cost function.

2.7 Conclusions

Registration is an important tool for acquiring deformations of anatomical structures in medical images. The three main components of registration are: objective function (similarity metric and regularisation), optimisation and transformation model.

In the literature, the most widely used similarity metrics in mono-modality registration are SSD and cross correlation, whereas in the case of multi-modality registration, mutual information, metrics based on image gradient, or features-based similarity are commonly required.

In optimisation, gradient-based methods, such as LBFGS, are widely used, because

of their accuracy and compatibility with most of the previously proposed similarity metrics and transformation models. However, they are sensitive to the initial conditions. This can be alleviated by first rigidly aligning the images and employing a multiresolution scheme, which reduces the likelihood of the optimiser to stop in a local minima. Another limitation of the gradient-based optimisers is their long computational time. These two problems do not exist with discrete optimisers, which are fast and robust to local minima. However, in general, discrete optimisers cannot be directly included in an existing registration framework and often require reformulating the objective function or developing problem specific metrics. Moreover, the accuracy of discrete registration is limited by the discretisation of the search space. On the other hand, continuous optimisation does not have the limitation of accuracy and their speed can be largely improved by employing stochastic techniques, such as stochastic gradient descent [148] or stochastic LBFGS [159], or by optimising the implementation based on multi-threading [181] or GPU computing [182]. In general, the simplicity of gradient-based approaches and their compatibility with existing registration frameworks make them more popular than discrete optimisers.

The most widely-used transformation models are Demons and FFD. The main advantage of Demon over FFD is its computational efficiency [183]. However, Demons is more sensitive to noise than FFD [184] and provides lower accuracy [100]. Nevertheless, FFD is versatile with multiple extensions, such as, multiresolution [18], multiview [185], spatio-temporal [3], and diffeomorphic registration [128]. The main advantage of FFD is its modularity. Most previously-proposed similarity measures and continuous optimisers can generally be employed straight-forwardly. In contrast, the formulation of demons is equivalent to optimising the similarity measure of SSD with gradient descent [68]. SSD assumes constant intensities, hindering its usability for multi-modality registration. Employing other similarity metrics in the Demons framework requires to modify the formulation of the metrics [183, 186]. Moreover, FFD has a sound mathematical formulation, which allows direct manipulation of the transformation model, such as multilevel FFD [92] and 4D FFD [96]. These properties make FFD a good candidate for incorporating discontinuities in the transformation model.

Thus, in this thesis, FFD was selected as the base for developing a registration framework to handle general discontinues.

Chapter 3

eXtended Free-Form Deformation (XFFD): tissue transitions with strong discontinuities

This chapter describes the XFFD registration framework. The formulation of XFFD was inspired by the interpolation method from eXtended Finite Element Method (XFEM). XFFD incorporates discontinuities by enriching the B-spline basis functions coupled with extra degrees of freedom. XFFD is integrated into a rigorously formulated multiresolution scheme that employs an exact parameter upsampling method. As explained in Chapter 1, the aim of this thesis is to develop a general registration methods that can handle all types of tissue transitions. In this chapter, only the most generic model is developed with the XFFD framework. The general classification of tissue transitions and the mathematical formulation for the corresponding models integrated in XFFD will be presented in the following chapter.

3.1 Motivation

As explained in the literature review (Chapter 2), the classical FFD commonly relies on B-spline basis, resulting in a smooth and continuous deformation field, which reflects the similarly smooth deformations hypothesised to be exhibited by compliant tissues.

This constraint, however, is not desirable when the tissue transitions are discontinuous. For instance, discontinuities are present at the interface of structures that undergo different motion patterns during the respiratory cycle, such as, the lungs and the thoracic cage. For images acquired in different poses, the relative position between different organs can also change, as observed in the abdominal organs. In longitudinal studies, discontinuities may also result from morphological changes associated with growth process or treatments, such as at the boundaries between tumours and surrounding parenchyma. Artificially imposing continuity in registration of tissues that exhibit discontinuities can introduce artefacts, resulting in non-physically plausible deformation and strain fields (Fig. 3.4). The strain is related to the physical properties of tissues, which are key to many diagnostic questions [19]. Therefore, artefacts leading to incorrect strain field have a direct negative impact on the assessment of kinetics and functionality of the corresponding organs.

3.2 Previous works

Proper management of physical discontinuities in medical image registration is an active area of research. According to the transformation model employed, the existing approaches can be classified into two categories; diffusion- or spline-based registration methods. In most diffusion-based methods, discontinuities were explicitly incorporated in the regularisation schemes. Direction-dependent regularisers were employed by decomposing the deformation field into normal and tangential directions at the discontinuity interface and smoothing was only applied in the tangential components but not across the boundary [187, 188]. Locally adaptive regularisers were adopted with discontinuity preserving properties [189, 190].

FFDs are parametric transformation models with fewer degrees of freedom; thus, they are potentially more efficient. They naturally produce smooth deformation fields without explicit regularisers. The basis functions are piece-wise polynomial and have local support, so that they are computationally efficient and compatible with gradient-based optimisers. The most straightforward FFD-based method for handling disconti-

nuities is based on independently registering regions on either side of the discontinuity interface using masks, covering the object of interest. However, this simple approach does not prevent the misalignment of the object boundaries. In the transformed image, the organ can shrink or expand beyond the actual boundary position, since it is not penalised by the cost function, unless specific constraints are imposed.

In [5], this problem is addressed by using masks to modify the image intensities outside the region to a homogenous extreme value. Thus, any misalignment is penalised since it increases the dissimilarity metric. This method requires provision of masks for both moving and target images. This requirement is reduced to one discontinuity interface for the target image in [6]. They introduced another strategy based on the decomposition of the displacement field into the normal and tangential directions of the interface in a multiple B-spline transformation framework. The main issue of this method is that the decomposition into the tangential and normal directions was performed at the control points. Thus, the interpolation of these directions only approximates the orientation of the actual discontinuity interface, producing inaccuracies in the registration results. This problem is more evident when there are structures of smaller scale, like sharp edges present in the interface delimiting the lungs. In their experiments, they used a motion mask covering also the abdomen, based on the assumption that the lungs and the abdomen move continuously together, although this assumption is not accurate, as the lungs and the abdominal organs slide relative to each other [191]. This restriction in the shape of the discontinuity interface was alleviated by using multiple B-spline transformations covering the regions separated by the discontinuity interface, and a penalty term to reduce gaps and overlaps at the region boundaries [192].

Most of the existing registration methods handling discontinuities are tailored solely to sliding motion. This type of discontinuity exists between structures which are adjoint and unable to get detached, but which are able to slide over each other. This assumption concerning the allowed motion is not suitable for some organs undergoing more complex motion. For instance, the liver slides over the diaphragm and some other abdominal organs, but it also touches and separates from some organs, such as

the kidney. We refer to this type of motion as free discontinuous motion, existing between objects that are not attached and can move freely from each other. Imposing a sliding constraint at the interface of organs detaching from each other can introduce detrimental artefacts in the deformation field.

In this chapter, a novel registration method is developed for treating discontinuities in general, coined eXtended Free Form Deformation (XFFD). The XFFD method was inspired by the interpolation function enrichment concepts that underpin eXtended Finite Element Methods (XFEMs) and Partition of Unity Methods more generally. The XFEM is an extension of Finite Element Methods (FEM) aiming at handling discontinuities without the need of remeshing, which is employed to adapt the finite element mesh by tracking the discontinuities at each time point. We have borrowed the enrichment concept from XFEM, extended it from the linear interpolation case to that of cubic B-splines, and incorporated it into the FFD formalism. In XFFD, discontinuities are incorporated in the enrichment term with extra degrees of freedom within a single B-spline transformation.

FFD registration algorithms often employ a multiresolution strategy, in which multiple scales of both image resolution and control point grid spacing are considered [18]. In general, this strategy improves the result, allowing for larger deformations without being trapped in a local minimum.

A multiresolution framework is developed for XFFD, initializing the transformation with the output transformation from the previous scale. Since the transformations in two consecutive scales are represented by different sets of parameters, we need to obtain the mapping between the parameter sets that renders the transformations themselves equivalent. We name this operation *parameter upsampling*.

Despite its importance, parameter upsampling has not received sufficient attention in the literature. To the best knowledge of the authors, this process has not been explicitly described in details and and only sometimes the reader is referred to one of the following articles [193–195]. Nevertheless, its application in the case of methods in which discontinuous motion is represented is not straightforward.

In the literature, there are two existing strategies for parameter upsampling: least

square approximation [193, 194], and B-spline refinement [195]. The first method was initially designed for image resampling. But it is widely used for B-spline parameter upsampling, as it has been implemented in ITK [196] and employed in Elastix [181]. However, it is not straightforward to extend it for XFFD. The second method was derived in [195] only for 2D, and with a notation not easily generalizable for other dimensions. In this chapter, the second strategy is employed but it is reformulated with more intuitive expressions, in order to develop its extension for XFFD in any dimension. This procedure has a unique and exact solution, as demonstrated in Section 3.3.4, and has been integrated in the multiresolution XFFD.

3.3 Methods

3.3.1 Free form deformation

FFD was developed as a method to deform objects in computer graphics [84] and was later introduced to transform a moving image of any dimension n to a target one in nonrigid image registration [18]. In order to obtain smooth and continuous deformations, B-splines are commonly used as basis functions. The displacement of any point $\boldsymbol{x} = (x_1, \ldots, x_n) \in \mathbb{R}^n$ is thus expressed as the linear combination

$$\boldsymbol{D}(\boldsymbol{x}) = \sum_{\boldsymbol{I} \in \mathcal{C}} B_{\boldsymbol{I}}(\boldsymbol{x}) \boldsymbol{\mu}_{\boldsymbol{I}} \tag{3.1}$$

where the index $\boldsymbol{I} = (I_1, \ldots, I_n)$ runs along the set of control points, $\mathcal{C}$, distributed in a regular grid at positions $\boldsymbol{x}_I$, and $\boldsymbol{\mu}_I$ is the displacement of the corresponding control point. The basis functions are tensor products of 1D B-spline functions centered at each control point:

$$B_I(\boldsymbol{x}) \equiv B\left(\frac{\boldsymbol{x} - \boldsymbol{x}_I}{\boldsymbol{L}}\right) \equiv \prod_{i=1}^{n} \beta\left(\frac{x_i - x_{I,i}}{L_i}\right) \tag{3.2}$$

where L_i is the spacing between control points along the i^{th} axis. The most used basis function is the cubic B-spline [88],

$$\beta(u) = \begin{cases} \frac{2}{3} - \frac{1}{2}|u|^2(2-|u|) & \text{if } |u| < 1 \\ \frac{1}{6}(2-|u|)^3 & \text{if } 1 \leq |u| < 2 \\ 0 & \text{if } |u| \geq 2 \end{cases} \tag{3.3}$$

which is a symmetric C^2-differentiable piece-wise cubic function.

3.3.2 Extended free form deformation

The eXtended Free Form Deformation (XFFD) method has been inspired by the eXtended Finite Element methods (XFEM) [197]. Because of the continuity of the standard FEM interpolation functions, discontinuities like fractures and material interfaces can only be incorporated by using a mesh that conforms to the interface geometry. Modelling evolving discontinuities therefore entails continuous remeshing, to maintain conformation with the changing interface geometry, incurring high computational cost. The XFEM avoids remeshing by adding an additional structure describing the location of the discontinuity surface, such as a surface mesh or level sets, and enriched basis functions encoding the desired discontinuities. In this chapter, a surface mesh is adopted to represent the discontinuity location.

In a registration framework, discontinuities can be accommodated in a similar way to XFEM by introducing an enrichment term in the conventional FFD formalism [198]:

$$\boldsymbol{D}(\boldsymbol{x}) = \sum_{\boldsymbol{I} \in \mathcal{C}} B_{\boldsymbol{I}}(\boldsymbol{x}) \boldsymbol{\mu}_{\boldsymbol{I}} + \sum_{\boldsymbol{J} \in \widetilde{\mathcal{C}}} M_{\boldsymbol{J}}(\boldsymbol{x}) \boldsymbol{\lambda}_{\boldsymbol{J}} \tag{3.4}$$

where $\boldsymbol{\lambda}_{\boldsymbol{J}}$ denotes the parameters for the extra degrees of freedom, added for the subset of control points $\boldsymbol{J} \in \widetilde{\mathcal{C}}$, for which the discontinuity intersects the support of their corresponding basis function, $B_{\boldsymbol{J}}(\boldsymbol{x})$. Since the extra degrees of freedom are added only near the discontinuities, the increase in computation with respect to standard FFD

is not substantial. The enriched basis function is defined by the product

$$M_{\boldsymbol{J}}(\boldsymbol{x}) = B_{\boldsymbol{J}}(\boldsymbol{x})\,\psi(\boldsymbol{x}) \tag{3.5}$$

where $\psi(\boldsymbol{x})$ is the enrichment function incorporating the discontinuity.

3.3.3 Enrichment function

The enrichment function must incorporate a gap across the discontinuity surface, but be continuous elsewhere. This can be implemented in many different ways. In general, an n-dimensional closed hyper-surface will be considered for representing the boundary of an object. Then, the most simple option is the sign function

$$\psi(\boldsymbol{x}) = \begin{cases} -1 & \text{if } \boldsymbol{x} \text{ is inside} \\ \\ 1 & \text{if } \boldsymbol{x} \text{ is outside} \end{cases} \tag{3.6}$$

An illustration of the resulting enriched basis functions, $M_{\boldsymbol{J}}(x)$, is presented in Fig. 3.1. Thus, the enriched basis functions decay to zero smoothly at the function support limits. This similarly guarantees a smooth transition between enriched and conventional control points, without introducing extra discontinuities. In addition, the L^p-norm (for any p) of these enriched functions coincides with that of the normal B-splines, and is independent of the control points. Observe that the enriched subset, $\widetilde{\mathcal{C}}$, only includes control points whose support region intersects with the discontinuity. The enriched function for control points outside this subset would be unavailing.

3.3.4 Control points upsampling

The most common strategy for the upsampling of the control poins is to halve the grid spacing at each scale refinement, keeping all the control points in the same position and inserting extra control points between them. For this upsampling protocol, it will be proven below that a unique exact solution exists for the upsampling of the XFFD parameters, and the corresponding mapping will be deduced. An analogous proof could be provided for the corresponding protocol of dividing the control points spacing

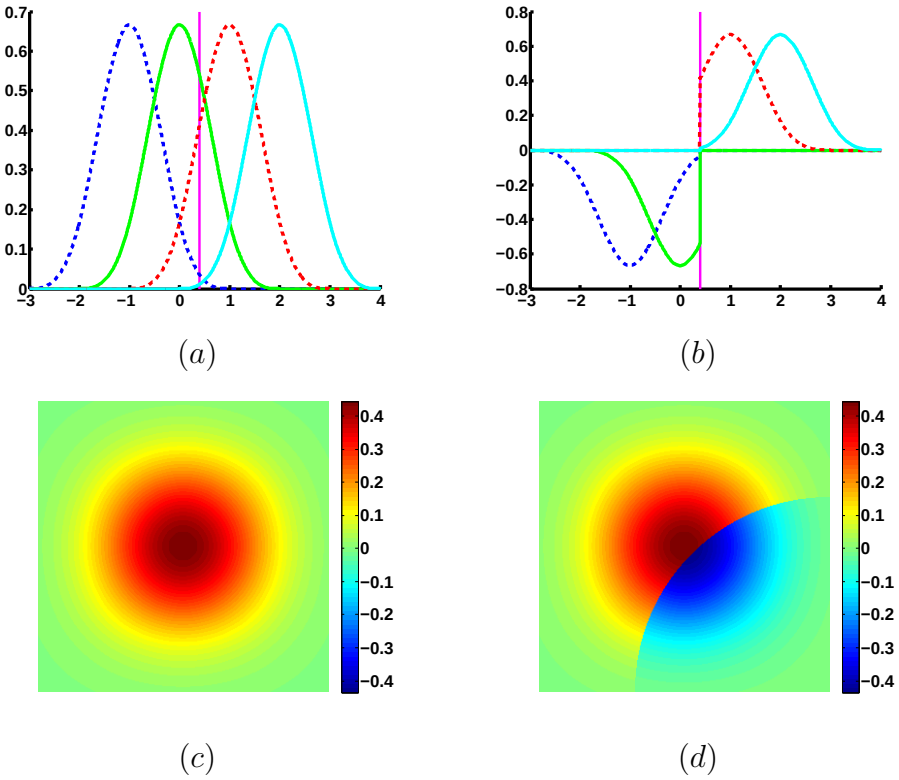

Figure 3.1: Enriched B-spline basis functions in the vicinity of a discontinuity, indicated by a pink dashed line: (a) conventional basis functions; (b) enriched basis functions. (c) a 2D conventional B-spline basis function; (d) a 2D enriched B-spline basis function with curved discontinuity boundary.

by any integer m. However, for simplicity, the proof is restricted to $m = 2$.

Cubic B-splines are piecewise cubic polynomials. As stated in formula (3.3), the support of $\beta(u)$ is split into four components, corresponding to the intervals between consecutive control points: [-2,-1], [-1,0], [0,1], and [1,2]. The upsampled basis functions are also piecewise cubic polynomials for intervals resulting from halving the previous ones. It is evident that if a function is a cubic polynomial in an interval, it is also a cubic polynomial in any subinterval, with smooth matching between subintervals. This fact provides the intuition behind the result that the function $\beta(u)$ can be exactly represented as a linear combination of the upsampled basis:

$$\beta(u) = \sum_{k=-2}^{2} A_k \, \beta(2u - k) \tag{3.7}$$

Separating the equation into different intervals and expanding the expressions according to (3.3) results in a system of linear equations for the constants A_k, with polynomial coefficients in u. Although this system is overdetermined, it is consistent and has the unique solution

$$A_{-2} = A_2 = \frac{1}{8}, \quad A_{-1} = A_1 = \frac{1}{2}, \quad A_0 = \frac{3}{4}. \tag{3.8}$$

The resulting linear combination is illustrated in Fig. 3.2 (a). The symmetry of the coefficients is a consequence of the symmetry of the B-spline basis functions.

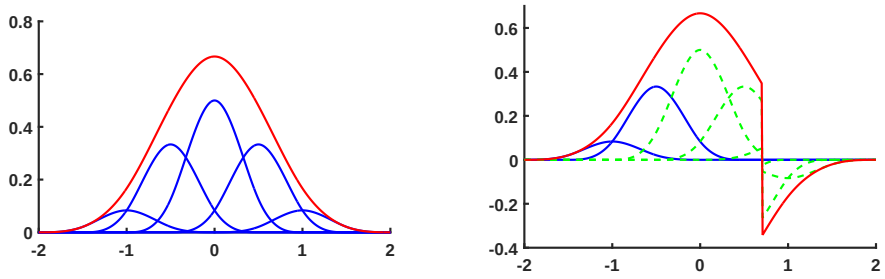

(a) (b)

Figure 3.2: 1D B-spline basis functions, represented by the ones in the upsampled grid with half grid spacing: (a) a non-enriched B-spline basis function in the original grid (red) can be represented by non-enriched basis functions in the upsampled grid (blue); (b) an enriched B-spline basis function in the original grid (red) can be represented by non-enriched basis functions (blue) and enriched ones (green dashed line) in the upsampled grid.

Considering the definition of n-dimensional B-spline basis functions in (3.2), it is straightforward to derive the analogous expression for the upsampled basis functions:

$$\begin{aligned} B_{\boldsymbol{I}}(\boldsymbol{x}) &= \prod_{i=1}^{n} \beta\left(\frac{x_i - x_{I,i}}{L_i}\right) \\ &= \sum_{k_1=-2}^{2} \cdots \sum_{k_n=-2}^{2} \prod_{i=1}^{n} A_{k_i}\, \beta\left(2\frac{x_i - x_{\boldsymbol{I},i}}{L_i} - k_i\right) \end{aligned} \tag{3.9}$$

Since the control points are located in a regular grid with spacings $\boldsymbol{L} = (L_1, \ldots, L_n)$, their position can be expressed relative to the origin of the control point grid: $\boldsymbol{x_I} = \boldsymbol{x_0} + \boldsymbol{IL}$. To simplify expressions, the following assumption can be made: $A_k = 0$ for

$|k| > 2$, denoting $A_{\boldsymbol{k}} = A_{k_1} \times \cdots \times A_{k_n}$. Thus,

$$\begin{aligned} B_{\boldsymbol{I}}(\boldsymbol{x}) &= \sum_{\boldsymbol{k}} A_{\boldsymbol{k}} \prod_{i=1}^{n} \beta\left(\frac{x_i - x_{\mathbf{0},i}}{L_i/2} - 2I_i - k_i\right) \\ &= \sum_{\boldsymbol{k}} A_{\boldsymbol{k}} B^{\uparrow}_{2\boldsymbol{I}+\boldsymbol{k}}(\boldsymbol{x}) \\ &= \sum_{\boldsymbol{I}^{\uparrow} \in \mathcal{C}^{\uparrow}} A_{\boldsymbol{I}^{\uparrow}-2\boldsymbol{I}} B^{\uparrow}_{\boldsymbol{I}^{\uparrow}}(\boldsymbol{x}), \end{aligned} \tag{3.10}$$

where the upsampled functions, coefficients and sets are denoted by the superscript $\uparrow$.

The expression of the enriched basis functions (3.5) can be obtained from the previous one:

$$M_{\boldsymbol{J}}(\boldsymbol{x}) = B_{\boldsymbol{J}}(\boldsymbol{x})\, \psi(\boldsymbol{x}) = \sum_{\boldsymbol{I}^{\uparrow} \in \mathcal{C}^{\uparrow}} A_{\boldsymbol{I}^{\uparrow}-2\boldsymbol{J}} B^{\uparrow}_{\boldsymbol{I}^{\uparrow}}(\boldsymbol{x})\, \psi(\boldsymbol{x}) \tag{3.11}$$

In this summation, enriched and non-enriched control points need to be discriminated. For the enriched ones, $\boldsymbol{J}^{\uparrow} \in \widetilde{\mathcal{C}}^{\uparrow}$, the product of the upsampled basis functions with $\psi(\boldsymbol{x})$ results in the upsampled enriched basis functions, $M^{\uparrow}_{\boldsymbol{J}^{\uparrow}}(\boldsymbol{x})$. For the non-enriched ones, $\boldsymbol{I}^{\uparrow} \in \mathcal{C}^{\uparrow} \setminus \widetilde{\mathcal{C}}^{\uparrow}$, the factor $\psi(\boldsymbol{x})$ is constant in the whole support of the function $B^{\uparrow}_{\boldsymbol{I}^{\uparrow}}(\boldsymbol{x})$, being positive or negative depending on the region where the control point, $\boldsymbol{x}_{\boldsymbol{I}^{\uparrow}}$, is located. Thus,

$$M_{\boldsymbol{J}}(\boldsymbol{x}) = \sum_{\boldsymbol{I}^{\uparrow} \in \mathcal{C}^{\uparrow}} S_{\boldsymbol{I}^{\uparrow}} A_{\boldsymbol{I}^{\uparrow}-2\boldsymbol{J}} B^{\uparrow}_{\boldsymbol{I}^{\uparrow}}(\boldsymbol{x}) + \sum_{\boldsymbol{J}^{\uparrow} \in \widetilde{\mathcal{C}}^{\uparrow}} A_{\boldsymbol{J}^{\uparrow}-2\boldsymbol{J}} M^{\uparrow}_{\boldsymbol{J}^{\uparrow}}(\boldsymbol{x}), \tag{3.12}$$

where

$$S_{\boldsymbol{I}^{\uparrow}} = \begin{cases} -1 & \text{if } \boldsymbol{x}_{\boldsymbol{I}^{\uparrow}} \text{ is inside and } \boldsymbol{I}^{\uparrow} \notin \widetilde{\mathcal{C}}^{\uparrow} \\ 1 & \text{if } \boldsymbol{x}_{\boldsymbol{I}^{\uparrow}} \text{ is outside and } \boldsymbol{I}^{\uparrow} \notin \widetilde{\mathcal{C}}^{\uparrow} \\ 0 & \text{if } \boldsymbol{I}^{\uparrow} \in \widetilde{\mathcal{C}}^{\uparrow}. \end{cases} \tag{3.13}$$

Fig. 3.2 (b) illustrates this linear combination for the enriched functions.

Equation (3.10) and (3.13) can be substituted into (3.4) to reexpress the displacements in the upsampled basis functions:

$$\boldsymbol{D}(\boldsymbol{x}) = \sum_{\boldsymbol{I}^{\uparrow} \in \mathcal{C}^{\uparrow}} B^{\uparrow}_{\boldsymbol{I}^{\uparrow}}(\boldsymbol{x}) \boldsymbol{\mu}_{\boldsymbol{I}^{\uparrow}} + \sum_{\boldsymbol{J}^{\uparrow} \in \widetilde{\mathcal{C}}^{\uparrow}} M^{\uparrow}_{\boldsymbol{J}^{\uparrow}}(\boldsymbol{x}) \boldsymbol{\lambda}_{\boldsymbol{J}^{\uparrow}} \tag{3.14}$$

where the upsampled parameters are

$$\begin{aligned} \boldsymbol{\mu}_{\boldsymbol{I}^{\uparrow}} &= \sum_{\boldsymbol{I}\in\mathcal{C}} A_{\boldsymbol{I}^{\uparrow}-2\boldsymbol{I}}\,\boldsymbol{\mu}_{\boldsymbol{I}} + \sum_{\boldsymbol{J}\in\widetilde{\mathcal{C}}} S_{\boldsymbol{I}^{\uparrow}} A_{\boldsymbol{I}^{\uparrow}-2\boldsymbol{J}}\,\boldsymbol{\lambda}_{\boldsymbol{J}} \\ \boldsymbol{\lambda}_{\boldsymbol{J}^{\uparrow}} &= \sum_{\boldsymbol{J}\in\widetilde{\mathcal{C}}} A_{\boldsymbol{J}^{\uparrow}-2\boldsymbol{J}}\,\boldsymbol{\lambda}_{\boldsymbol{J}} \end{aligned} \tag{3.15}$$

Observe that enriched and non-enriched parameters are coupled in the upsampling.

3.4 Materials

To evaluate the proposed method, two synthetic datasets and two publicly available clinical datasets were employed for validation.

3.4.1 Synthetic dataset

The first dataset includes 2D images with checkerboard texture and a deformation pattern that emulates sliding motion. The image size is 256×256 pixels. In the target image, the right-side region was vertically displaced by 15 pixels (Fig. 3.4).

The second synthetic dataset presents free discontinuous motion. The images show two objects that touch and separate, with resolution of 512×512 pixels (Fig. 3.7). The target image is composed of four elements, two circles touching each other and two small ellipses near the right circle. The moving image differs from the target in that the right circle moves towards the right side and the two ellipses towards each other. The right circle can move independently of the other structures and the surrounding materials. Thus, the discontinuity interface was set at its boundary.

3.4.2 DIR-lab dataset

The dataset contains 10 4D CT images acquired from patients treated for esophageal and lung cancer with a spatial resolution varying between $0.97\times0.97\times2.5\,\text{mm}^3$ and $1.16\times1.16\times2.5\,\text{mm}^3$ [23]. This dataset includes 300 landmarks for each image volume, annotated by experts with inter-observer variability around 1 mm [23]. Lung

masks were semi-automatically created using thresholding and morphological operations followed by manual corrections.

3.4.3 4D CT liver dataset

This dataset consists of 4 cases acquired in the Children's National Medical Center at Stanford [188]. The images cover the lower part of the lungs and abdominal organs, including the liver. For each volume, 20 landmarks were provided for the abdominal organs. A rough segmentation of the liver was also provided for each volume. The mask for the target image was manually corrected and used as input of XFFD.

For both medical image datasets, the volume at the end of inhale was selected as the target image and the one at the end of exhale as the moving image.

In the respiratory cycle, the lungs exhibit sliding motion at the lung boundary against the rib cage and diaphragm, as the lungs expand and contract, while the ribs and spine remain relatively static (Fig. 3.3 (a-b)). The liver motion is more complicated, as it is the most movable abdominal organ [199], and does not have a fixed relationship to the skin surface or the surrounding organs [200, 201], although they are related by ligaments or membranes [202]. Thus, the liver can be subject to both sliding and free discontinuous motion (Fig. 3.3 (c-d)).

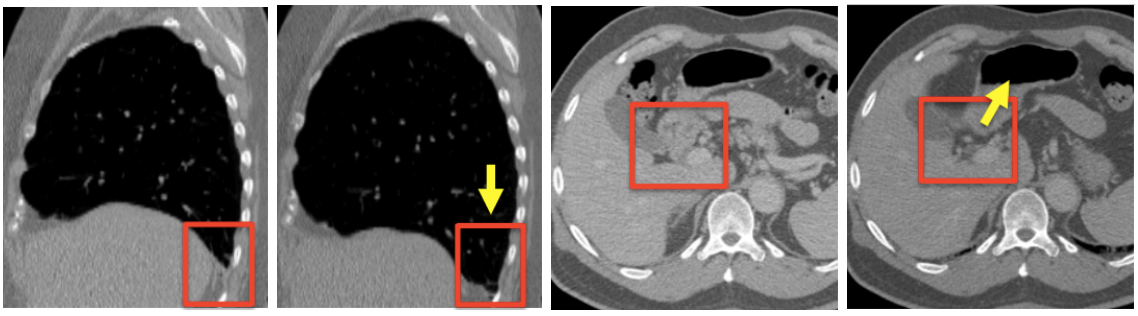

(a) (b) (c) (d)

Figure 3.3: Motion in the clinical datasets: (a-b) lung motion; (c-d) liver motion.

3.5 Experiments

The proposed method has been implemented as a module in the image registration toolbox Elastix [181]. In the experiments, XFFD was employed as the transformation model, normalized cross-correlation as similarity metric, and Limited memory Broyden-Fletcher-Goldfarb-Shanno (LBFGS) as the optimiser, because cross-correlation is robust to linear variations in image intensities [203] and LBFGS is known for its high performance in dealing with high-dimensional problems [204]. For the sake of fair comparison, parameters were selected similar to those from [192]. For the lung and liver datasets, five scales were employed in the multiresolution scheme (Table 3.1, 3.2). In the DIR-lab dataset, at each resolution, the images were smoothed and down-sampled by a Gaussian smoothing pyramid with standard deviation (σ) corresponding to half of the one at the previous scale. For the five scales, the smoothing is set by $\sigma = (16, 8, 4, 2, 1)$ voxels in the transversal plane and $\sigma = (8, 4, 2, 1, 0)$ voxels in the perpendicular direction, since the transversal image spacing is approximately half of that of the vertical. The grid spacing was set to be (80, 80, 40, 20, 10) mm for each scale. For the first synthetic dataset, a single resolution was employed with grid spacing of 64×64 pixels (Table 3.3). For the second synthetic dataset, three resolutions were used with grid spacings 256, 128, and 64 pixels (Table 3.4).

Table 3.1: Parameters for experiments on DIR-lab dataset

Parameters	Values	Function
Number of scales	5	number of scales of image pyramids
standard deviation (σ)	(16, 8, 4, 2, 1) voxels (transversal plane) (8, 4, 2, 1, 0) voxels (axial direction)	standard deviation of Gaussian smoothing
grid spacing	(80, 80, 40, 20, 10) mm	grid spacing of grid pyramids

Table 3.2: Parameters for experiments on 4D CT liver dataset

Parameters	Values	Function
Number of scales	5	number of scales of image pyramids
standard deviation (σ)	(4,4,4,2,1) voxels (transversal plane) (2,2,2,1,0) voxels (axial direction)	standard deviation of Gaussian smoothing
grid spacing	(80, 80, 40, 20, 10) mm	grid spacing of grid pyramids

Table 3.3: Parameters for experiments on synthetic dataset with sliding motion

Parameters	Values	Function
Number of scales	1	number of scales of image pyramids
standard deviation (σ)	(0, 0) pixels	standard deviation of Gaussian smoothing
grid spacing	(64, 64) pixels	grid spacing of grid pyramids

Table 3.4: Parameters for experiments on synthetic dataset with free discontinuous motion

Parameters	Values	Function
Number of scales	3	number of scales of image pyramids
standard deviation (σ)	(4, 2, 0) pixels	standard deviation of Gaussian smoothing
grid spacing	(256, 128, 64) pixels	grid spacing of grid pyramids

3.5.1 Metrics for evaluation

Target Registration Error (TRE) was employed to quantitatively evaluate the accuracy of the registration. The landmark error is computed as the Euclidean distance between the landmarks in the moving image and those in the target image, displaced by the deformation field. The mean and standard deviation of the distance of all the landmarks in each case was reported as the TRE [5, 6, 187, 188, 190, 192].

Gap and Overlap volumes may appear between the regions in both sides of the discontinuity as an undesired effect, when dealing with discontinuities in the transformation. To evaluate this effect, the surface mesh describing the discontinuity interface was transformed by considering it to belong to either the inside or the outside, producing two transformed meshes, denoted as S^- and S^+, respectively. The volume enclosed by each transformed mesh was extracted and represented as a binary mask in the same resolution as registered images. This results in interior, $V_{\text{In}}^{\pm}$, and exterior, $V_{\text{Out}}^{\pm}$, regions for each surface, $S^{\pm}$. Then, the gap volume were measured as $V_{\text{Out}}^{-} \cap V_{\text{In}}^{+}$ and the overlap volume as $V_{\text{In}}^{-} \cap V_{\text{Out}}^{+}$ [5, 6, 192].

Qualitative evaluation of the resulting deformation field was performed by visual inspection of the transformed grid and the displacement vector field. Plausibility of the tissue expansion and compression was assessed by the volumetric strain, which is computed from the determinant of the Jacobian of the transformation [205].

3.5.2 Comparison between FFD and XFFD: influence of incorporating discontinuous transformations

To evaluate the importance of handling discontinuities in image registration, qualitative evaluation was performed in the synthetic images presenting sliding motion and DIR-lab dataset for both XFFD and FFD. In both datasets, the resulting transformed images and deformation field and volumetric strain field were visualised and compared.

Qualitative comparison between FFD and XFFD was also performed on the second synthetic dataset, presenting free discontinuous motion, by visualising the transformed grid.

3.5.3 Comparison with previous methods

Multiresolution XFFD was compared with previous methods tested in the two clinical datasets. The DIR-lab dataset was adopted in most of the previous methods treating discontinuities. The same measurements, TRE, gap and overlap volumes, were computed as reported in all the B-spline based methods [5,6,192] and some diffusion-based methods [187, 188, 190].

For a fairer comparison, XFFD was benchmarked against two previous methods [5, 6] using the same parameters and lung masks employed for XFFD on the DIR-lab dataset. Wu's method [5] was re-implemented and the implementation of Delmon's method [6] in Elastix [181] was employed.

In the second synthetic dataset, presenting free discontinuous motion, the experiments demonstrate that the proposed method is not restricted to sliding motion. This is complemented by the evaluation of the TRE in the liver dataset, subject to complex discontinuous motion in the abdomen. The results were compared with the two previous methods tested on the same dataset [188, 206], which handle sliding motion. Gap and overlap volumes were not relevant in this dataset, since some organs separate from the liver and sliding motion does not exist everywhere at the discontinuity interface.

3.6 Results

3.6.1 Comparison between FFD and XFFD: influence of incorporating discontinuous transformations

In the synthetic dataset presenting sliding motion, XFFD produced a more accurate transformed image than FFD, as the latter introduced artefacts, especially near the discontinuity (Fig. 3.4). The displacement field and transformed grid demonstrated that the discontinuities in the deformation field have been properly handled by XFFD, while FFD failed to do so. The displacements obtained from XFFD showed uniform rigid movement at the right side of the image, while the displacements were almost zero at the left side. This was in agreement with the actual deformation in the synthetic images. On the contrary, FFD generated artefacts in the displacement field near the discontinuity, which also influenced a larger neighbourhood. These errors in the deformation field can be propagated in quantities computed from the displacements, such as strain. The ideal strain field of this experiment should be zero across the whole image, as there is only rigid motion. However, because of its inability to treat discontinuities, FFD produced an unphysical volumetric strain field, in which the maximum value was 36.52, compared to 0.10 obtained from XFFD.

For the second synthetic dataset, the resulting transformed grid showed XFFD is able to handle free discontinuous motion, while FFD produced an unrealistic transformation (Fig. 3.7).

Similar results were obtained in the DIR-lab dataset (Fig. 3.5). XFFD showed the expected discontinuities in the deformation field, visible in the transformed grid. This is in agreement with the relatively large motion of the lungs and the very small vertical movement of the rib cage observed in the images. In contrast, for FFD, the transformed grid evidences artefacts near the discontinuity boundaries, as a result of imposing continuity indiscriminately. By properly handling discontinuities, XFFD avoided unphysical strains, which were present in the results of FFD. The maximum volumetric strain was 1037.32 in FFD, compared to 1.75 in XFFD. The color map in the figure was trimmed to the range [-1,5] for visualisation.

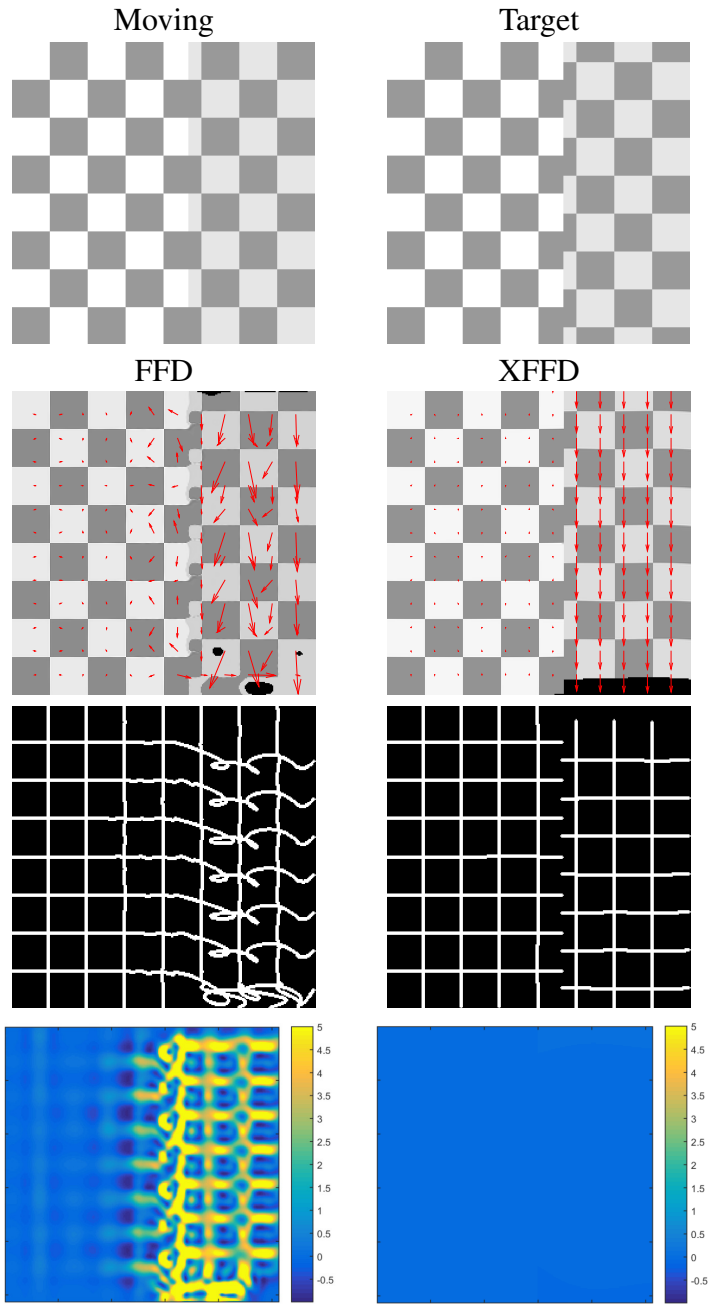

Figure 3.4: Results in synthetic dataset with sliding motion: moving and target images; 2nd row: transformed images overlaid with displacement fields obtained from FFD and XFFD; 3rd row: transformed grid obtained from FFD and XFFD; 4th row: strain fields obtained from FFD and XFFD. The color map in the figure was trimmed to the range [-1,5] for visualisation.

3.6.2 Comparison with previous methods

In the DIR-lab dataset, the TRE obtained with multiresolution XFFD was better than those of all previous methods [5, 6, 187, 188, 190, 192] in every subject (Table 3.5).

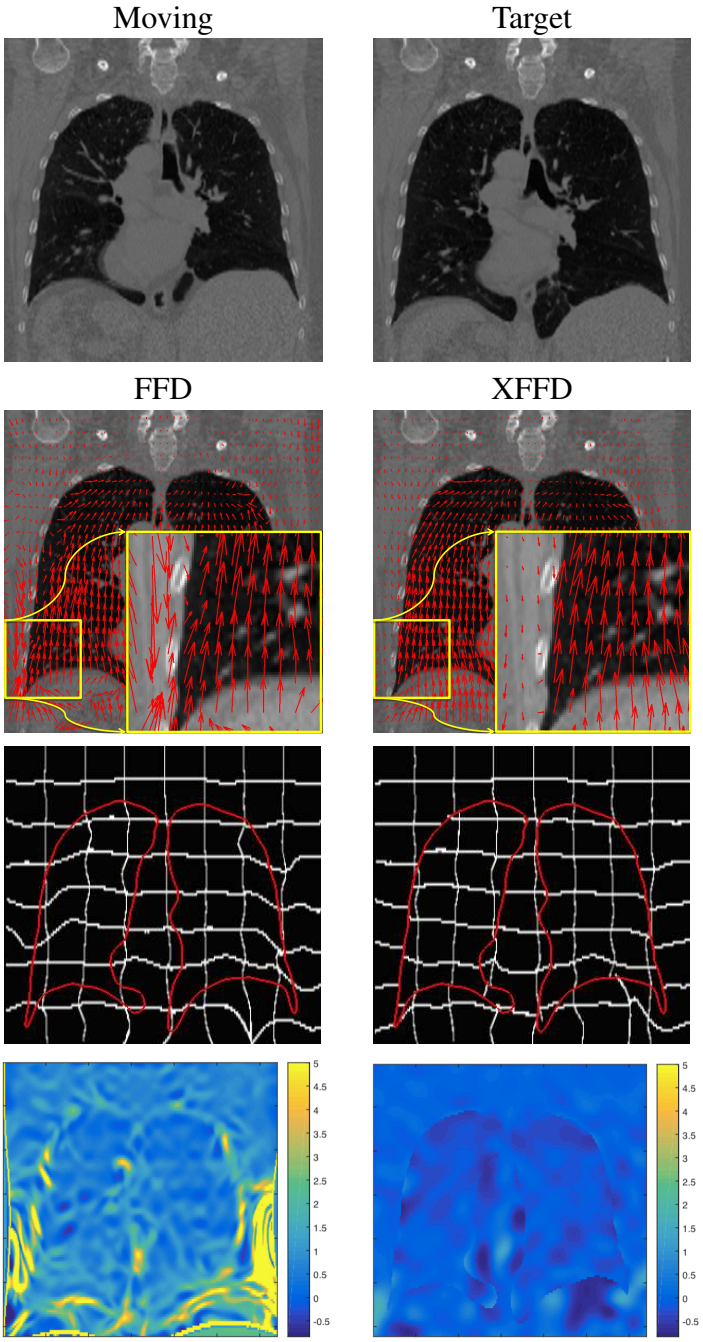

Figure 3.5: Qualitative results in DIR-lab dataset for sliding motion: 1st row: moving and target image; 2nd row: transformed images overlaid with displacement fields obtained from FFD and XFFD; 3rd row: transformed grid obtained from FFD and XFFD, surface mesh of discontinuity (red); 4th row: strain fields obtained from FFD and XFFD. The color map in the figure was trimmed to the range [-1,5] for visualisation, although the maximum value for FFD was 1037.32, compared to 1.75 in XFFD.

The average TRE was 1.17 mm, improving the best previous results by 14.0%. The resulting gap and overlap volumes were reasonable. Compared with the best previous method, the overlaps were reduced by 50%, but the gap volume was 22% larger (Table 3.6). Nevertheless, they correspond to an average surface-to-surface distance of 1.04 mm (standard deviation 1.09 mm) between the transformed meshes S^+ and S^-, which is comparable to the image resolution (1x1x2.5 mm^3).

Table 3.5: The mean and standard deviation of TRE in the DIR-lab dataset in comparison with other methods (mm)

Case	Before registration	Schmidt-Richberg (2012)	Pace (2013)	Papież (2014)	Wu (2008)	Delmon (2013)	Berendsen (2014)	XFFD
1	3.89 ± 2.78	1.22 ± 0.64	1.06 ± 0.57	1.05 ± 0.6	1.1 ± 0.5	1.2 ± 0.6	**1.00 ± 0.52**	**1.00 ± 0.51**
2	4.34 ± 3.90	1.14 ± 0.65	1.45 ± 1.00	1.08 ± 0.6	1.0 ± 0.5	1.1 ± 0.6	1.02 ± 0.57	**0.99 ± 0.59**
3	6.94 ± 4.05	1.36 ± 0.81	1.88 ± 1.35	1.49 ± 0.9	1.3 ± 0.7	1.6 ± 0.9	1.14 ± 0.89	**1.12 ± 0.64**
4	9.83 ± 4.86	2.68 ± 2.79	2.04 ± 1.40	1.90 ± 1.3	1.5 ± 1.0	1.6 ± 1.1	1.46 ± 0.96	**1.44 ± 1.03**
5	7.48 ± 5.51	1.57 ± 1.23	2.73 ± 2.13	1.99 ± 1.7	1.9 ± 1.5	2.0 ± 1.6	1.61 ± 1.48	**1.37 ± 1.35**
6	10.9 ± 6.97	2.21 ± 1.66	2.72 ± 2.04	2.36 ± 1.9	1.6 ± 0.9	1.7 ± 1.0	1.42 ± 0.89	**1.26 ± 1.04**
7	11.0 ± 7.43	3.81 ± 3.06	4.59 ± 3.41	2.32 ± 1.9	1.7 ± 1.1	1.9 ± 1.2	1.49 ± 1.06	**1.12 ± 0.67**
8	15.0 ± 9.01	3.42 ± 4.25	6.22 ± 5.69	3.58 ± 3.4	1.6 ± 1.4	2.2 ± 2.3	1.62 ± 1.71	**1.18 ± 1.22**
9	7.92 ± 3.98	1.83 ± 1.19	2.32 ± 1.42	1.74 ± 1.0	1.4 ± 0.8	1.6 ± 0.9	1.30 ± 0.76	**1.14 ± 0.64**
10	7.30 ± 6.35	2.06 ± 1.92	2.82 ± 2.50	2.02 ± 2.1	1.6 ± 1.2	1.7 ± 1.2	1.50 ± 1.31	**1.08± 0.82**
mean	8.46 ± 5.48	2.13 ± 1.82	2.78 ± 2.96	1.95 ± 0.7	1.47 ± 0.96	1.66 ± 1.14	1.36 ± 0.99	**1.17 ± 0.85**

Table 3.6: Gap/Overlap volumes in DIR-lab dataset in comparison with other methods (cm^3)

Case	Wu (2008)	Delmon (2013)	Berendsen (2014)	XFFD
1	38 / 26	39 / 15	**23** / 18	39 / **2**
2	78 / 46	**67** / 60	74 / 34	74 / **31**
3	99 / 28	83 / 33	**57** / 30	71 / **24**
4	75 / 34	**66** / 44	**66** / 28	92 / **13**
5	110 / 38	78 / 52	61 / 32	**54** / **6**
6	**100** / 86	119 / 77	130 / 50	155 / **11**
7	**105** / 79	108 / 77	119 / 45	138 / **19**
8	96 / 91	92 / 93	**85** / 53	150 / **40**
9	61 / 34	**54** / 44	70 / 51	58 / **14**
10	120 / 63	**94** / 56	80 / 43	109 / **28**
mean	88.2/52.5	80.0/55.1	**76.5**/37.4	94.0/ **18.8**

The TRE and gap and overlap volumes obtained from the methods in [5] and [6], but employing the same parameters and lung masks used for XFFD, are shown in Table 3.7. Both methods showed an improvement in the TRE compared to their reported results, but were still surpassed by XFFD. Wu's method also improved in the gap and overlap volumes. In contrast, Delmon's method showed a large increase in gap and overlap volumes, illustrating the limitation of the method in handling discontinuities

with non-smooth shapes.

Table 3.7: The average TRE and gap and overlap volumes using the same parameters, compared with [5] and [6].

	Wu (2008)	Delmon (2013)	XFFD
TRE (mm)	1.36 ± 1.61	1.38 ± 1.49	1.17 ± 0.85
gap/overlap (cm^3)	53.7/65.7	279.1/438.5	94.0/18.8

Similarly, in the liver dataset, the TRE obtained from XFFD improved on those from the two previous methods tested on the same dataset (Table 3.8), reducing the average TRE by 13% with respect to the best previous result. The obtained XFFD transformations are illustrated in Fig. 3.6 by the resulting grid deformation.

Table 3.8: The mean and standard deviation of TRE in the 4D CT liver dataset (mm)

Case	Before registration	Pace (2013)	Papież (2015)	XFFD
0	9.08 ± 2.89	2.06 ± 1.10	N/A	$\mathbf{1.54 \pm 0.87}$
1	5.89 ± 3.15	2.10 ± 1.23	N/A	$\mathbf{1.56 \pm 0.93}$
2	6.30 ± 2.76	2.55 ± 1.41	N/A	$\mathbf{2.25 \pm 1.28}$
4	4.42 ± 3.30	2.82 ± 1.92	N/A	$\mathbf{2.41 \pm 0.98}$
mean	6.64 ± 3.42	2.30 ± 1.45	2.19	$\mathbf{1.94 \pm 1.01}$

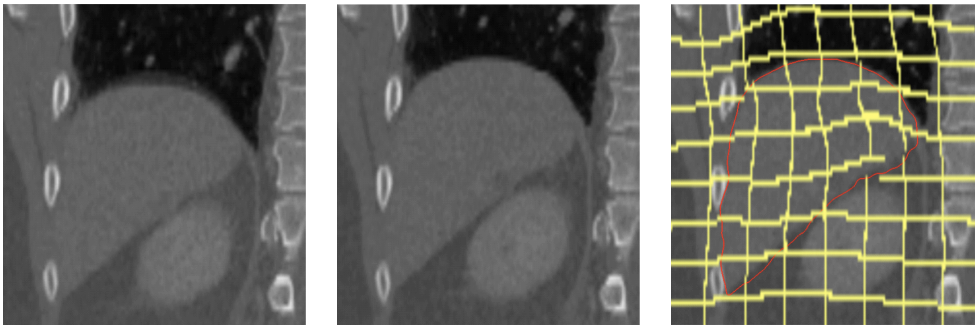

(a) (b) (c)

Figure 3.6: Transformed grid in the liver dataset: (a) moving image; (b) target image; (c) transformed grid overlay on moving image with liver boundary in red.

3.7 Discussion

Handling discontinuities in the deformation field is challenging. Attempts to address this issue have been based on direction-dependent or spatially varying regularisers

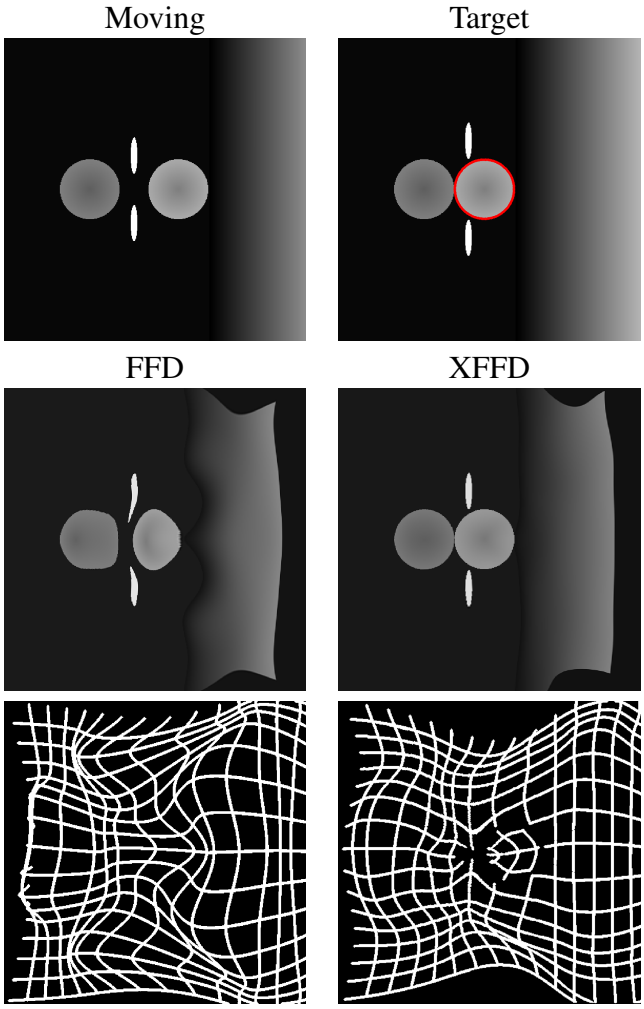

Figure 3.7: Results in synthetic dataset with free discontinuous motion: 1st row: moving image and target image with discontinuity interface (red); 2nd row: transformed images obtained with FFD and XFFD; 3rd row: transformed grid obtained from FFD and XFFD.

[179, 187–190], multiple B-spline transformations [5, 6], or penalty terms to reduce gaps and overlaps [192]. In contrast to these methods, XFFD handles this problem in the transformation model, such that the discontinuities are implicitly incorporated into a single B-spline transformation, while retaining all the desirable properties of B-splines. The proposed method imposes no constraint on the shape of the discontinuity interface and can handle free discontinuous motion. Other types of discontinuities, such as sliding motion, can be considered as constrained versions of this general type, according to the specific motion properties.

To demonstrate the significance of treating discontinuities in the deformation field, comparison was performed between the proposed method and FFD in the synthetic and DIR-lab dataset. In the synthetic dataset, the deformation can be described by a rigid body translation, having zero strain across the whole image. XFFD produced accurate displacements, correctly reflecting the physical properties of the actual deformation field, while FFD introduced unacceptable artefacts. These deficiencies were similarly exposed in the experiments on the lung images (Section 3.6.1).

For the purpose of benchmarking against previous methods, XFFD has been tested on two publicly available lung and liver datasets. In the lung dataset, the distribution of the average motion of the landmarks was 8.46 ± 5.58 mm. This represents large scale motion when compared to the small structures present in the lungs (airways), thus challenging the registration algorithm. Despite the complexity of the images, XFFD achieved high accuracy in both applications. The average TRE was 1.17 mm on the lung dataset and 1.94 mm on the liver images, which significantly improves on the performance of the previous methods handling discontinuities tested on the same datasets. In order to quantify the improvement in the results given by XFFD, the results of the two previous methods [5,6] were reproduced and compared with those of XFFD using the same parameters and lung masks only differing in the transformation model. This experiment confirms that the proposed transformation model is the key element in the higher accuracy obtained with XFFD.

XFFD does not involve any explicit control of gaps and overlaps. However, by using a single transformation, any misalignment is penalised, as it increases the image dissimilarity measure. Thus, the gap and overlap volumes obtained from XFFD were comparable to or better than the ones obtained from previous methods using *ad hoc* restrictions.

In this chapter, the goal is to develop a registration method, which handles discontinuities in the deformations. Different types of discontinuous motion can be observed in medical images, such as sliding motion, in which two organs are touching but not attached; and free discontinuous motion, where two organs are not attached and can touch and separate. Other types of discontinuities can also be observed, for instance in

the interface between tumours and the surrounding tissues, in which the two tissues are attached but having different material properties. To improve the performance in handling other types of discontinuities, different constraints or more specific enrichment functions can be included in the XFFD framework to adapt to a specific application.

In particular, XFFD does not include any constraint or penalty on the activation or the value of the enriched coefficients, $\boldsymbol{\lambda_J}$. Their values are driven in the registration only by the image similarity metric. This could result in instabilities or spurious discontinuities due to image noise, especially in homogeneous regions. The XFFD method could be extended to incorporate in the cost function a penalty term controlling $\boldsymbol{\lambda_J}$. This penalty could also be made location-dependent, restricting the discontinuity in regions of the interface which are known or expected to have nearly continuous motion.

Furthermore, regularisers are sometimes included in FFD to impose desired properties of the deformations, such as bending energy or incompressibility penalties. The regularisers often require derivatives of the transformation, which can be computed analytically in FFD. This property is also shared by XFFD. Thus, the proposed method is a flexible framework allowing inclusion of prior knowledge of the deformations via regularisers. In addition, any of the extensions of the FFD registration proposed in the past, such as spatio-temporal [3] and diffeomorphic registration [128], may be straightforwardly included in the proposed framework.

The computational complexity of XFFD is comparable to that of FFD. It only differs in that the enriched control points near the discontinuity interface have twice as many parameters as those in FFD. Thus, the number of extra parameters depends on the size and shape of the discontinuity interface, and on the resolution. Since the computational cost of one iteration of LBFGS increases linearly with respect to the number of parameters [204], the computational complexity of the XFFD is bounded to twice that of the FFD. In the experiments on the DIR-lab dataset, the average increase in the number of parameters across all the resolutions was 30%.

A limitation of XFFD is that it requires a segmentation in the target image. This requirement is, however, shared by all the other B-spline based methods [5, 6, 192]

and most of the diffusion-based methods [188, 207]. This may be facilitated by using an automatic segmentation method [208–210] as a previous step. Extensions of the presented method to enable automatic detection of the discontinuity boundaries during registration, without prior segmentation, are subjects of current research.

3.8 Conclusions

In this chapter, a novel registration framework, XFFD, is developed to handle discontinuous transformations that generally accompany tissue transitions. XFFD treats discontinuities within a single B-spline transformation, by enriching the basis functions to incorporate discontinuities across the considered tissue interfaces. XFFD has been integrated into a multiresolution framework using parameter upsampling.

XFFD does not incorporate any ad hoc penalty term conforming to a particular type of deformations. It has been tested on synthetic images, 3D lung and liver datasets along the respiratory cycle. The lungs follow sliding motion with respect to the rib cage, while the liver involves complex motions with respect to surrounding organs. In both datasets, XFFD showed high performance, compared to the state-of-the-art methods treating discontinuities tested on the same datasets.

In this chapter, the XFFD framework has been developed with the general discontinuity model, which allows the most freedom of the discontinuous motion. In the lung dataset, although XFFD showed good performance in terms of TRE and strain, this model does not correspond to the physical properties of the tissue transition involved. The most evident effect is that it permits the lungs to detach from the rib cage, which is not anatomically possible. This excessive freedom results in gap and overlap volumes that are not completely satisfying. The appropriate model should be more constrained, controlling the type of discontinuity according to the actual tissue transition present. In the next chapter, the tissue transitions and the associated discontinuity types are classified according to their physical and mathematical properties. The corresponding models and enrichment functions are developed and incorporated in XFFD.

Chapter 4

Anisotropic XFFD: dealing with orientation-dependent, generic tissue transitions

In the previous chapter, the XFFD framework with the most generic model was developed. This type of model allows the most freedom, while other types of models can be considered constrained versions of this general type. In this chapter, the different types of tissue transitions are studied and a classification of discontinuities is proposed considering also their directionality. This classification serves as the basis for the formulation of different transformation models, which are incorporated in the XFFD.

4.1 Motivation

Image registration is an essential technique for establishing material point correspondences between images acquired from different subjects, with different image modalities, or at different time points. When the images are from the same subject, the anatomical correspondence is expected to represent the same material point, following the motion and deformation of the tissues. Examples of such applications include temporal sequences at different cardiac or respiratory phases and images acquired at

different poses of the patient. In general, conventional non-rigid registration methods are based on the assumption that the deformation field is continuous and smooth across the entire image. This smoothness constraint is typically imposed by an explicit regularisation or a smooth transformation model. However, this assumption is only valid when the properties of the tissues vary continuously. When discontinuities are present at the tissue interfaces with different material properties or with relative motion across organ interfaces, the deformation field is not necessarily continuous nor smooth. In that case, imposing continuity and smoothness everywhere may lead to non-physical deformation fields, which deteriorates the accuracy of any quantity derived from the deformations (Fig. 4.6). One of these important quantities is the strain. Strain reflects tissue elastic properties and has been employed to evaluate normal or abnormal organ function or kinetics [19–22].

4.1.1 Tissue transition properties

Organs or tissues can have different material properties and be bound by different contact conditions. When these structures are subject to stretching or compression, different types of discontinuities may occur at their interface in the overall deformation field. Such discontinuities are present, for instance, in the respiratory motion of the lungs, which slide against the rib cage [211], at the boundary between myocardium and cardiac blood pool during cardiac motion or at the interfaces between abdominal organs under patient repositioning [212] or during respiratory motion [213].

There are a variety of discontinuities present in medical images involving different levels of complexity. In this chapter, a classification of discontinuities involved in tissue transitions is proposed by adapting the one from computational mechanics [197]. According to the contact conditions and the material properties of the interfacing tissues, discontinuities fall into three categories (Fig. 4.1):

Continuity: exists when the material properties are continuous across the interface and both parts are attached preventing relative motion. The deformation is then continuous with continuous first derivatives (C^1 continuous). This is considered a discontinuity class, as continuity could be present in one of the directional components in an

overall discontinuous tissue transition (Section 4.2.C).

Weak discontinuity: occurs at the transition of tissues that are attached to each other but have different material properties. Thus, the deformation is a continuous function but with discontinuous first derivatives at the transition (C^0 continuous, piecewise C^1).

Strong discontinuity: is present when two tissues can move freely and are able to separate from each other. The deformations are then discontinuous (piecewise C^0).

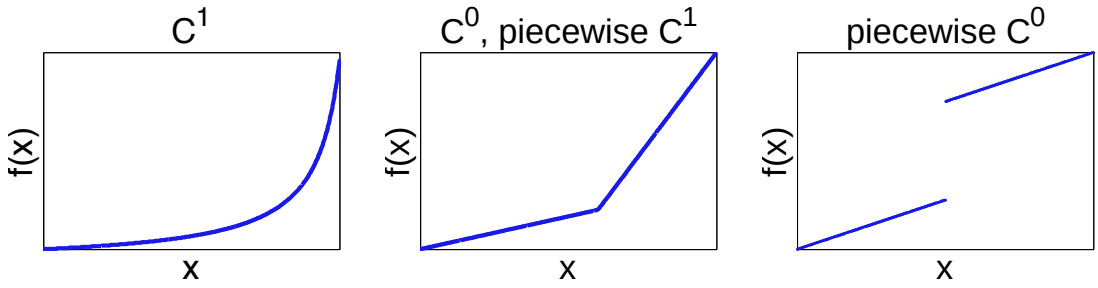

(a) (b) (c)

Figure 4.1: Classification of discontinuities: (a): continuity, (b) weak discontinuity, (c) strong discontinuity.

For a tissue transition, the type of discontinuity can vary depending on the direction with respect to the tissue interface. For instance, in the respiratory motion, a strong discontinuity exists in the tangential direction of the interface between the lungs and the rib cage, since the lungs move freely along the rib cage in this direction. In the normal direction, however, a weak discontinuity is present, since the lungs and rib cage keep in contact during deformation but they have different material properties. In this chapter, general models of tissue transitions are proposed to account for different types and directions of discontinuities.

4.1.2 Literature review

Although medical image registration has been an active area of research for over 25 years, only in the recent years, there have been limited efforts addressing discontinuous image registration. The efforts, however, are partial and with limited success. These

works, however, only modelled tissue transitions as strong discontinuities [5, 192] or are tailored to sliding motion [6, 187, 188, 207].

The most straightforward approach to handle discontinuities is to register each of the objects of interest individually and mask out the rest of the image. However, this can cause large gaps and overlaps at the boundary of the regions separated by the mask, since they are not penalised by the image similarity measure. Wu *et al.* [5] performed two independent registrations inside and outside the object of interest with a penalty term to reduce the boundary misalignment. Berendsen *et al.* [192] employed multiple B-spline transformations for different regions separated by a tissue interface. Gaps and overlaps between the regions are reduced using a penalty term that stitches together the transformations at the tissue interface. Papież *et al.* [190] employed the Demons framework replacing the conventional Gaussian smoothing by an adaptive regularisation. Thus, the smoothing weights are reduced for neighbouring voxels with large differences in image intensities or displacements. However, this criterion is neither based on a physical model of the tissues involved nor considers the directionality of the tissue transition.

Some other methods have been specifically proposed to model sliding motion as strong discontinuities along the tangential direction of the tissue interface and continuous transitions across the normal direction. Delmon *et al.* [6] employed multiple B-spline transformations, in which the displacements were decomposed into normal and tangential directions. However, the decomposition is performed at the B-spline control points instead of at the actual point location. The resulting normal and tangential directions interpolated at the tissue transition may thus be different from the actual directions. This is specifically the case for small structures involving discontinuities where the resulting deformations and strain are likely to be inaccurately recovered. Schmidt-Richberg *et al.* [187] proposed a direction-dependent regulariser acting in a narrow band near the discontinuity interface. Along the tangential direction, the two regions are smoothed individually, but in the normal direction, smoothing is applied across the boundary, which effectively imposes continuity across this direction. This idea was extended by Pace *et al.* [188] using a directional-dependent anisotropic dif-

fusion regulariser over the entire image domain. Risser *et al.* [207] extended the large deformation diffeomorphic metric mapping method [62] to handle sliding motion with piecewise-diffeomorphisms.

A common limitation of these methods is that they model sliding motion as a strong discontinuity along the tangential direction, while assuming continuity across the normal direction. However, this is only a particular case of sliding motion. In the human body, organs sliding to each other often have different material properties. Thus, modelling their discontinuity in the normal direction as weak discontinuity provides a more realistic representation. On the contrary, imposing continuity in this direction will introduce artefacts, which are specially evident in the strain fields, as shown in the results (i.e. Fig. 4.6 and 4.9).

In the literature, there is no general image registration method capable of handling different tissue transitions. Such method should treat each discontinuity type appropriately and account for different tissue transition behaviours in different directions.

In this chapter, anisotropic XFFD is developed to be a general framework for handling tissue transitions involving different types of discontinuities in different directions. Anisotropic XFFD is also integrated into a multiresolution scheme based on parameter upsampling, which allows to initialise the transformation parameters at a given resolution from those at the previous level.

Anisotropic XFFD has been tested on various synthetic images representing a diversity of tissue transition types. The purpose is to demonstrate the ability of anisotropic XFFD coping with general tissue transitions and the importance of modelling discontinuities correctly. Its applicability on clinical dataset has been illustrated on the DIR-lab dataset, a publicly available 3D lung CT dataset [23]. This dataset contains lung sliding motion, which offers a good example of a complex tissue transition, consisting of both strong and weak discontinuities in different directions. It is also a dataset in widespread use for benchmarking previous methods handling discontinuities.

4.2 Anisotropic eXtended Free Form Deformation

4.2.1 Conventional Free Form Deformation

Free Form Deformation (FFD) was initially proposed as a method to generate plausible deformations of 3D objects in computer graphics [84]. Later on, FFDs were introduced in nonrigid image registration as a transformation model based on B-splines, which ensure continuous and smooth deformations [18]. For any given point $\boldsymbol{x} = (x_1, \ldots, x_n) \in \mathbb{R}^n$, its displacement $\boldsymbol{D}(\boldsymbol{x})$ can be expressed as the linear combination of the B-spline basis functions $B_{\boldsymbol{I}}(\boldsymbol{x})$ weighted by the corresponding control point vectorial coefficients $\boldsymbol{\mu}_{\boldsymbol{I}}$:

$$\boldsymbol{D}(\boldsymbol{x}) = \sum_{\boldsymbol{I} \in \mathcal{C}} B_{\boldsymbol{I}}(\boldsymbol{x}) \boldsymbol{\mu}_{\boldsymbol{I}} \tag{4.1}$$

The index $\boldsymbol{I} = (I_1, \ldots, I_n)$ represents each element in a set of control points, $\mathcal{C}$, at position $\boldsymbol{x}_{\boldsymbol{I}} = \boldsymbol{x}_0 + \boldsymbol{I}\boldsymbol{L}$ in a regular grid with origin at $\boldsymbol{x}_0$ and spacings $\boldsymbol{L} = (L_1, \ldots, L_n)$. The basis functions $B_{\boldsymbol{I}}(\boldsymbol{x})$ are tensor products of 1D B-spline functions centered at each control point:

$$B_{\boldsymbol{I}}(\boldsymbol{x}) \equiv B\left(\frac{\boldsymbol{x} - \boldsymbol{x}_{\boldsymbol{I}}}{\boldsymbol{L}}\right) \equiv \prod_{i=1}^{n} \beta\left(\frac{x_i - x_{\boldsymbol{I},i}}{L_i}\right) \tag{4.2}$$

The most common B-spline basis functions are cubic B-splines [88], where:

$$\beta(u) = \begin{cases} \frac{2}{3} - \frac{1}{2}|u|^2(2 - |u|) & \text{if } |u| < 1 \\ \frac{1}{6}(2 - |u|)^3 & \text{if } 1 \leq |u| < 2 \\ 0 & \text{if } |u| \geq 2 \end{cases} \tag{4.3}$$

which is a piecewise cubic function with C^2-continuity.

4.2.2 Isotropic eXtended Free Form Deformation

The eXtended Free Form Deformation (XFFD) method employs concepts of the interpolation method of the eXtended Finite Element methods (XFEM) [197], which was developed to incorporate discontinuities, such as fractures at material interfaces, in the

standard FEM. The FEM is based on continuous interpolation at each element. Thus, it can only accounts for discontinuities by introducing a mesh conforming to the interface geometry. This continuous remeshing results in high computational cost for continuous remeshing to track the evolving discontinuities. The XFEM circumvents remeshing and encodes discontinuities by enriching the linear interpolation basis functions. The location of discontinuities interface can be described using a surface mesh or level sets, for instance.

Analogously, in XFFD, an enrichment term is introduced to the conventional FFD formalism [214]:

$$\boldsymbol{D}(\boldsymbol{x}) = \sum_{\boldsymbol{I}\in\mathcal{C}} B_{\boldsymbol{I}}(\boldsymbol{x})\boldsymbol{\mu}_{\boldsymbol{I}} + \sum_{\boldsymbol{J}\in\widetilde{\mathcal{C}}} M_{\boldsymbol{J}}(\boldsymbol{x})\boldsymbol{\lambda}_{\boldsymbol{J}} \tag{4.4}$$

where $\boldsymbol{\lambda}_{\boldsymbol{J}}$ represents additional degrees of freedom for the subset of control points $\boldsymbol{J} \in \widetilde{\mathcal{C}}$ whose support intersects with the tissue interface. The enriched basis function can be expressed as:

$$M_{\boldsymbol{J}}(\boldsymbol{x}) = B_{\boldsymbol{J}}(\boldsymbol{x})\,\psi(\boldsymbol{x}) \tag{4.5}$$

where $\psi(\boldsymbol{x})$ is the enrichment function, which encodes the target discontinuity class.

The mathematical properties of the enrichment function should be able to model the discontinuity type at the interface. The location of the interface can be described either directly by an n-dimensional hyper-surface, S, or by a level set function, $\phi(\boldsymbol{x})$. This interface will split the image into regions that, in general, can be interpreted as inside and outside an object of interest.

For strong discontinuities, the enrichment function should be continuous except at the tissue interface, S, exhibiting a jump in the function's value. Thus, a natural candidate for strong-discontinuity enrichment function is the sign function.

$$\psi_{\text{strong}}(\boldsymbol{x}) = \text{sign}(\phi(\boldsymbol{x})) = \begin{cases} -1 & \text{if } \boldsymbol{x} \text{ is inside} \\ \\ 1 & \text{if } \boldsymbol{x} \text{ is outside} \end{cases} \tag{4.6}$$

For weak discontinuities, the enrichment function must be continuous but with discontinuous derivatives across the tissue interface, and continuous and smooth elsewhere. A natural candidate satisfying these properties is the absolute value of the level

set function:

$$\psi_{\text{weak}}(\boldsymbol{x}) = |\phi(\boldsymbol{x})| \tag{4.7}$$

In case the interface is described by a surface mesh, a corresponding level set function can be obtained from its signed distance transform [215]. Observe that the distance transform can be non-smooth outside a neighbourhood of the surface. Thus, a smoothed approximation should be considered, but ensuring that it preserves the location of the zero level. This can be obtained, for instance, by the algorithm presented in [215], based on a distance-dependent Gaussian filter.

Fig. 4.2 presents 1D examples of strong and weak enriched basis functions. For both types of discontinuities, the enriched basis functions preserve the C^2-continuity property of cubic B-splines, except at the intended tissue interface. This allows a smooth transition between enriched and non-enriched basis, without introducing undesired discontinuities.

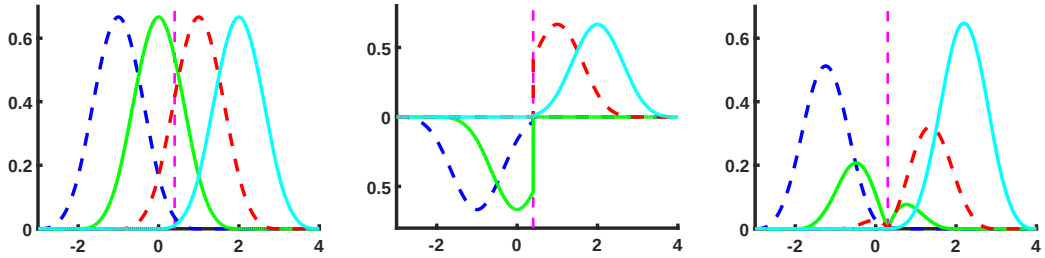

(a) (b) (c)

Figure 4.2: Enriched B-spline basis functions in the vicinity of a discontinuity, indicated by a pink dashed line: (a) Conventional basis functions; (b) Enriched basis functions for strong discontinuity; (c) Enriched basis functions for weak discontinuity.

4.2.3 Anisotropic Extended Free Form Deformation

In this chapter, a general formulation of the anisotropic enrichment function is developed. Equation (4.4) defines the transformation with isotropic enrichment, assuming the discontinuity type is independent of the direction of the deformation. However, the actual deformations may exhibit different behaviours in different directions relative to the orientation of the tissue interface (e.g. tangential versus normal direction of the

interface). Thus, XFFD is developed to incorporate anisotropic discontinuities. For that, the enrichment function (4.4) can be extended to a tensorial function:

$$\boldsymbol{D}(\boldsymbol{x}) = \sum_{\boldsymbol{I}\in\mathcal{C}} B_{\boldsymbol{I}}(\boldsymbol{x})\boldsymbol{\mu}_{\boldsymbol{I}} + \sum_{\boldsymbol{J}\in\widetilde{\mathcal{C}}} \boldsymbol{M}_{\boldsymbol{J}}(\boldsymbol{x})\boldsymbol{\lambda}_{\boldsymbol{J}} \tag{4.8}$$

where

$$\boldsymbol{M}_{\boldsymbol{J}}(\boldsymbol{x}) = B_{\boldsymbol{J}}(\boldsymbol{x})\boldsymbol{\Psi}(\boldsymbol{x}) \tag{4.9}$$

is a symmetric matrix. The anisotropic enrichment allows to introduce diverse enrichment functions according to the tissue transition properties relative to the orientation with respect to the tissue interface. One specific and useful case is the differentiation between the normal and tangential directions of the tissue interface. In this case, the anisotropic enrichment function is given by

$$\boldsymbol{\Psi}(\boldsymbol{x}) = \psi^{\perp}(\boldsymbol{x})\boldsymbol{P}^{\perp}(\boldsymbol{x}) + \psi^{\parallel}(\boldsymbol{x})\boldsymbol{P}^{\parallel}(\boldsymbol{x})$$

where

$$\boldsymbol{P}^{\perp}(\boldsymbol{x}) = \hat{\boldsymbol{n}}(\boldsymbol{x}) \otimes \hat{\boldsymbol{n}}(\boldsymbol{x}) \quad \text{and} \quad \boldsymbol{P}^{\parallel}(\boldsymbol{x}) = \mathbf{1} - \boldsymbol{P}^{\perp}(\boldsymbol{x})$$

are the normal and tangential projectors, respectively. The normal direction vector field $\hat{\boldsymbol{n}}(\boldsymbol{x})$ must be defined in the support of the set of enriched basis functions around the tissue interface. A natural way to produce the normal direction filed is to compute the gradient of the level set function:

$$\boldsymbol{n}(\boldsymbol{x}) = \nabla\phi(\boldsymbol{x}), \qquad \hat{\boldsymbol{n}}(\boldsymbol{x}) = \frac{\boldsymbol{n}(\boldsymbol{x})}{\|\boldsymbol{n}(\boldsymbol{x})\|} \tag{4.10}$$

For isotropic discontinuities, either weak or strong, their enrichment function is also isotropic $\psi^{\perp}(\boldsymbol{x}) = \psi^{\parallel}(\boldsymbol{x}) \equiv \psi(\boldsymbol{x})$. Thus, the tensorial enrichment function can be simplified to the scalar one (4.4):

$$\boldsymbol{\Psi}(\boldsymbol{x}) = \psi(\boldsymbol{x})\mathbf{1} \quad \Rightarrow \quad \boldsymbol{\Psi}(\boldsymbol{x})\boldsymbol{\lambda}_{\boldsymbol{J}} = \psi(\boldsymbol{x})\boldsymbol{\lambda}_{\boldsymbol{J}}$$

The following enrichment functions are proposed to account for the different types of

discontinuities relevant for various medical image registration cases, considering the directionality of the tissue transition properties (Fig. 4.3).

Isotropic strong: the transition between two tissues moving freely from each other is characterized by an isotropic strong discontinuity. The enrichment function is

$$\psi(\boldsymbol{x}) = \psi_{\text{strong}}(\boldsymbol{x})$$

This is observed, for instance, when the liver and some surrounding organs touch and separate during respiratory cycle (Fig. 4.4 (a)).

Isotropic weak: the tissue transition between attached objects with no possible relative motion at the interface but with different material properties. The enrichment function is

$$\psi(\boldsymbol{x}) = \psi_{\text{weak}}(\boldsymbol{x})$$

This can be found, for example, in the transition between a vertebrae and a intervertebral disc (Fig. 4.4 (b)), as a vertebra is rigid and the intervertebral disc is elastic [216].

Strong-continuous: the transition between two tissues having the same material properties but being able to move relatively to each other along the tangential direction of their interface without losing contact in the normal direction. The deformation undergoes strong discontinuities in the tangential direction and continuity in the normal direction:

$$\psi^{\perp}(\boldsymbol{x}) = 0 \qquad \text{and} \qquad \psi^{\parallel}(\boldsymbol{x}) = \psi_{\text{strong}}(\boldsymbol{x})$$

This model has been assumed in all the previous works explicitly modelling the sliding motion present in the lung respiratory cycle [6, 187, 188]. However, this assumption is incorrect, since the lungs and the ribs have different material properties [217].

Strong-weak: the transition between two tissues of different material properties that can move relatively to each other along the tangential direction of their interface without losing contact in the normal direction. The enrichment function is:

$$\psi^{\perp}(\boldsymbol{x}) = \psi_{\text{weak}}(\boldsymbol{x}) \qquad \text{and} \qquad \psi^{\parallel}(\boldsymbol{x}) = \psi_{\text{strong}}(\boldsymbol{x})$$

This type of discontinuity has never been explicitly modelled before. One typical example is the lung sliding motion against the thoracic cage (Fig. 4.4 (c)).

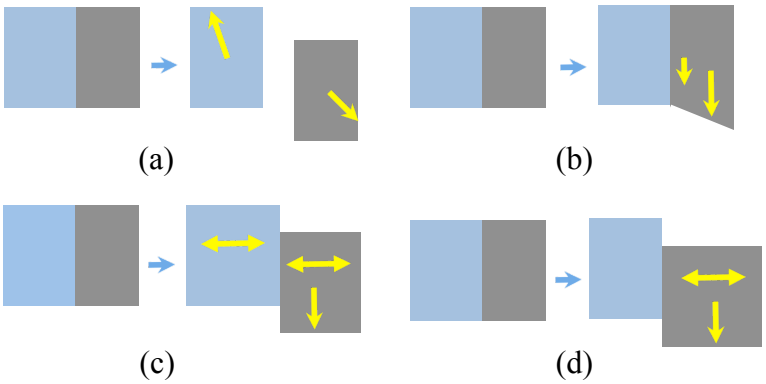

Figure 4.3: Examples of different types of discontinuous motion: (a) isotropic strong; (b) isotropic weak; (c) strong-continuous; (d) strong-weak.

Figure 4.4: Examples of different tissue transitions: (a): Respiration-induced motion of the liver and kidney, (b) vertebrae and intervertebral discs, (c) lungs and rib cage.

4.2.4 Multiresolution registration

Multiresolution strategy is commonly employed in image registration, involving multiple scales of both image resolution and control point grid. It is more efficient than single-resolution and helps to avoid the optimiser to be trapped at a local minimum [218]. In the multi-resolution grids, the transformation parameters at a given scale can be upsampled to initialise those at the next finer level. This process is referred to as *parameter upsampling*.

A common strategy to upsample the deformation grid to a finer level is to insert

additional control points between those at the previous scale, thus halving the grid spacing [18]. With this protocol, there is a unique exact solution for the parameter upsampling of the conventional B-splines. Cubic B-splines are piecewise polynomial consisting of four segments segments, given by the intervals between successive control points, with smooth transition between the segments (4.3). The upsampled basis are also piecewise polynomials. The function $\beta(u)$ can be exactly represented by a linear combination of the upsampled functions:

$$\beta(u) = \sum_{k=-2}^{2} A_k \, \beta(2u - k) \tag{4.11}$$

To solve for the constants A_k, a system of linear equations for A_k can be obtained by separating the the functional equation (4.11) into eight components in the intervals divided by the upsampled control points, resulting in eight polynomial equations for five unknowns. This system is overconstrained but it is consistent and has the unique solution (Fig. 4.5 (a))

$$A_{-2} = A_2 = \frac{1}{8}, \quad A_{-1} = A_1 = \frac{1}{2}, \quad A_0 = \frac{3}{4}. \tag{4.12}$$

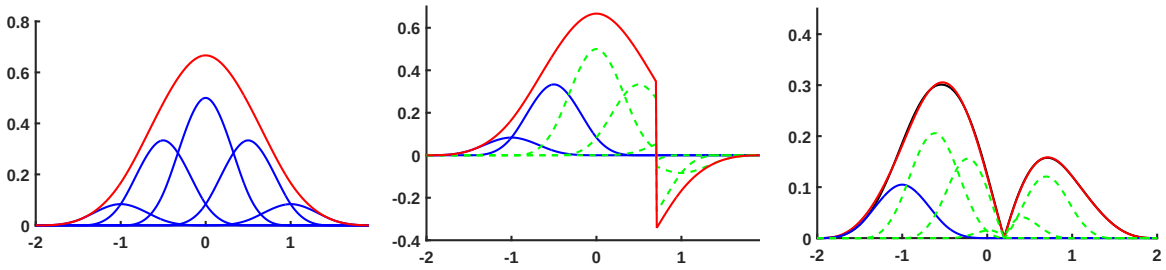

(a) (b) (c)

Figure 4.5: 1D B-spline basis functions, represented by the ones in the upsampled grid with half grid spacing: (a) a non-enriched B-spline basis function in the original grid (red) can be represented by non-enriched basis functions in the upsampled grid (blue); (b) strong enriched basis in the original grid (red) represented by non-enriched basis functions (blue) and enriched ones (dashed green) in the upsampled grid. (c) weak enriched basis in the original grid (red) coincides with the approximation of the original basis using upsampling (black).

The analogue of n-dimensional B-spline basis functions for upsampled grid can be directly derived by inserting (4.11) into (4.2)

$$\begin{aligned} B_{\boldsymbol{I}}(\boldsymbol{x}) &= \prod_{i=1}^{n} \beta\left(\frac{x_i - x_{I,i}}{L_i}\right) \\ &= \sum_{k_1=-2}^{2} \cdots \sum_{k_n=-2}^{2} \prod_{i=1}^{n} A_{k_i}\, \beta\left(2\frac{x_i - x_{\boldsymbol{I},i}}{L_i} - k_i\right) \end{aligned} \tag{4.13}$$

This expression can be simplified by representing the control point position with respect to the grid origin: $\boldsymbol{x_I} = \boldsymbol{x_0} + \boldsymbol{IL}$. Besides, defining $A_k = 0$ for $|k| > 2$ and $A_{\boldsymbol{k}} = A_{k_1} \times \cdots \times A_{k_n}$ leads to

$$\begin{aligned} B_{\boldsymbol{I}}(\boldsymbol{x}) &= \sum_{\boldsymbol{k}} A_{\boldsymbol{k}} \prod_{i=1}^{n} \beta\left(\frac{x_i - x_{\boldsymbol{0},i}}{L_i/2} - 2I_i - k_i\right) \\ &= \sum_{\boldsymbol{k}} A_{\boldsymbol{k}} B^{\uparrow}_{2\boldsymbol{I}+\boldsymbol{k}}(\boldsymbol{x}) \\ &= \sum_{\boldsymbol{I}^{\uparrow} \in \mathcal{C}^{\uparrow}} A_{\boldsymbol{I}^{\uparrow}-2\boldsymbol{I}} B^{\uparrow}_{\boldsymbol{I}^{\uparrow}}(\boldsymbol{x}), \end{aligned} \tag{4.14}$$

where the upsampled functions, coefficients and sets are denoted by the superscript $\uparrow$.

Accordingly, the tensorial enriched basis functions can be expressed as:

$$\begin{aligned} \boldsymbol{M_J}(\boldsymbol{x}) &= \sum_{\boldsymbol{I}^{\uparrow} \in \mathcal{C}^{\uparrow}} A_{\boldsymbol{I}^{\uparrow}-2\boldsymbol{J}} B^{\uparrow}_{\boldsymbol{I}^{\uparrow}}(\boldsymbol{x}) \boldsymbol{\Psi}(\boldsymbol{x}) \\ &= \sum_{\boldsymbol{J}^{\uparrow} \in \tilde{\mathcal{C}}^{\uparrow}} A_{\boldsymbol{J}^{\uparrow}-2\boldsymbol{J}} \boldsymbol{M}^{\uparrow}_{\boldsymbol{J}^{\uparrow}}(\boldsymbol{x}) + \sum_{\boldsymbol{I}^{\uparrow} \in \mathcal{C}^{\uparrow} \setminus \tilde{\mathcal{C}}^{\uparrow}} A_{\boldsymbol{I}^{\uparrow}-2\boldsymbol{J}} B^{\uparrow}_{\boldsymbol{I}^{\uparrow}}(\boldsymbol{x}) \boldsymbol{\Psi}(\boldsymbol{x}) \end{aligned} \tag{4.15}$$

In this equation, two different types of terms appear, depending on whether or not the upsampled control point is enriched. This occurs because the support region of enrichment decreases at a finer scale and only the minimum necessary number of enriched control points are employed for supporting the points at the discontinuities. For the enriched upsampled control points, $\boldsymbol{J}^{\uparrow} \in \tilde{\mathcal{C}}^{\uparrow}$, the product of the upsampled basis $B^{\uparrow}_{\boldsymbol{J}^{\uparrow}}(\boldsymbol{x})$ with the enrichment function $\boldsymbol{\Psi}(\boldsymbol{x})$ produces the corresponding enriched basis function $\boldsymbol{M}^{\uparrow}_{\boldsymbol{J}^{\uparrow}}(\boldsymbol{x})$. However, for the non-enriched upsampled control points, $\boldsymbol{I}^{\uparrow} \in \mathcal{C}^{\uparrow} \setminus \tilde{\mathcal{C}}^{\uparrow}$, the equivalent identity does not hold. For these terms, a unique exact

expression in terms of the upsampled basis functions may or may not exist, depending on the type of enrichment.

In case of the isotropic strong enrichment, $\boldsymbol{\Psi}(\boldsymbol{x})$ can be simplified to a scalar, $\psi(\boldsymbol{x})$, which is constant in the whole support of $B^{\uparrow}_{\boldsymbol{I}^{\uparrow}}(\boldsymbol{x})$ for any $\boldsymbol{I}^{\uparrow} \in \mathcal{C}^{\uparrow} \backslash \tilde{\mathcal{C}}^{\uparrow}$. Thus, a unique exact solution can be obtained:

$$M_{\boldsymbol{J}}(\boldsymbol{x}) = \sum_{\boldsymbol{J}^{\uparrow} \in \widetilde{\mathcal{C}}^{\uparrow}} A_{\boldsymbol{J}^{\uparrow}-2\boldsymbol{J}} M^{\uparrow}_{\boldsymbol{J}^{\uparrow}}(\boldsymbol{x}) + \sum_{\boldsymbol{I}^{\uparrow} \in \mathcal{C}^{\uparrow}} S_{\boldsymbol{I}^{\uparrow}} A_{\boldsymbol{I}^{\uparrow}-2\boldsymbol{J}} B^{\uparrow}_{\boldsymbol{I}^{\uparrow}}(\boldsymbol{x}) \tag{4.16}$$

where

$$S_{\boldsymbol{I}^{\uparrow}} = \begin{cases} -1 & \text{if } \boldsymbol{x}_{\boldsymbol{I}^{\uparrow}} \text{ is inside and } \boldsymbol{I}^{\uparrow} \notin \widetilde{\mathcal{C}}^{\uparrow} \\ 1 & \text{if } \boldsymbol{x}_{\boldsymbol{I}^{\uparrow}} \text{ is outside and } \boldsymbol{I}^{\uparrow} \notin \widetilde{\mathcal{C}}^{\uparrow} \\ 0 & \text{if } \boldsymbol{I}^{\uparrow} \in \widetilde{\mathcal{C}}^{\uparrow}. \end{cases} \tag{4.17}$$

In contrast, for isotropic weak or anisotropic discontinuity, $\boldsymbol{\Psi}(\boldsymbol{x})$ is not constant for each control point $\boldsymbol{I}^{\uparrow} \in \mathcal{C}^{\uparrow} \setminus \widetilde{\mathcal{C}}^{\uparrow}$. Thus, no exact expression of the enriched basis function exists in the upsampled basis. The best approximation in a least-square sense implies minimizing an integral in the full image domain which would involve all the upsampled parameters. This approximation is computationally expensive and numerically unstable, given the large number of parameters to estimate. Alternatively, a stable and efficient approximation is developed. For each non-enriched control point $\boldsymbol{I}^{\uparrow} \in \mathcal{C}^{\uparrow} \setminus \widetilde{\mathcal{C}}^{\uparrow}$, the corresponding product can be approximated by substituting the enrichment function by its central value at the control point location: $B^{\uparrow}_{\boldsymbol{I}^{\uparrow}}(\boldsymbol{x})\boldsymbol{\Psi}(\boldsymbol{x}) \simeq B^{\uparrow}_{\boldsymbol{I}^{\uparrow}}(\boldsymbol{x})\boldsymbol{\Psi}(\boldsymbol{x}_{\boldsymbol{I}^{\uparrow}})$. This gives the expression

$$\boldsymbol{M}_{\boldsymbol{J}}(\boldsymbol{x}) \simeq \sum_{\boldsymbol{J}^{\uparrow} \in \tilde{\mathcal{C}}^{\uparrow}} A_{\boldsymbol{J}^{\uparrow}-2\boldsymbol{J}} \boldsymbol{M}^{\uparrow}_{\boldsymbol{J}^{\uparrow}}(\boldsymbol{x}) + \sum_{\boldsymbol{I}^{\uparrow} \in \mathcal{C}^{\uparrow}} A_{\boldsymbol{I}^{\uparrow}-2\boldsymbol{J}} B^{\uparrow}_{\boldsymbol{I}^{\uparrow}}(\boldsymbol{x}) \boldsymbol{S}_{\boldsymbol{I}^{\uparrow}} \tag{4.18}$$

where

$$\boldsymbol{S}_{\boldsymbol{I}^{\uparrow}} = \begin{cases} \boldsymbol{\Psi}(\boldsymbol{x}_{\boldsymbol{I}^{\uparrow}}) & \text{if } \boldsymbol{I}^{\uparrow} \in \mathcal{C}^{\uparrow} \setminus \tilde{\mathcal{C}}^{\uparrow} \\ \mathbf{0} & \text{if } \boldsymbol{I}^{\uparrow} \in \tilde{\mathcal{C}}^{\uparrow} \end{cases}$$

Substituting (4.14) and (4.18) into (4.8), the displacement can be expressed as

$$\begin{aligned}\boldsymbol{D}(\boldsymbol{x}) \simeq & \sum_{\boldsymbol{I}\in\mathcal{C}} \sum_{\boldsymbol{I}^{\uparrow}\in\mathcal{C}^{\uparrow}} B^{\uparrow}_{\boldsymbol{I}^{\uparrow}}(\boldsymbol{x}) A_{\boldsymbol{I}^{\uparrow}-2\boldsymbol{I}} \boldsymbol{\mu}_{\boldsymbol{I}} + \sum_{\boldsymbol{J}\in\tilde{\mathcal{C}}} \sum_{\boldsymbol{J}^{\uparrow}\in\tilde{\mathcal{C}}^{\uparrow}} \boldsymbol{M}^{\uparrow}_{\boldsymbol{J}^{\uparrow}}(\boldsymbol{x}) A_{\boldsymbol{J}^{\uparrow}-2\boldsymbol{J}} \boldsymbol{\lambda}_{\boldsymbol{J}} \\ & + \sum_{\boldsymbol{J}\in\tilde{\mathcal{C}}} \sum_{\boldsymbol{I}^{\uparrow}\in\mathcal{C}^{\uparrow}} B^{\uparrow}_{\boldsymbol{I}^{\uparrow}}(\boldsymbol{x}) A_{\boldsymbol{I}^{\uparrow}-2\boldsymbol{J}} \boldsymbol{S}_{\boldsymbol{I}^{\uparrow}} \boldsymbol{\lambda}_{\boldsymbol{J}} \\ = & \sum_{\boldsymbol{I}^{\uparrow}\in\mathcal{C}^{\uparrow}} B^{\uparrow}_{\boldsymbol{I}^{\uparrow}}(\boldsymbol{x}) \boldsymbol{\mu}_{\boldsymbol{I}^{\uparrow}} + \sum_{\boldsymbol{J}^{\uparrow}\in\tilde{\mathcal{C}}^{\uparrow}} \boldsymbol{M}^{\uparrow}_{\boldsymbol{J}^{\uparrow}}(\boldsymbol{x}) \boldsymbol{\lambda}_{\boldsymbol{J}^{\uparrow}}\end{aligned} \tag{4.19}$$

4.3 Materials and experiments

4.3.1 Materials

To evaluate the effectiveness of anisotropic XFFD, three synthetic datasets were created emulating different types of discontinuous motion. In addition, a publicly available clinical dataset was also employed for the evaluation.

Synthetic dataset

Synthetic images were created to mimic different types of discontinuities that could be found in medical images, such as strong-weak, strong-continuous and isotropic weak discontinuity. All the images are in 2D with 256×256 pixels.

Strong-weak dataset: The images contain two regions: left and right (Fig. 4.6).From the target to the moving image, the right region was shifted vertically and compressed homogeneously in the horizontal direction, while the left region is static, presenting a strong-weak discontinuity.

Strong-continuous dataset: Similar to the strong-weak dataset, these images contain two regions (Fig. 4.7). The discontinuity was created by shifting the rightmost region vertically and compressing both regions in the horizontal direction.

Isotropic weak dataset: the images contain a circle and a set of concentric rings (Fig. 4.8). The circle (interior region) remains static while the rings (exterior regions) are expanded.

Dir-lab dataset

This dataset contains 4D lung CT images of 10 subjects. This dataset is a good candidate for evaluating anisotropic XFFD, as it involves complex deformations, including both weak and strong discontinuities and with directional dependence. The in-plane resolution of the images is between $0.97 \times 0.97\,\text{mm}^2$ and $1.16 \times 1.16\,\text{mm}^2$ and the inter-slice resolution is 2.5 mm. For each subject, 300 landmarks are provided for inhale and exhale phases annotated by experts with inter-observer variability around 1 mm [23, 219]. Masks covering the lungs were created by Delmon et al. [6] using an automatic segmentation method [220].

4.3.2 Evaluation metrics

Target Registration Error

Target Registration Error (TRE) measures the registration accuracy based on landmarks manually located in salient structures. It is defined as the Euclidean distance between the groundtruth landmarks in the moving image and transformed landmarks from the target space to the moving one using the obtained transformation from registration. In previous registration methods applied to the DIR-lab dataset [5, 6, 187, 188, 190, 192, 214], the mean and standard deviation of the TRE of all the landmarks were reported for each subject.

Gap and overlap volumes

The boundary matching of two regions, defined inside and outside the discontinuity surface, are assessed by the gap and overlap volumes [5, 6, 192, 214]. Large values of this metric indicate misalignment of the boundaries of the two regions, which may result in undesired artefacts in the transformed image and resulting deformation field.

Strain

From the deformation field obtained from the registration, the corresponding strain field can be computed. The strain is related to the material properties of the tissues in-

volved and is a significant clinical measurement to many diagnostic questions [19, 21]. Strain is also more sensitive to local variations of the deformations. Thus, it is a good indicator to evaluate the importance of modelling the registration with the appropriate type of discontinuity. Volumetric strain measures the expansion or compression of the tissue [205] and is given by the determinant of the Jacobian of the deformations. The perpendicular strain is the projection of the Lagrangian strain tensor to the direction normal to the interface.

4.3.3 Implementation details

The proposed method was implemented as a new transformation module in the Elastix toolkit [181], which allows a fair comparison with other methods implemented in the same platform [6, 192]. Elastix is a publicly available software platform for intensity-based medical image registration. It consists of a collection of image registration algorithms [181]. The modular design of Elastix allows the user to quickly test and compare different algorithms for each component of image registration and to select the best one for a specific application.

The Elastix code is written in C++ and it is based on the Insight Segmentation and Registration Toolkit (ITK) [196]. It consists of two layers: 1) ITK-style classes that implement image registration functionality, and 2) Elastix wrappers that take care of connecting components, receiving inputs and saving results, and similar "administrative" tasks [221]. To develop a new module, a first layer class should be created to implement the algorithm. Subsequently, a second layer wrapper needs to be written to connect the first layer class to the other parts of Elastix.

In this thesis, the proposed methods have been implemented as transformation modules, inheriting from the mother class in Elastix. In addition, the derivatives of the transformations were implemented for the optimisation as well as the upsampling methods for the multiresolution scheme. The rest of the registration components, such as similarity measure and optimisation, were selected from existing Elastix modules.

In the registration experiments, the anisotropic XFFD was adopted as the transformation model, normalized cross-correlation as similarity metric, for its robustness

to linear variations in image intensity [203], and Limited memory Broyden-Fletcher-Goldfarb-Shanno (LBFGS) as the optimiser, due to its high performance in high-dimensional problems [204].

On the DIR-lab dataset, for the comparison with the previous methods, the registration parameters were selected to be similar to those from [192] (Table 3.1). Five scales were chosen in the multiresolution scheme. At each resolution, the grid spacing is halved from that at the previous scale. Correspondingly, the images were smoothed and downsampled using a Gaussian smoothing pyramid, with standard deviation, σ, halved from the one at the previous scale. Thus, for the five scales, The grid spacing was set to be (80, 80, 40, 20, 10) mm, and the smoothing $\sigma = (16, 8, 4, 2, 1)$ voxels in the axial plane and $\sigma = (8, 4, 2, 1, 0)$ voxels in the perpendicular direction to accommodate the difference of image spacing in each dimension. For the synthetic datasets, 2 scales were employed with isotropic grid spacing of (128, 64) pixels and smoothing with $\sigma = (2, 1)$ pixels, respectively (Table 4.1).

Table 4.1: Parameters for experiments on synthetic datasets

Parameters	Values	Function
Number of scales	2	number of scales of image pyramids
standard deviation (σ)	(2, 1) pixels	standard deviation of Gaussian smoothing
grid spacing	(128, 64) pixels	grid spacing of grid pyramids

4.3.4 Experiments

The goal of the experiments is to demonstrate the ability of anisotropic XFFD in handling general tissue transitions involving discontinuities and the significance of modelling the discontinuities with the correct type. Thus, XFFD with the appropriate discontinuity type is compared with FFD and XFFD with a related but incorrect type.

Experiments on synthetic datasets

Each dataset is registered using FFD, strong-continuous XFFD, strong-weak XFFD, and isotropic weak XFFD. The results are compared by visually inspecting the transformed grid and the volumetric strain field, and quantitatively evaluated with the max-

imum absolute error of the volumetric strain.

Experiments on DIR-lab dataset

DIR-lab dataset involves strong-weak discontinuity, which is the most complex type. In the literature, previous methods modelled the lung motion using a simpler strong-continuous model [6, 187, 188, 207]. However, this incorrect model generates clearly observable artefacts in the strain. To illustrate this issue, perpendicular strain is computed and visualised for the FFD, the strong-weak XFFD and the strong-continuous XFFD. Besides, the TRE [5, 6, 187, 188, 190, 192, 214], gap and overlap volumes [5, 6, 192, 214] were also computed and compared to those from previous methods.

4.4 Results

4.4.1 Experiments on synthetic datasets

In the synthetic datasets representing strong-weak and strong-continuous discontinuity types (Fig. 4.6, 4.7), the transformed grids clearly show that FFD fails to capture strong discontinuity in the vertical direction. However, anisotropic XFFD, with both strong-weak and strong-continuous, results in very similar and seemingly correct transformed grids. For the isotropic weak dataset (Fig. 4.8), no difference can be observed in the transformed grid, even for the FFD registration. In general, it is difficult to observe weak discontinuity in the transformed grid, since the displacement field is continuous and discontinuities only exist in the derivatives of the displacements. In contrast, the strain is computed from the first derivatives of the displacements allowing a much finer evaluation and comparison between the registration with different models.

The volumetric strain fields obtained on the three datasets when registered with different discontinuity types are also shown in Fig. 4.6, 4.7 and 4.8. The corresponding maximum absolute errors are presented in Table 4.2. For each of the datasets, the best result is always given by registration modelled with the XFFD of the corresponding discontinuity type.

In the strong-weak dataset, only the strong-weak XFFD correctly recovers the discontinuity in the strain given by the homogeneous compression in the right-side region (Fig. 4.6).

In the strong-continuous dataset, the homogeneous horizontal compression should result in a constant (continuous) volumetric strain. Strong-continuous XFFD correctly recovers the constant strain, whereas the additional degrees of freedom given by the strong-weak XFFD produce spurious discontinuities in the strain (Fig. 4.7).

In the isotropic weak dataset the discontinuous strain given by the homogenous isotropic expansion in the exterior region and the static state of the interior circle is only correctly recovered by the isotropic weak XFFD (Fig. 4.8).

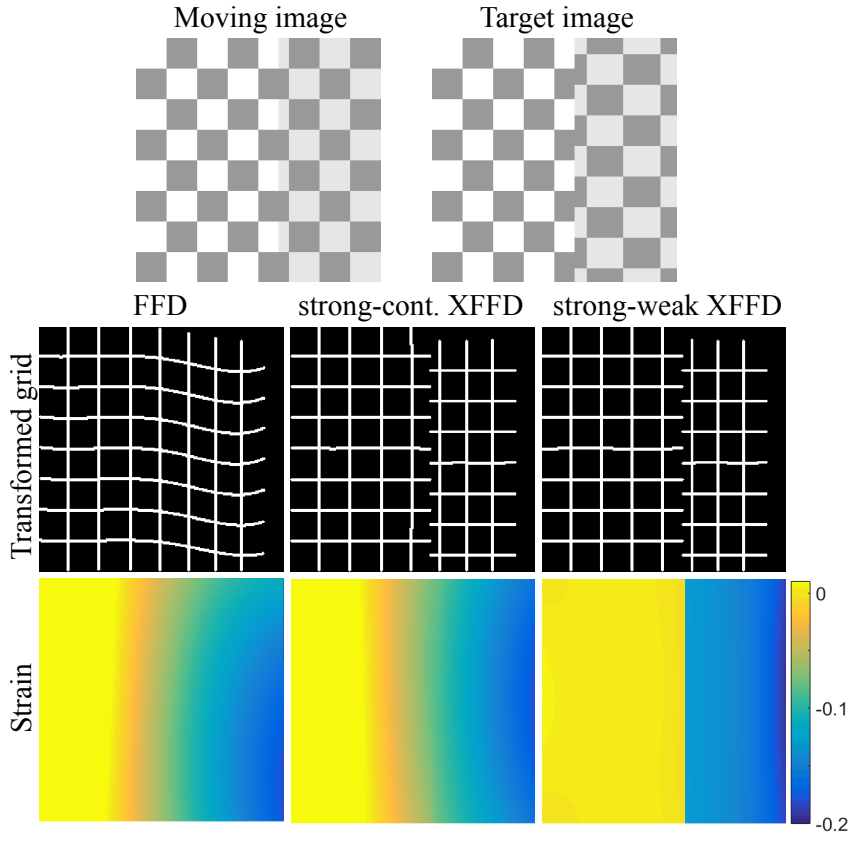

Figure 4.6: Results on strong-weak dataset: transformed grid and volumetric strain of FFD, strong-continuous and strong-weak XFFD. The color map in the strain figure was trimmed to the range [-0.2, 0] for visualisation.

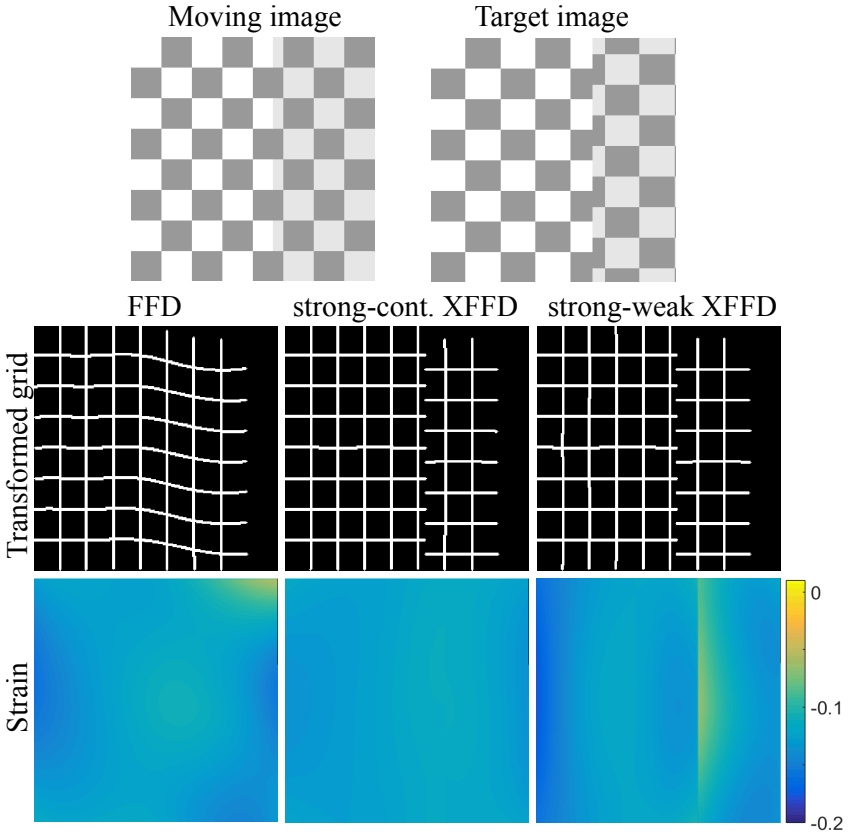

Figure 4.7: Results on strong-continuous dataset: transformed grid and volumetric strain of FFD, strong-continuous and strong-weak XFFD. The color map in the strain figure was trimmed to the range [-0.2,0] for visualisation.

Table 4.2: Maximum error of the volumetric strain for different registration models on the three synthetic datasets with different discontinuity types.

Dataset	FFD	Strong-Cont. XFFD	Strong-Weak XFFD	Weak XFFD
Strong-Cont.	0.0333	**0.0060**	0.0531	0.0598
Strong-Weak	0.1025	0.0958	**0.0079**	0.1771
Weak	0.2150	0.2277	0.1730	**0.0392**

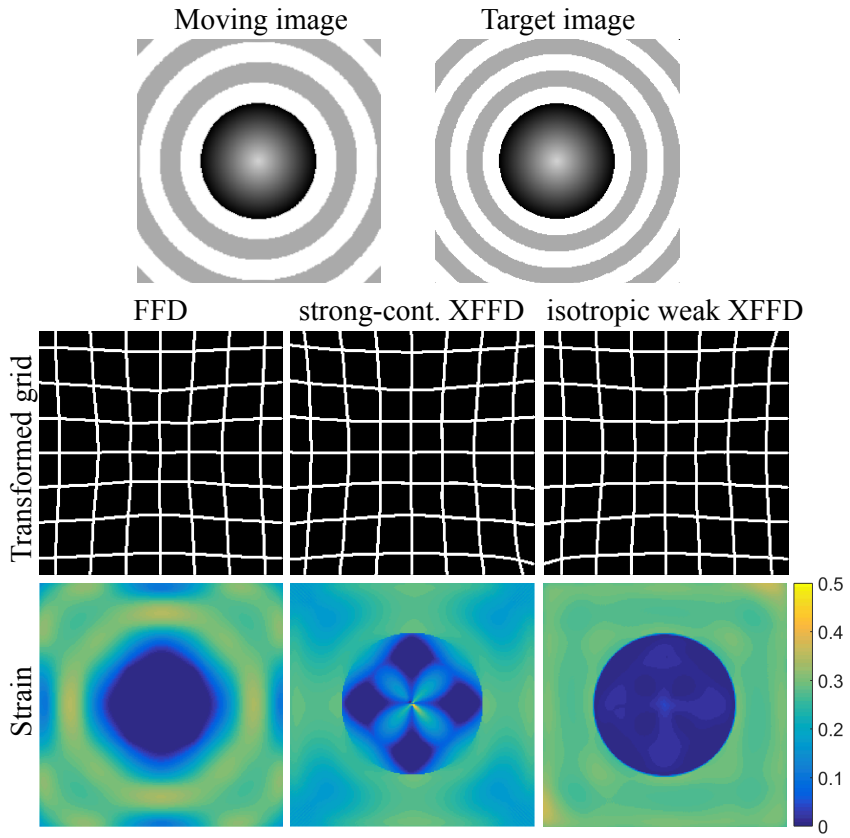

Figure 4.8: Results on isotropic weak dataset: transformed grid and volumetric strain of FFD, strong-continuous and isotropic weak XFFD. The color map in the strain figure was trimmed to the range [0, 0.5] for visualisation.

4.4.2 Experiments on DIR-lab dataset

In the quantitative evaluation on the DIR-lab dataset, the strong-weak XFFD obtained the best results. In terms of TRE (Table 4.3), the isotropic strong XFFD obtained the best results, while the strong-weak XFFD produced slightly better results (1.32 mm in average) than the best results from previous methods [5, 6, 187, 188, 190, 192]. However, only using the TRE is not adequate for evaluating the performance of registration methods in handling discontinuities, since the landmarks are located inside the lungs. Thus, it is important to evaluate the alignment of the region boundaries using gap and overlap volumes. Regarding to this metric (Table 4.4), The isotropic strong XFFD obtained equivalent results to previous methods [5, 6, 192]. But the strong-weak XFFD showed substantial improvement (15.7 mm^3 and 19.1 mm^3 respectively, in average) reducing by 79% and 49% the best results of the previous methods.

Strong-weak XFFD produced better TRE than strong-continuous XFFD, but they were very similar in gap and overlap volumes. They are both able to handle strong discontinuity in the tangential direction properly. However, their difference is more evident in the strain field (Fig. 4.9). The strain showed that strong-weak XFFD correctly captures discontinuity present in the perpendicular strain due to the presence of tissues with different material properties (the rib cage and lungs). In contrast, strong-continuous XFFD failed in that aspect, as much as FFD.

4.5 Discussion

Handling discontinuities in image registration is a challenging problem that have been tackled with limited success. In the literature, most methods on discontinuous registration have been developed for lung images, implicitly or explicitly modelling the discontinuous motion as either isotropic strong [5, 190, 192] or strong-continuous type [6, 187, 188, 207]. However, no previous work provides an explicit discussion and complete modelling of general tissue transitions, nor considers weak discontinuities. In this chapter, anisotropic XFFD is introduced as a general method to handle different types of discontinuities in image registration. In particular, anisotropic XFFD addresses the

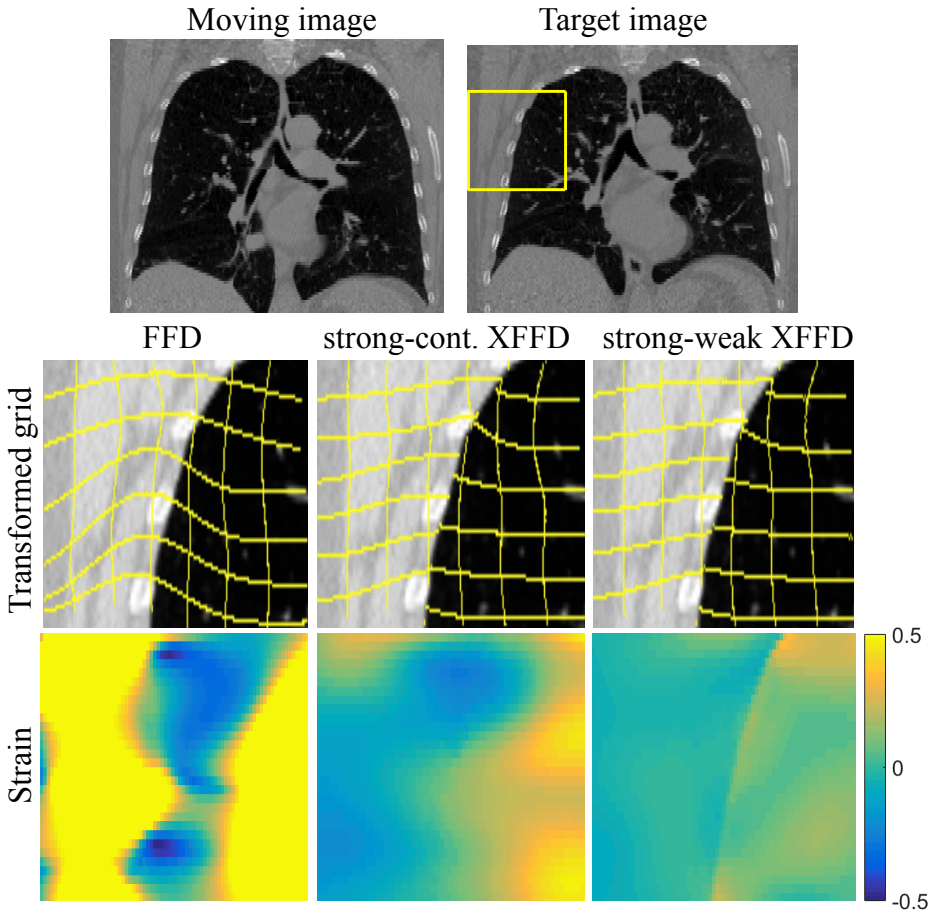

Figure 4.9: Results on DIR-lab dataset: target image with region A defined in yellow box. Zoom-in figures for transformed grid and perpendicular strain in region A. The colour map in the strain figure was trimmed to the range [-0.5, 0.5] for visualisation.

Table 4.3: The mean and standard deviation of TRE (mm) on the DIR-lab dataset

Case	Before registration	Schmidt-Richberg (2012)	Pace (2013)	Papież (2014)	Wu (2008)
1	3.89 ± 2.78	1.22 ± 0.64	1.06 ± 0.57	1.05 ± 0.6	1.1 ± 0.5
2	4.34 ± 3.90	1.14 ± 0.65	1.45 ± 1.00	1.08 ± 0.6	1.0 ± 0.5
3	6.94 ± 4.05	1.36 ± 0.81	1.88 ± 1.35	1.49 ± 0.9	1.3 ± 0.7
4	9.83 ± 4.86	2.68 ± 2.79	2.04 ± 1.40	1.90 ± 1.3	1.5 ± 1.0
5	7.48 ± 5.51	1.57 ± 1.23	2.73 ± 2.13	1.99 ± 1.7	1.9 ± 1.5
6	10.9 ± 6.97	2.21 ± 1.66	2.72 ± 2.04	2.36 ±1.9	1.6 ± 0.9
7	11.0 ± 7.43	3.81 ± 3.06	4.59 ± 3.41	2.32 ± 1.9	1.7 ± 1.1
8	15.0 ± 9.01	3.42 ± 4.25	6.22 ± 5.69	3.58 ± 3.4	1.6 ± 1.4
9	7.92 ± 3.98	1.83 ± 1.19	2.32 ± 1.42	1.74 ± 1.0	1.4 ± 0.8
10	7.30 ± 6.35	2.06 ± 1.92	2.82 ± 2.50	2.02 ± 2.1	1.6 ± 1.2
mean	8.46 ± 5.48	2.13 ± 1.82	2.78 ± 2.96	1.95 ± 0.7	1.47 ± 0.96
Case	Delmon (2013)	Berendsen (2014)	XFFD isotropic strong	XFFD strong-cont.	XFFD strong-weak
1	1.2 ± 0.6	1.00 ± 0.52	1.00 ± 0.51	1.02±0.58	1.02 ± 0.58
2	1.1 ± 0.6	1.02 ± 0.57	0.99 ± 0.59	1.01±0.63	1.02 ± 0.71
3	1.6 ± 0.9	1.14 ± 0.89	1.12 ± 0.64	1.23±0.80	1.23 ± 0.82
4	1.6 ± 1.1	1.46 ± 0.96	1.44 ± 1.03	1.47±1.03	1.46 ± 1.01
5	2.0 ± 1.6	1.61 ± 1.48	1.37 ± 1.35	2.20±3.53	1.58 ± 1.44
6	1.7 ± 1.0	1.42 ± 0.89	1.26 ± 1.04	1.36±0.83	1.39 ± 0.83
7	1.9 ± 1.2	1.49 ± 1.06	1.12 ± 0.67	1.37±0.82	1.39 ± 1.10
8	2.2 ± 2.3	1.62 ± 1.71	1.18 ± 1.22	1.54±1.84	1.53 ± 1.92
9	1.6 ± 0.9	1.30 ± 0.76	1.14 ± 0.64	1.73±0.95	1.38 ± 0.84
10	1.7 ± 1.2	1.50 ± 1.31	1.08± 0.82	1.25±0.78	1.26± 0.80
mean	1.66 ± 1.14	1.36 ± 0.99	1.17 ± 0.85	1.42±1.18	1.32 ± 1.00

Table 4.4: Gap/overlap volumes (mm^3) on the DIR-lab dataset

Case	Wu (2008)	Delmon (2013)	Berendsen (2014)	XFFD isotropic strong	XFFD strong-cont.	XFFD strong-weak
1	38/26	39/15	23/18	39/2	4/5	4/6
2	78/46	67/60	74/34	74/31	15/13	18/13
3	99/28	83/33	57/30	71/24	10/12	9/11
4	75/34	66/44	66/28	92/13	7/6	12/16
5	110/38	78/52	61/32	54/6	11/7	15/13
6	100/86	119/77	130/50	155/11	14/12	27/29
7	105/79	108/7	119/45	138/19	19/16	25/45
8	96/91	92/93	85/53	150/40	26/15	3/2
9	61/34	54/44	70/51	58/14	29/11	12/23
10	120/63	94/56	80/43	109/28	23/13	33/38
mean	88.2/52.5	80.0/55.1	76.5/37.4	94.0/18.8	16.0/11.2	15.7/19.1

dependency of the discontinuity type on the displacement direction with respect to the tissue transition interface.

The experiments on synthetic datasets have demonstrated that anisotropic XFFD is able to correctly model different types of complex tissue transitions. Furthermore, they have illustrated that modelling tissue transitions with the corresponding discontinuity type is significant, showing that incorrect modelling can lead to artefacts in the deformations, especially noticeable in the strain field. In the literature, methods handling discontinuities [5, 6, 187, 188, 190, 192, 207] do not evaluate the strain. However, in order to properly quantify the directions and magnitude of local tissue expansion, this metric is necessary.

The strain reflects local tissue elastic properties and has been employed to evaluate normal and abnormal organ function or kinetics [19–22]. The volumetric strain is the determinant of the Jacobian, which is proportional to local volume change [24]. It is shown that the determinant of Jacobian can be used as a physiologically meaningful parameter to assess the functional capacity of lung tissue [24]. Kaczka *et al.* [25] showed that regional compliances computed from the determinant of Jacobian, can provide unique and complementary information on the mechanical derangements associated with lung injury. In addition, image registration based metrics, such as the Jacobian determinant and maximum principle strain, are shown to be important biomechanical features for the prediction of COPD presence and severity [26].

Anisotropic XFFD was also evaluated on the DIR-lab dataset imaging lung respiratory motion. This dataset exhibits the most complex type of discontinuity, strong-weak, which involves strong discontinuity in the tangential direction and weak discontinuity in the normal direction to the tissue interface. To the best knowledge of the author, this is the first time this type of discontinuity has been correctly modelled. Some previous methods modelled it as strong-continuous, which is a simpler and more constrained model. The evaluation of the strain field showed more evident differences between modelling the tissue transition as strong-weak or strong-continuous. The strong-weak model correctly recovered discontinuity in the strain due to different material properties of the lungs and the rib cage, while the strong-continuous model introduced unreal-

istic compression and expansion near the lung boundary (Fig. 4.9). In this case, strain near the discontinuity interface is artificially smoothed, reducing the strain values of the lung tissue near the boundary and introducing artefacts in the ribs. These errors will adversely affect the clinical conclusions based on parameters computed from strain.

Besides the strain, the accuracy of the registration was measured by TRE and gaps and overlap volumes. In the DIR-lab dataset, since the landmarks are located inside the lungs, TRE evaluates the registration accuracy inside the lungs. Gaps and overlap volumes reflect the registration accuracy near the boundaries when discontinuities are involved. Compared to previous methods handling discontinuities, anisotropic XFFD provided slightly better TRE and significantly smaller gap and overlap volumes.

The registration accuracy is important in clinical applications. For instance, in image-guided radiotherapy, deformable registration can be used to map dose between planning scans and diagnostic scans acquired before radiotherapy. It has been proven that the registration error is correlated with the mapped location error [31], which is associated to side effects of radiotherapy, when normal tissue receives high doses. Cunliffe *et al.* [31] measured the dose alignment accuracy when nonrigid registration is used for dose mapping. They found that the state-of-the-art method MEVIS EMPIRE10 [222] had a TRE of 5.2 mm when the lungs were not masked, since this method did not handle discontinuities. They also discovered that the dose-mapping error increases linearly with the registration error. Thus, the proposed registration framework could be potentially used for this task since it highly reduces the registration error while maintaining good boundary alignment.

4.6 Conclusions

In this chapter, a classification of tissue transitions is presented and the corresponding transformation models have been developed for the corresponding discontinuity types considering their directional dependence. By incorporating such models, XFFD has been extended to a general non-rigid image registration framework for handling all scenarios of tissue transitions.

Anisotropic XFFD is able to handle discontinuities caused by relative motion of non-attached structures (strong discontinuity) and discontinuities due to different material properties of attached structures (weak discontinuity). Moreover, it can model common tissue transitions characterised by anisotropic discontinuity types, in which the behaviour of discontinuities depends on the displacement direction relative to the interface orientation. No previous methods explicitly describe or model these types of discontinuities.

The generality of anisotropic XFFD has been demonstrated on synthetic datasets mimicking various discontinuity types. Its applicability to clinical images has been illustrated on the DIR-lab open dataset, where anisotropic XFFD outperforms all previous registration methods handling discontinuities. The results evidence the importance of adopting the correct discontinuity type in agreement with the physical properties and contact conditions of the tissues involved.

Chapter 5

Conclusions and Outlook

5.1 Overview

Correct modelling of tissue transitions in image registration is important for recovering physically realistic deformations, from which clinical quantities can be estimated for measuring tissue mechanics. An important clinical parameter is the strain, which is used to evaluate organ function towards disease diagnosis [19–22]. Failing to model discontinuities with an appropriate model can introduce artefacts in the resulting deformations and strain, having an adverse impact on the relevant clinical analysis.

In this thesis, a general image registration framework has been developed for handling discontinuities at tissue transitions, named eXtended Free-Form Deformation (XFFD). The XFFD seamlessly integrates within and extends the standard FFD approach. This framework borrows the concept of the interpolation method from the eXtended Finite Element method (XFEM) to incorporate discontinuities by enriching the B-spline basis functions, coupled with extra degrees of freedom. Discontinuities involved in tissue transitions can be classified into different types depending on the physical properties of the tissue transitions: tissue material properties and contact conditions. In addition, tissue transitions can also involve discontinuities with anisotropic properties. XFFD incorporates all types of discontinues including the directional properties to handle different tissue transitions. The proposed framework has been developed in two stages presented in two chapters (Chapter 3, 4), leading to the following

contributions:

- It contains the first study on tissue transition properties in image registration. A classification of discontinuities is proposed based on the physical properties of the tissue transitions.
- This study has led to the development of a set of transformation models within XFFD that can handle all types of discontinuities involved at tissue transitions.
- XFFD is also developed to include directional dependence, which takes into account that the most usual types of tissue transitions involve anisotropic discontinuity properties.

5.2 Conclusions

The XFFD has been tested on a variety of synthetic datasets mimicking different types of tissue transitions and illustrated on a publicly available 3D liver and lung datasets. XFFD produced physically plausible deformations and strain when modelling tissue transitions with a correct model, as observed in the visualisation of transformed grid and strain. In addition, XFFD achieved high performance in the lung dataset, in terms of TRE, which measures registration accuracy inside the lungs, as well as gap and overlap volumes, which measure boundary misalignment of the regions separated by the discontinuity surface.

The XFFD has high registration accuracy and can produce more realistic displacement and strain fields when discontinuities exist. Thus, it can be applied to clinical applications involving discontinuous deformations. For instance, it could be directly applied to dose mapping in radiotherapy planning of lung tumour (Section 1.3). For the construction of biomechanical model of the spine, XFFD can be employed to match CT and MRI images of the spine, since it can properly handle weak discontinuities between IVDs and vertebrae. However, for a further improvement of the resulting deformation field, a rigidity penalty term [130] should be included for bone structures.

Furthermore, it can be used for diagnosis and monitoring of cardiac diseases (Section 1.3). In cardiac images the heart slide along other organs and is always in contact

with the blood, so it can be modelled as strong-weak discontinuity. This application would require the addition of a penalty term to smooth the strain (Section 5.3.1).

A limitation of XFFD is that it requires a segmentation of the target image to describe the location of discontinuities as prior knowledge. This requirement is, however, shared by all the other B-spline based methods [5, 6, 192] and many of the diffusion-based methods [188, 207]. This may be alleviated by using an automatic segmentation method [208–210] as a previous step (Section 5.3.3).

A further limitation of XFFD is that it does not incorporate any prior information on the elasticity properties outside the tissue transitions. This can produce undesirable results especially in the regions where the images lack enough texture to guide the registration. This aspect can be improved by including a penalty term (Section 5.3.3).

5.3 Future lines of research

The work presented in this thesis has opened ways for a variety of lines of research and future developments. Some of the potential research directions are presented in the following.

5.3.1 Simultaneous registration and segmentation framework

The most important limitation of the proposed framework is the requirement of a high quality segmentation of the tissue transition interface in the target image. For the registration of an image sequence, only one segmentation is required. However, a fully automatic method would be more convenient for clinical applications. Although an automatic segmentation can be performed as an initial step, it would be valuable to couple the registration framework with an automatic segmentation.

This task could be achieved by adding a new set of B-spline parameters controlling the deformations of an initial mask to update the segmentation of the fixed image during the registration process. This initial mask does not need to be accurate, but it should partially cover the object of interest.

The main idea of this approach is that the cost function has a minima when the fixed

image and transformed image coincide, and this can only happen if the mask is a perfect segmentation of the fixed image. During the registration process, when the mask does not coincide with the boundary of the object being segmented, this will cause not only the mis-alignment of the images but also high strain of the transformation near the actual tissue interface. The mis-alignment of the images will be handled by the cost of similarity measure. However, it would be necessary to include a penalisation of the strain in the cost function, such as bending energy penalty [128].

The main caveat of this approach is the addition of new degrees of freedom, which will increase the computational complexity and the likelihood of the optimiser being trapped at a local minima. This could potentially be solved using a discrete optimiser [171, 179].

5.3.2 Discrete optimisation

The XFFD registration framework implemented for the development of this thesis adopts LBFGS to find the optimal transformation parameters. LBFGS is a continuous optimiser based on the gradient and an approximated Hessian. Continuous optimisers can provide accurate solutions and they are compatible with most of the previously proposed similarity metrics and transformation models. However, the optimisation process is time-consuming and they might get trapped in a local minima. To solve this issue, discrete optimisers can serve as an alternative, as they are much faster than continuous optimisers and can find the global minimum or a solution close to it. However, their accuracy is limited by the search space and they are not directly compatible with other existing components of registration, often requiring reformulation of the cost function.

Notwithstanding, the current enriched B-splines could be used in the frameworks proposed in [171, 179]. These two methods produce continuous displacements and they require a very dense grid to mimic discontinuous motion. Since these two methods employ B-splines to restrict the possible deformations, the modification would be to change the B-spline parameterisation to include its enriched counterpart. The advantage of this modification over the two previous methods [171, 179] would be twofolds:

the modified framework would not require a very dense grid, since discontinuities are properly handled, and it would produce more realistic displacement and strain fields when discontinuities are involved.

5.3.3 Penalising inhomogeneous strain

Correct modelling of discontinuities is key to producing realistic displacement and strain fields. Even without an accurate information on the material properties of tissues involved, it is expected that, under normal conditions, homogeneous regions present continuous and smooth strains. However, regions with homogeneous intensities lack texture to guide the registration process, resulting in high uncertainties. The proposed framework does not impose any extra constraint on the behaviour of the transformation, which is only optimised for matching the image intensities. Thus, this can lead to inhomogeneous strain in such regions. To achieve more physically plausible strain, a smoothness penalty term could be included.

In the literature, the bending energy penalty term [128] is commonly employed to smooth the strain field by penalising large values in the second derivatives of the transformation. Thus, it could be extended in the XFFD framework by deriving the second derivatives of the enriched B-splines.

5.3.4 Diffeomorphic temporal XFFD

The XFFD is a flexible framework, which allows the inclusion of any other extension of FFD that have been proposed in the past, such as diffeomorphic registration [128] and sparse FFD [47]. Especially, temporal registration can provide more accurate motion analysis by including temporal information. XFFD can be extended to handle temporal deformations by including enriched B-spline basis in the Temporal Diffeomorphic Free Form Deformation (TDFFD) [3]. In this framework, the velocity field is modelled by B-splines defined on a 4D control point grid. The velocities are described by 3D B-spline basis weighted by 1D B-spline function in the temporal dimension and the displacements are computed by the integral of the velocities with respect to time. Thus, the enriched basis functions in XFFD can be plugged in to replace the 3D B-spline

basis to incorporate discontinuities.

Bibliography

[1] Markelj P., Tomaževič D., Likar B., and Pernuš F., "A review of 3D/2D registration methods for image-guided interventions," *Medical Image Analysis*, vol. 16, no. 3, pp. 642–661, 2012.

[2] Rueckert D. and Aljabar P., "Nonrigid registration of medical images: Theory, methods, and applications," *Signal Processing Magazine, IEEE*, vol. 27, no. 4, pp. 113–119, 2010.

[3] De Craene M., Piella G., Camara O., Duchateau N., Silva E., Doltra A., D'hooge J., Brugada J., Sitges M., and Frangi A. F., "Temporal diffeomorphic free-form deformation: Application to motion and strain estimation from 3D echocardiography," *Medical Image Analysis*, vol. 16, no. 2, pp. 427–450, 2012.

[4] Aljabar P., *Tracking longitudinal change using MR image data*, Ph.D. thesis, Imperial College London, 2007.

[5] Wu Z., Rietzel E., Boldea V., Sarrut D., and Sharp G. C., "Evaluation of deformable registration of patient lung 4DCT with subanatomical region segmentations," *Medical Physics*, vol. 35, no. 2, pp. 775–781, 2008.

[6] Delmon V., Rit S., Pinho R., and Sarrut D., "Registration of sliding objects using direction dependent B-splines decomposition," *Physics in Medicine and Biology*, vol. 58, no. 5, pp. 1303–1314, 2013.

[7] Dawn S., Saxena V., and Sharma B., "Remote sensing image registration techniques: A survey," in *International Conference on Image and Signal Processing*. Springer, 2010, pp. 103–112.

[8] Zitova B. and Flusser J., "Image registration methods: a survey," *Image and Vision Computing*, vol. 21, no. 11, pp. 977–1000, 2003.

[9] Hajnal J. V., Hill D. L. G., and Hawkes D. J., Eds., *Medical image registration*, Biomedical Engineering Series. CRC Press, Boca Raton, 2001.

[10] James A. P. and Dasarathy B. V., "Medical image fusion: A survey of the state of the art," *Information Fusion*, vol. 19, pp. 4–19, 2014.

[11] Dickie D. A., Job D. E., Gonzalez D. R., Shenkin S. D., and Wardlaw J. M., "Use of brain MRI atlases to determine boundaries of age-related pathology: the importance of statistical method," *PloS One*, vol. 10, no. 5, pp. e0127939, 2015.

[12] Aljabar P., Heckemann R. A., Hammers A., Hajnal J. V., and Rueckert D., "Multi-atlas based segmentation of brain images: atlas selection and its effect on accuracy," *Neuroimage*, vol. 46, no. 3, pp. 726–738, 2009.

[13] Nokhodchi A. and Martin G. P., *Pulmonary Drug Delivery: Advances and Challenges*, John Wiley & Sons, 2015.

[14] Gorbunova V., Sporring J., Lo P., Loeve M., Tiddens H. A., Nielsen M., Dirksen A., and de Bruijne M., "Mass preserving image registration for lung CT," *Medical Image Analysis*, vol. 16, no. 4, pp. 786–795, 2012.

[15] Maintz J. A. and Viergever M. A., "A survey of medical image registration," *Medical Image Analysis*, vol. 2, no. 1, pp. 1–36, 1998.

[16] Broit C., *Optimal registration of deformed images*, Ph.D. thesis, University of Pennsylvania, 1981.

[17] Christense G. E., Rabbitt R. D., and Miller M. I., "Deformable templates using large deformation kinematics," *IEEE Transactions on Image Processing*, vol. 5, no. 10, pp. 1435–1447, 1996.

[18] Rueckert D., Sonoda , LukeI., Hayes C., Hill , DerekL. G., Leach M. O., and Hawkes D. J., "Nonrigid registration using free-form deformations: application

to breast MR images," *IEEE Transactions on Medical Imaging*, vol. 18, no. 8, pp. 712–721, 1999.

[19] Mirsky I., "Assessment of passive elastic stiffness of cardiac muscle: mathematical concepts, physiologic and clinical considerations, directions of future research," *Progress in Cardiovascular Diseases*, vol. 18, no. 4, pp. 277–308, 1976.

[20] Urheim S., Edvardsen T., Torp H., Angelsen B., and Smiseth O. A., "Myocardial strain by Doppler echocardiography validation of a new method to quantify regional myocardial function," *Circulation*, vol. 102, no. 10, pp. 1158–1164, 2000.

[21] Chiumello D., Carlesso E., Cadringher P., Caironi P., Valenza F., Polli F., Tallarini F., Cozzi P., Cressoni M., Colombo A., and others , "Lung stress and strain during mechanical ventilation for acute respiratory distress syndrome," *American Journal of Respiratory and Critical Care Medicine*, vol. 178, no. 4, pp. 346–355, 2008.

[22] Hirsch S., Klatt D., Freimann F., Scheel M., Braun J., and Sack I., "In vivo measurement of volumetric strain in the human brain induced by arterial pulsation and harmonic waves," *Magnetic Resonance in Medicine*, vol. 70, no. 3, pp. 671–683, 2013.

[23] Castillo R., Castillo E., Guerra R., Johnson V. E., McPhail T., Garg A. K., and Guerrero T., "A framework for evaluation of deformable image registration spatial accuracy using large landmark point sets," *Physics in Medicine and Biology*, vol. 54, no. 7, pp. 1849–1870, 2009.

[24] Reinhardt J. M., Ding K., Cao K., Christensen G. E., Hoffman E. A., and Bodas S. V., "Registration-based estimates of local lung tissue expansion compared to xenon CT measures of specific ventilation," *Medical image analysis*, vol. 12, no. 6, pp. 752–763, 2008.

[25] Kaczka D. W., Cao K., Christensen G. E., Bates J. H., and Simon B. A., "Analysis of regional mechanics in canine lung injury using forced oscillations and 3D image registration," *Annals of biomedical engineering*, vol. 39, no. 3, pp. 1112–1124, 2011.

[26] Bodduluri S., Newell J. D., Hoffman E. A., and Reinhardt J. M., "Registration-based lung mechanical analysis of chronic obstructive pulmonary disease (COPD) using a supervised machine learning framework," *Academic radiology*, vol. 20, no. 5, pp. 527–536, 2013.

[27] Amelon R., Cao K., Ding K., Christensen G. E., Reinhardt J. M., and Raghavan M. L., "Three-dimensional characterization of regional lung deformation," *Journal of biomechanics*, vol. 44, no. 13, pp. 2489–2495, 2011.

[28] Elen A., Choi H. F., Loeckx D., Gao H., Claus P., Suetens P., Maes F., and D'hooge J., "Three-dimensional cardiac strain estimation using spatio-temporal elastic registration of ultrasound images: A feasibility study," *IEEE transactions on medical imaging*, vol. 27, no. 11, pp. 1580–1591, 2008.

[29] Gao H., Allan A., McComb C., Luo X., and Berry C., "Left ventricular strain and its pattern estimated from cine CMR and validation with DENSE," *Physics in medicine and biology*, vol. 59, no. 13, pp. 3637, 2014.

[30] Duchateau N., De Craene M., Piella G., Silva E., Doltra A., Sitges M., Bijnens B. H., and Frangi A. F., "A spatiotemporal statistical atlas of motion for the quantification of abnormal myocardial tissue velocities," *Medical image analysis*, vol. 15, no. 3, pp. 316–328, 2011.

[31] Cunliffe A. R., Contee C., Armato S. G., White B., Justusson J., Malik R., and Al-Hallaq H. A., "Effect of deformable registration on the dose calculated in radiation therapy planning CT scans of lung cancer patients," *Medical physics*, vol. 42, no. 1, pp. 391–399, 2015.

[32] Weiss E., Wijesooriya K., Dill S. V., and Keall P. J., "Tumor and normal tissue motion in the thorax during respiration: Analysis of volumetric and positional

variations using 4D CT," *International Journal of Radiation Oncology* Biology* Physics*, vol. 67, no. 1, pp. 296–307, 2007.

[33] Castro-Mateos I., Pozo J. M., Lazary A., and Frangi A. F., "Automatic construction of patient-specific finite-element mesh of the spine from IVDs and vertebra segmentations," in *SPIE Medical Imaging*. International Society for Optics and Photonics, 2016, pp. 97881U–97881U.

[34] Brown L. G., "A survey of image registration techniques," *ACM computing surveys (CSUR)*, vol. 24, no. 4, pp. 325–376, 1992.

[35] Oliveira F. P. and Tavares J. M. R., "Medical image registration: a review," *Computer Methods in Biomechanics and Biomedical Engineering*, , no. ahead-of-print, pp. 1–21, 2012.

[36] Sotiras A., Davatzikos C., and Paragios N., "Deformable medical image registration: A survey," *IEEE Transactions on Medical Imaging*, vol. 32, no. 7, pp. 1153–1190, 2013.

[37] Modersitzki J., *Numerical methods for image registration*, Oxford University Press on Demand, 2004.

[38] Pelizzari C. A., Chen G. T., Spelbring D. R., Weichselbaum R. R., and Chen C.-T., "Accurate three-dimensional registration of CT, PET, and/or MR images of the brain," *Journal of Computer Assisted Tomography*, vol. 13, no. 1, pp. 20–26, 1989.

[39] Hill D. L., Hawkes D. J., Crossman J., Gleeson M., Cox T., Bracey E., Strong A., and Graves P., "Registration of MR and CT images for skull base surgery using point-like anatomical features," *The British Journal of Radiology*, vol. 64, no. 767, pp. 1030–1035, 1991.

[40] Sauer F., "Image registration: enabling technology for image guided surgery and therapy," in *IEEE Engineering in Medicine and Biology 27th Annual Conference*. IEEE, 2006, pp. 7242–7245.

[41] Rao A., Sanchez-Ortiz G. I., Chandrashekara R., Lorenzo-Valdés M., Mohiaddin R., and Rueckert D., "Construction of a cardiac motion atlas from MR using non-rigid registration," in *International Workshop on Functional Imaging and Modeling of the Heart*. Springer, 2003, pp. 141–150.

[42] Pluim J. P. W., Maintz J. B. A., and Viergever M. A., "Mutual-information-based registration of medical images: a survey," *IEEE Transactions on Medical Imaging*, vol. 22, no. 8, pp. 986–1004, 2003.

[43] Castro-Mateos I., Pozo J. M., Cootes T. F., Wilkinson J. M., Eastell R., and Frangi A. F., "Statistical shape and appearance models in osteoporosis," *Current osteoporosis reports*, vol. 12, no. 2, pp. 163–173, 2014.

[44] Lorenzo-Valdés M., Sanchez-Ortiz G. I., Mohiaddin R., and Rueckert D., "Atlas-based segmentation and tracking of 3D cardiac MR images using non-rigid registration," in *International Conference on Medical Image Computing and Computer-Assisted Intervention*. Springer, 2002, pp. 642–650.

[45] Rohlfing T., Brandt R., Maurer C., and Menzel R., "Bee brains, B-splines and computational democracy: Generating an average shape atlas," in *IEEE Workshop on Mathematical Methods in Biomedical Image Analysis*. IEEE, 2001, pp. 187–194.

[46] Wang H., Suh J. W., Das S. R., Pluta J. B., Craige C., and Yushkevich P. A., "Multi-atlas segmentation with joint label fusion," *IEEE Transactions on Pattern Analysis and Machine Intelligence*, vol. 35, no. 3, pp. 611–623, 2013.

[47] Shi W., Zhuang X., Wang H., Duckett S., Luong D. V., Tobon-Gomez C., Tung K., Edwards P. J., Rhode K. S., Razavi R. S., and others , "A comprehensive cardiac motion estimation framework using both untagged and 3-D tagged MR images based on nonrigid registration," *IEEE Transactions on Medical Imaging*, vol. 31, no. 6, pp. 1263–1275, 2012.

[48] Boldea V., Sharp G. C., Jiang S. B., and Sarrut D., "4D-CT lung motion estimation with deformable registration: quantification of motion nonlinearity and hysteresis," *Medical Physics*, vol. 35, no. 3, pp. 1008–1018, 2008.

[49] Vandemeulebroucke J., Rit S., Kybic J., Clarysse P., and Sarrut D., "Spatiotemporal motion estimation for respiratory-correlated imaging of the lungs," *Medical Physics*, vol. 38, no. 1, pp. 166–178, 2011.

[50] Hunt S. A., Abraham W. T., Chin M. H., Feldman A. M., Francis G. S., Ganiats T. G., Jessup M., Konstam M. A., Mancini D. M., Michl K., and others , "ACC/AHA 2005 guideline update for the diagnosis and management of chronic heart failure in the adult a report of the American College of Cardiology/American Heart Association Task Force on Practice Guidelines (Writing Committee to Update the 2001 Guidelines for the Evaluation and Management of Heart Failure): developed in collaboration with the American College of Chest Physicians and the International Society for Heart and Lung Transplantation: endorsed by the Heart Rhythm Society," *Circulation*, vol. 112, no. 12, pp. e154–e235, 2005.

[51] Crum W. R., Hartkens T., and Hill D. L. G., "Non-rigid image registration: theory and practice," *British Journal of Radiology*, vol. 77, no. suppl 2, pp. S140–S153, 2004.

[52] Holden M., "A review of geometric transformations for nonrigid body registration," *IEEE Transactions on Medical Imaging*, vol. 27, no. 1, pp. 111–128, 2008.

[53] Bhatia K. K., *Analysis of the developing brain using image registration*, Ph.D. thesis, Imperial College London, 2007.

[54] Bajcsy R. and Kovačič S., "Multiresolution elastic matching," *Computer vision, Graphics, and Image Processing*, vol. 46, no. 1, pp. 1–21, 1989.

[55] Davatzikos C., "Spatial transformation and registration of brain images using elastically deformable models," *Computer Vision and Image Understanding*, vol. 66, no. 2, pp. 207–222, 1997.

[56] Rabbitt R. D., Weiss J. A., Christensen G. E., and Miller M. I., "Mapping of hyperelastic deformable templates using the finite element method," in *SPIE's 1995 International Symposium on Optical Science, Engineering, and Instrumentation*. International Society for Optics and Photonics, 1995, pp. 252–265.

[57] Droske M. and Rumpf M., "A variational approach to nonrigid morphological image registration," *SIAM Journal on Applied Mathematics*, vol. 64, no. 2, pp. 668–687, 2004.

[58] Pennec X., Stefanescu R., Arsigny V., Fillard P., and Ayache N., "Riemannian elasticity: A statistical regularization framework for non-linear registration," in *International Conference on Medical Image Computing and Computer-Assisted Intervention*. Springer, 2005, pp. 943–950.

[59] Burger M., Modersitzki J., and Ruthotto L., "A hyperelastic regularization energy for image registration," *SIAM Journal on Scientific Computing*, vol. 35, no. 1, pp. B132–B148, 2013.

[60] Bro-Nielsen M. and Gramkow C., "Fast fluid registration of medical images," in *Visualization in Biomedical Computing*. Springer, 1996, pp. 265–276.

[61] Lester H., Arridge S. R., Jansons K. M., Lemieux L., Hajnal J. V., and Oatridge A., "Non-linear registration with the variable viscosity fluid algorithm," in *Biennial International Conference on Information Processing in Medical Imaging*. Springer, 1999, pp. 238–251.

[62] Beg M. F., Miller M. I., Trouvé A., and Younes L., "Computing large deformation metric mappings via geodesic flows of diffeomorphisms," *International Journal of Computer Vision*, vol. 61, no. 2, pp. 139–157, 2005.

[63] Arsigny V., Commowick O., Pennec X., and Ayache N., "A log-euclidean framework for statistics on diffeomorphisms," *Medical Image Computing and Computer-Assisted Intervention–MICCAI 2006*, pp. 924–931, 2006.

[64] Vercauteren T., Pennec X., Perchant A., and Ayache N., "Symmetric log-domain diffeomorphic registration: A demons-based approach," *Medical Image Computing and Computer-Assisted Intervention–MICCAI 2008*, pp. 754–761, 2008.

[65] Thirion J. P., "Image matching as a diffusion process: an analogy with Maxwell's demons," *Medical Image Analysis*, vol. 2, no. 3, pp. 243–260, 1998.

[66] Horn B. K. and Schunck B. G., "Determining optical flow," *Artificial Intelligence*, vol. 17, no. 1, pp. 185–203, 1981.

[67] Lucas B. D., Kanade T., and others , "An iterative image registration technique with an application to stereo vision.," in *IJCAI*, 1981, vol. 81, pp. 674–679.

[68] Pennec X., Cachier P., and Ayache N., "Understanding the ''Demons's algorithm": 3D non-rigid registration by gradient descent," in *MICCAI*. Springer, 1999, pp. 597–605.

[69] Vercauteren T., Pennec X., Perchant A., and Ayache N., "Diffeomorphic demons: Efficient non-parametric image registration," *NeuroImage*, vol. 45, no. 1, pp. S61–S72, 2009.

[70] Stefanescu R., Pennec X., and Ayache N., "Grid powered nonlinear image registration with locally adaptive regularization," *Medical Image Analysis*, vol. 8, no. 3, pp. 325–342, 2004.

[71] Mansi T., Pennec X., Sermesant M., Delingette H., and Ayache N., "iLogDemons: a Demons-based registration algorithm for tracking incompressible elastic biological tissues," *International Journal of Computer Vision*, vol. 92, no. 1, pp. 92–111, 2011.

[72] Arad N., Dyn N., Reisfeld D., and Yeshurun Y., "Image warping by radial basis functions: application to facial expressions," *CVGIP: Graphical Models and Image Processing*, vol. 56, no. 2, pp. 161–172, 1994.

[73] Ruprecht D. and Müller H., "Free form deformation with scattered data interpolation methods," in *Geometric Modelling*, pp. 267–281. Springer, 1993.

[74] Bookstein F. L., "Thin-plate splines and the atlas problem for biomedical images," in *Biennial International Conference on Information Processing in Medical Imaging*. Springer, 1991, pp. 326–342.

[75] Yang X., Xue Z., Liu X., and Xiong D., "Topology preservation evaluation of compact-support radial basis functions for image registration," *Pattern Recognition Letters*, vol. 32, no. 8, pp. 1162–1177, 2011.

[76] Li J., Yang X., and Yu J., "Compact support thin plate spline algorithm," *Journal of Electronics (China)*, vol. 24, no. 4, pp. 515–522, 2007.

[77] Rohr K. and Wörz S., "An extension of thin-plate splines for image registration with radial basis functions," in *IEEE International Symposium on Biomedical Imaging (ISBI)*. IEEE, 2012, pp. 442–445.

[78] Rohr K., Stiehl H. S., Sprengel R., Beil W., Buzug T. M., Weese J., and Kuhn M., "Point-based elastic registration of medical image data using approximating thin-plate splines," in *Visualization in Biomedical Computing*. Springer, 1996, pp. 297–306.

[79] Rohr K., Stiehl H. S., Sprengel R., Buzug T. M., Weese J., and Kuhn M., "Landmark-based elastic registration using approximating thin-plate splines," *IEEE Transactions on Medical Imaging*, vol. 20, no. 6, pp. 526–534, 2001.

[80] Zagorchev L. and Goshtasby A., "A comparative study of transformation functions for nonrigid image registration," *IEEE Transactions on Image Processing*, vol. 15, no. 3, pp. 529–538, 2006.

[81] Davis M. H., Khotanzad A., Flamig D. P., and Harms S. E., "A physics-based coordinate transformation for 3-D image matching," *IEEE Transactions on Medical Imaging*, vol. 16, no. 3, pp. 317–328, 1997.

[82] Kohlrausch J., Rohr K., and Stiehl H. S., "A new class of elastic body splines for nonrigid registration of medical images," *Journal of Mathematical Imaging and Vision*, vol. 23, no. 3, pp. 253–280, 2005.

[83] Wörz S. and Rohr K., "Physics-based elastic registration using non-radial basis functions and including landmark localization uncertainties," *Computer Vision and Image Understanding*, vol. 111, no. 3, pp. 263–274, 2008.

[84] Barr A. H., "Global and local deformations of solid primitives," *ACM Siggraph Computer Graphics*, vol. 18, no. 3, pp. 21–30, 1984.

[85] Sederberg T. W. and Parry S. R., "Free-form deformation of solid geometric models," in *ACM SIGGRAPH computer graphics*. ACM, 1986, vol. 20, pp. 151–160.

[86] Feldmar J., Malandain G., Declerck J., and Ayache N., "Extension of the ICP algorithm to non-rigid intensity-based registration of 3D volumes," in *Proceedings of the Workshop on Mathematical Methods in Biomedical Image Analysis*. IEEE, 1996, pp. 84–93.

[87] Declerck J., Feldmar J., Goris M. L., and Betting F., "Automatic registration and alignment on a template of cardiac stress and rest reoriented SPECT images," *IEEE Transactions on Medical Imaging*, vol. 16, no. 6, pp. 727–737, 1997.

[88] Bankman I. N., *Handbook of Medical Image Processing and Analysis*, Academic Press, 2009.

[89] Tustison N. J. and Amini A. A., "Biventricular myocardial strains via nonrigid registration of AnFigatomical NURBS models," *IEEE Transactions on Medical Imaging*, vol. 25, no. 1, pp. 94–112, 2006.

[90] Wang J. and Jiang T., "Nonrigid registration of brain MRI using NURBS," *Pattern Recognition Letters*, vol. 28, no. 2, pp. 214–223, 2007.

[91] Tustison N. J., Avants B. B., and Gee J. C., "Directly manipulated free-form deformation image registration," *IEEE Transactions on Image Processing*, vol. 18, no. 3, pp. 624–635, 2009.

[92] Schnabel J. A., Rueckert D., Quist M., Blackall J. M., Castellano-Smith A. D., Hartkens T., Penney G. P., Hall W. A., Liu H., Truwit C. L., and others , "A generic framework for non-rigid registration based on non-uniform multi-level free-form deformations," in *MICCAI*. Springer, 2001, pp. 573–581.

[93] Shi W., Jantsch M., Aljabar P., Pizarro L., Bai W., Wang H., O'Regan D., Zhuang X., and Rueckert D., "Temporal sparse free-form deformations," *Medical Image Analysis*, vol. 17, no. 7, pp. 779–789, 2013.

[94] Ledesma-Carbayo M. J., Kybic J., Desco M., Santos A., Suhling M., Hunziker P., and Unser M., "Spatio-temporal nonrigid registration for ultrasound cardiac motion estimation," *IEEE Transactions on Medical Imaging*, vol. 24, no. 9, pp. 1113–1126, 2005.

[95] Chandrashekara R., Mohiaddin R., and Rueckert D., "Cardiac motion tracking in tagged MR images using a 4D B-spline motion model and nonrigid image registration," in *Biomedical Imaging: Nano to Macro, 2004. IEEE International Symposium on*. IEEE, 2004, pp. 468–471.

[96] De Craene M., Tobon-Gomez C., Butakoff C., Duchateau N., Piella G., Rhode K. S., and Frangi A. F., "Temporal diffeomorphic free form deformation (TDFFD) applied to motion and deformation quantification of tagged MRI sequences," in *STACOM*, pp. 68–77. Springer, 2012.

[97] Arsigny V., Pennec X., and Ayache N., "Polyrigid and polyaffine transformations: a novel geometrical tool to deal with non-rigid deformations–application to the registration of histological slices," *Medical image analysis*, vol. 9, no. 6, pp. 507–523, 2005.

[98] Arsigny V., Commowick O., Ayache N., and Pennec X., "A fast and log-euclidean polyaffine framework for locally linear registration," *Journal of Mathematical Imaging and Vision*, vol. 33, no. 2, pp. 222–238, 2009.

[99] McLeod K., Sermesant M., Beerbaum P., and Pennec X., "Spatio-temporal tensor decomposition of a polyaffine motion model for a better analysis of patho-

logical left ventricular dynamics," *IEEE transactions on medical imaging*, vol. 34, no. 7, pp. 1562–1575, 2015.

[100] Modat M., *Efficient Dense Non-Rigid Registration using the Free-Form Deformation Framework*, Phd thesis, University College London., 2012.

[101] Viola P. and Wells III W. M., "Alignment by maximization of mutual information," *International Journal of Computer Vision*, vol. 24, no. 2, pp. 137–154, 1997.

[102] Hajnal J. V., Saeed N., Oatridge A., Williams E. J., Young I. R., and Bydder G. M., "Detection of subtle brain changes using subvoxel registration and subtraction of serial MR images," *Journal of Computer Assisted Tomography*, vol. 19, no. 5, pp. 677–691, 1995.

[103] Hajnal J. V., Saeed N., Soar E. J., Oatridge A., Young I. R., and Bydder G. M., "A registration and interpolation procedure for subvoxel matching of serially acquired MR images," *Journal of Computer Assisted Tomography*, vol. 19, no. 2, pp. 289–296, 1995.

[104] Kim J. and Fessler J. A., "Intensity-based image registration using robust correlation coefficients," *IEEE Transactions on Medical Imaging*, vol. 23, no. 11, pp. 1430–1444, 2004.

[105] Avants B. B., Epstein C. L., Grossman M., and Gee J. C., "Symmetric diffeomorphic image registration with cross-correlation: evaluating automated labeling of elderly and neurodegenerative brain," *Medical Image Analysis*, vol. 12, no. 1, pp. 26–41, 2008.

[106] Shannon C. E. and Weaver W., "The mathematical theory of communication," *Reprinted with corrections from The Bell System Technical Journal*, vol. 27, pp. 379–423, 623–656, 1948.

[107] Collignon A., Maes F., Delaere D., Vandermeulen D., Suetens P., and Marchal G., "Automated multi-modality image registration based on information theory," in *Information Processing in Medical Imaging*, 1995, vol. 3, pp. 263–274.

[108] Collignon A., *Multi-modality medical image registration by maximization of mutual information*, Ph.D. thesis, Catholic University of Leuven, 1998.

[109] Viola P. and Wells III W. M., "Alignment by maximization of mutual information," in *International Conference on Computer Vision*. IEEE Computer Society Press, 1995, pp. 16–23.

[110] Wells W. M., Viola P., Atsumi H., Nakajima S., and Kikinis R., "Multi-modal volume registration by maximization of mutual information," *Medical Image Analysis*, vol. 1, no. 1, pp. 35–51, 1996.

[111] Studholme C., Hill D. L., and Hawkes D. J., "An overlap invariant entropy measure of 3D medical image alignment," *Pattern Recognition*, vol. 32, no. 1, pp. 71–86, 1999.

[112] Hermosillo G., Chefd'Hotel C., and Faugeras O., "Variational methods for multimodal image matching," *International Journal of Computer Vision*, vol. 50, no. 3, pp. 329–343, 2002.

[113] Karaçali B., "Information theoretic deformable registration using local image information," *International Journal of Computer Vision*, vol. 72, no. 3, pp. 219–237, 2007.

[114] Studholme C., Drapaca C., Iordanova B., and Cardenas V., "Deformation-based mapping of volume change from serial brain MRI in the presence of local tissue contrast change," *IEEE Transactions on Medical Imaging*, vol. 25, no. 5, pp. 626–639, 2006.

[115] Sundar H., Shen D., Biros G., Xu C., and Davatzikos C., "Robust computation of mutual information using spatially adaptive meshes," in *International Conference on Medical Image Computing and Computer-Assisted Intervention*. Springer, 2007, pp. 950–958.

[116] Loeckx D., Slagmolen P., Maes F., Vandermeulen D., and Suetens P., "Nonrigid image registration using conditional mutual information," *IEEE Transactions on Medical Imaging*, vol. 29, no. 1, pp. 19–29, 2010.

[117] Zhuang X., Arridge S., Hawkes D. J., and Ourselin S., "A nonrigid registration framework using spatially encoded mutual information and free-form deformations," *IEEE Transactions on Medical Imaging*, vol. 30, no. 10, pp. 1819–1828, 2011.

[118] Pluim J. P., Maintz J. A., and Viergever M. A., "Image registration by maximization of combined mutual information and gradient information," in *International Conference on Medical Image Computing and Computer-Assisted Intervention*. Springer, 2000, pp. 452–461.

[119] Rueckert D., Clarkson M., Hill D., and Hawkes D. J., "Non-rigid registration using higher-order mutual information," in *Medical Imaging 2000*. International Society for Optics and Photonics, 2000, pp. 438–447.

[120] Russakoff D. B., Tomasi C., Rohlfing T., and Maurer Jr C. R., "Image similarity using mutual information of regions," in *European Conference on Computer Vision*. Springer, 2004, pp. 596–607.

[121] Studholme C., Hill D., and Hawkes D., "Incorporating connected region labelling into automated image registration using mutual information," in *Mathematical Methods in Biomedical Image Analysis, 1996., Proceedings of the Workshop on*. IEEE, 1996, pp. 23–31.

[122] Knops Z. F., Maintz J. A., Viergever M. A., and Pluim J. P., "Registration using segment intensity remapping and mutual information," in *International Conference on Medical Image Computing and Computer-Assisted Intervention*. Springer, 2004, pp. 805–812.

[123] D'Agostino E., Maes F., Vandermeulen D., and Suetens P., "An information theoretic approach for non-rigid image registration using voxel class probabilities," *Medical Image Analysis*, vol. 10, no. 3, pp. 413–431, 2006.

[124] Yi Z. and Soatto S., "Multimodal registration via spatial-context mutual information," in *Biennial International Conference on Information Processing in Medical Imaging*. Springer, 2011, pp. 424–435.

[125] Heinrich M. P., Jenkinson M., Bhushan M., Matin T., Gleeson F. V., Brady M., and Schnabel J. A., "MIND: Modality independent neighbourhood descriptor for multi-modal deformable registration," *Medical Image Analysis*, vol. 16, no. 7, pp. 1423–1435, 2012.

[126] Lee D., Hofmann M., Steinke F., Altun Y., Cahill N. D., and Scholkopf B., "Learning similarity measure for multi-modal 3D image registration," in *IEEE Conference on Computer Vision and Pattern Recognition, CVPR*. IEEE, 2009, pp. 186–193.

[127] Bronstein M. M., Bronstein A. M., Michel F., and Paragios N., "Data fusion through cross-modality metric learning using similarity-sensitive hashing.," in *CVPR*. San Francisco, CA, 2010, vol. 1, p. 5.

[128] Rueckert D., Aljabar P., Heckemann R. A., Hajnal J. V., and Hammers A., "Diffeomorphic registration using B-splines," in *International Conference on Medical Image Computing and Computer-Assisted Intervention*. Springer, 2006, pp. 702–709.

[129] Loeckx D., Maes F., Vandermeulen D., and Suetens P., "Nonrigid image registration using free-form deformations with a local rigidity constraint," in *International Conference on Medical Image Computing and Computer-Assisted Intervention*. Springer, 2004, pp. 639–646.

[130] Staring M., Klein S., and Pluim J. P., "A rigidity penalty term for nonrigid registration," *Medical Physics*, vol. 34, no. 11, pp. 4098–4108, 2007.

[131] Libertiaux V., Pascon F., and Cescotto S., "Experimental verification of brain tissue incompressibility using digital image correlation," *Journal of the mechanical behavior of biomedical materials*, vol. 4, no. 7, pp. 1177–1185, 2011.

[132] Rohlfing T., Maurer C. R., Bluemke D. A., and Jacobs M. A., "Volume-preserving nonrigid registration of MR breast images using free-form deformation with an incompressibility constraint," *IEEE Transactions on Medical Imaging*, vol. 22, no. 6, pp. 730–741, 2003.

[133] Rueckert D., Frangi A. F., and Schnabel J. A., "Automatic construction of 3-D statistical deformation models of the brain using nonrigid registration," *IEEE Transactions on Medical Imaging*, vol. 22, no. 8, pp. 1014–1025, 2003.

[134] Loeckx D., Maes F., Vandermeulen D., and Suetens P., "Non-rigid image registration using a statistical spline deformation model," in *Biennial International Conference on Information Processing in Medical Imaging*. Springer, 2003, pp. 463–474.

[135] Xue Z., Shen D., and Davatzikos C., "Statistical representation of high-dimensional deformation fields with application to statistically constrained 3D warping," *Medical Image Analysis*, vol. 10, no. 5, pp. 740–751, 2006.

[136] Albrecht T., Luthi M., and Vetter T., "A statistical deformation prior for non-rigid image and shape registration," in *Computer Vision and Pattern Recognition, 2008. CVPR 2008. IEEE Conference on*. IEEE, 2008, pp. 1–8.

[137] Berendsen F. F., Van Der Heide U. A., Langerak T. R., Kotte A. N., and Pluim J. P., "Free-form image registration regularized by a statistical shape model: application to organ segmentation in cervical MR," *Computer Vision and Image Understanding*, vol. 117, no. 9, pp. 1119–1127, 2013.

[138] Chong E. K. and Zak S. H., *An introduction to optimization*, vol. 76, John Wiley & Sons, 2013.

[139] Bazaraa M. S., Sherali H. D., and Shetty C. M., *Nonlinear programming: theory and algorithms*, John Wiley & Sons, 2013.

[140] Luenberger D. G., *Introduction to linear and nonlinear programming*, vol. 28, Addison-Wesley Reading, MA, 1973.

[141] Klein S., Staring M., and Pluim J. P., "Evaluation of optimization methods for nonrigid medical image registration using mutual information and B-splines," *IEEE Transactions on Image Processing*, vol. 16, no. 12, pp. 2879–2890, 2007.

[142] Grippo L., Lampariello F., and Lucidi S., "A nonmonotone line search technique for Newton's method," *SIAM Journal on Numerical Analysis*, vol. 23, no. 4, pp. 707–716, 1986.

[143] Moré J. J. and Thuente D. J., "Line search algorithms with guaranteed sufficient decrease," *ACM Transactions on Mathematical Software (TOMS)*, vol. 20, no. 3, pp. 286–307, 1994.

[144] Press W. H., *Numerical recipes 3rd edition: The art of scientific computing*, Cambridge university press, 2007.

[145] Kiefer J., Wolfowitz J., and others , "Stochastic estimation of the maximum of a regression function," *The Annals of Mathematical Statistics*, vol. 23, no. 3, pp. 462–466, 1952.

[146] Spall J. C., "Multivariate stochastic approximation using a simultaneous perturbation gradient approximation," *IEEE Transactions on Automatic Control*, vol. 37, no. 3, pp. 332–341, 1992.

[147] Robbins H. and Monro S., "A stochastic approximation method," *The Annals of Mathematical Statistics*, pp. 400–407, 1951.

[148] Klein S., Pluim J. P., Staring M., and Viergever M. A., "Adaptive stochastic gradient descent optimisation for image registration," *International Journal of Computer Vision*, vol. 81, no. 3, pp. 227–239, 2009.

[149] Fletcher R. and Reeves C. M., "Function minimization by conjugate gradients," *The Computer Journal*, vol. 7, no. 2, pp. 149–154, 1964.

[150] Polak E. and Ribiere G., "Note sur la convergence de méthodes de directions conjuguées," *Revue française d'informatique et de recherche opérationnelle, série rouge*, vol. 3, no. 1, pp. 35–43, 1969.

[151] Polyak B. T., "The conjugate gradient method in extremal problems," *USSR Computational Mathematics and Mathematical Physics*, vol. 9, no. 4, pp. 94–112, 1969.

[152] Hestenes M. R. and Stiefel E., *Methods of conjugate gradients for solving linear systems*, vol. 49, NBS, 1952.

[153] Hager W. W. and Zhang H., "A survey of nonlinear conjugate gradient methods," *Pacific Journal of Optimization*, vol. 2, no. 1, pp. 35–58, 2006.

[154] Nocedal J. and Wright S., *Numerical optimization*, Springer Science & Business Media, 2006.

[155] Powell M. J., "Convergence properties of algorithms for nonlinear optimization," *Siam Review*, vol. 28, no. 4, pp. 487–500, 1986.

[156] Nocedal J., "Updating quasi-Newton matrices with limited storage," *Mathematics of Computation*, vol. 35, no. 151, pp. 773–782, 1980.

[157] Byrd R. H., Lu P., Nocedal J., and Zhu C., "A limited memory algorithm for bound constrained optimization," *SIAM Journal on Scientific Computing*, vol. 16, no. 5, pp. 1190–1208, 1995.

[158] De Craene M., Camara O., Bijnens B. H., and Frangi A. F., "Large diffeomorphic FFD registration for motion and strain quantification from 3D-US sequences," in *Functional Imaging and Modeling of the Heart*, pp. 437–446. Springer, 2009.

[159] Qiao Y., Sun Z., Lelieveldt B. P., and Staring M., "A Stochastic Quasi-Newton method for non-rigid image registration," in *International Conference on Medical Image Computing and Computer-Assisted Intervention*. Springer, 2015, pp. 297–304.

[160] Wang C., Komodakis N., and Paragios N., "Markov random field modeling, inference & learning in computer vision & image understanding: A survey," *Computer Vision and Image Understanding*, vol. 117, no. 11, pp. 1610–1627, 2013.

[161] Boykov Y. and Kolmogorov V., "An experimental comparison of min-cut/max-flow algorithms for energy minimization in vision," *IEEE transactions on Pattern Analysis and Machine Intelligence*, vol. 26, no. 9, pp. 1124–1137, 2004.

[162] Tang T. W. and Chung A. C., "Non-rigid image registration using graph-cuts," in *International Conference on Medical Image Computing and Computer-Assisted Intervention*. Springer, 2007, pp. 916–924.

[163] Lawler E. L., *Combinatorial optimization: networks and matroids*, Courier Corporation, 2001.

[164] So R. W. and Chung A. C., "Multi-level non-rigid image registration using graph-cuts," in *2009 IEEE International Conference on Acoustics, Speech and Signal Processing*. IEEE, 2009, pp. 397–400.

[165] So R. W. and Chung A. C., "Non-rigid image registration by using graph-cuts with mutual information," in *2010 IEEE International Conference on Image Processing*. IEEE, 2010, pp. 4429–4432.

[166] So R. W., Tang T. W., and Chung A. C., "Non-rigid image registration of brain magnetic resonance images using graph-cuts," *Pattern Recognition*, vol. 44, no. 10, pp. 2450–2467, 2011.

[167] Pearl J., *Probabilistic reasoning in intelligent systems: networks of plausible inference*, Morgan Kaufmann, 2014.

[168] Yang Q., Wang L., and Ahuja N., "A constant-space belief propagation algorithm for stereo matching," in *IEEE Conference on Computer Vision and Pattern Recognition (CVPR)*. IEEE, 2010, pp. 1458–1465.

[169] Heinrich M. P., Jenkinson M., Brady J. M., and Schnabel J. A., "Non-rigid image registration through efficient discrete optimization.," in *MIUA*, 2011, pp. 187–192.

[170] Komodakis N., Tziritas G., and Paragios N., "Fast, approximately optimal solutions for single and dynamic MRFs," in *2007 IEEE Conference on Computer Vision and Pattern Recognition*. IEEE, 2007, pp. 1–8.

[171] Glocker B., Komodakis N., Tziritas G., Navab N., and Paragios N., "Dense image registration through MRFs and efficient linear programming," *Medical Image Analysis*, vol. 12, no. 6, pp. 731–741, 2008.

[172] Glocker B., Sotiras A., Komodakis N., and Paragios N., "Deformable medical image registration: Setting the state of the art with discrete methods," *Annual Review of Biomedical Engineering*, vol. 13, pp. 219–244, 2011.

[173] Komodakis N. and Tziritas G., "Approximate labeling via graph cuts based on linear programming," *IEEE Transactions on Pattern Analysis and Machine Intelligence*, vol. 29, no. 8, pp. 1436–1453, 2007.

[174] Glocker B., Komodakis N., Paragios N., Glaser C., Tziritas G., and Navab N., "Primal/dual linear programming and statistical atlases for cartilage segmentation," in *International Conference on Medical Image Computing and Computer-Assisted Intervention*. Springer, 2007, pp. 536–543.

[175] Glocker B., Komodakis N., Navab N., Tziritas G., and Paragios N., "Dense registration with deformation priors," in *International Conference on Information Processing in Medical Imaging*. Springer, 2009, pp. 540–551.

[176] Sotiras A., Neji R., Deux J.-F., Komodakis N., Fleury G., and Paragios N., "A kernel-based graphical model for diffusion tensor registration," in *2010 IEEE International Symposium on Biomedical Imaging: From Nano to Macro*. IEEE, 2010, pp. 524–527.

[177] Sotiras A. and Paragios N., "Discrete symmetric image registration," in *IEEE International Symposium on Biomedical Imaging (ISBI)*. IEEE, 2012, pp. 342–345.

[178] Sotiras A., Komodakis N., Glocker B., Deux J.-F., and Paragios N., "Graphical models and deformable diffeomorphic population registration using global and local metrics," in *International Conference on Medical Image Computing and Computer-Assisted Intervention*. Springer, 2009, pp. 672–679.

[179] Heinrich M. P., Jenkinson M., Papież B. W., Glesson F. V., Brady M., and Schnabel J. A., "Edge-and detail-preserving sparse image representations for deformable registration of chest MRI and CT volumes," in *Information Processing in Medical Imaging*. Springer, 2013, pp. 463–474.

[180] Heinrich M. P., Simpson I. J., Papież B. W., Brady M., and Schnabel J. A., "Deformable image registration by combining uncertainty estimates from supervoxel belief propagation," *Medical Image Analysis*, vol. 27, pp. 57–71, 2016.

[181] Klein S., Staring M., Murphy K., Viergever M. A., and Pluim J. P., "Elastix: a toolbox for intensity-based medical image registration," *IEEE Transactions on Medical Imaging*, vol. 29, no. 1, pp. 196–205, 2010.

[182] Modat M., Ridgway G. R., Taylor Z. A., Lehmann M., Barnes J., Hawkes D. J., Fox N. C., and Ourselin S., "Fast free-form deformation using graphics processing units," *Computer Methods and Programs in Biomedicine*, vol. 98, no. 3, pp. 278–284, 2010.

[183] Modat M., Vercauteren T., Ridgway G. R., Hawkes D. J., Fox N. C., and Ourselin S., "Diffeomorphic demons using normalized mutual information, evaluation on multimodal brain MR images," in *SPIE Medical Imaging*. International Society for Optics and Photonics, 2010, pp. 76232K–76232K.

[184] Shen J.-K., Matuszewski B. J., Shark L.-K., Skalski A., Zielinski T., and Moore C. J., "Deformable image registration-a critical evaluation: Demons, B-Spline FFD and Spring Mass System," in *Fifth International Conference on BioMedical Visualization, MEDIVIS'08*. IEEE, 2008, pp. 77–82.

[185] Piella G., De Craene M., Butakoff C., Grau V., Yao C., Nedjati-Gilani S., Penney G. P., and Frangi A. F., "Multiview diffeomorphic registration: Application to motion and strain estimation from 3D echocardiography," *Medical Image Analysis*, vol. 17, no. 3, pp. 348–364, 2013.

[186] Lu H., Reyes M., Serifovic A., Šerifović A., Weber S., Sakurai Y., Yamagata H., and Cattin P. C., "Multi-modal diffeomorphic demons registration based on point-wise mutual information," in *2010 IEEE International Symposium on Biomedical Imaging: From Nano to Macro*. IEEE, 2010, pp. 372–375.

[187] Schmidt-Richberg A., Werner R., Handels H., and Ehrhardt J., "Estimation of slipping organ motion by registration with direction-dependent regularization," *Medical Image Analysis*, vol. 16, no. 1, pp. 150–159, 2012.

[188] Pace D. F., Aylward S. R., and Niethammer M., "A locally adaptive regularization based on anisotropic diffusion for deformable image registration of sliding organs," *IEEE Transactions on Medical Imaging*, vol. 32, no. 11, pp. 2114–2126, 2013.

[189] Ruan D., Esedoglu S., and Fessler J. A., "Discriminative sliding preserving regularization in medical image registration," in *IEEE International Symposium on Biomedical Imaging (ISBI)*. IEEE, 2009, pp. 430–433.

[190] Papież B. W., Heinrich M. P., Fehrenbach J., Risser L., and Schnabel J. A., "An implicit sliding-motion preserving regularisation via bilateral filtering for deformable image registration," *Medical Image Analysis*, vol. 18, no. 8, pp. 1299–1311, 2014.

[191] Pace D., Enquobahrie A., Yang H., Aylward S., and Niethammer M., "Deformable image registration of sliding organs using anisotropic diffusive regularization," in *IEEE International Symposium on Biomedical Imaging: From Nano to Macro*. IEEE, 2011, pp. 407–413.

[192] Berendsen F. F., Kotte A. N., Viergever M. A., and Pluim J. P., "Registration of organs with sliding interfaces and changing topologies," in *SPIE Medical Imaging*. International Society for Optics and Photonics, 2014, pp. 90340E–90340E.

[193] Unser M., Aldroubi A., and Eden M., "B-spline signal processing. I. Theory," *IEEE Transactions on Signal Processing*, vol. 41, no. 2, pp. 821–833, 1993.

[194] Unser M., Aldroubi A., and Eden M., "B-spline signal processing. II. Efficiency design and applications," *IEEE Transactions on Signal Processing*, vol. 41, no. 2, pp. 834–848, 1993.

[195] Forsey D. R. and Bartels R. H., "Hierarchical B-spline refinement," in *ACM Transitions on Computer Graphics*. ACM, 1988, vol. 22, pp. 205–212.

[196] Ibanez L., Schroeder W., Ng L., and Cates J., "The ITK software guide," 2003.

[197] Fries T. and Belytschko T., "The extended/generalized finite element method: an overview of the method and its applications," *International Journal for Numerical Methods in Engineering*, vol. 84, no. 3, pp. 253–304, 2010.

[198] Hua R., Pozo J. M., Taylor Z. A., and Frangi A. F., "Discontinuous nonrigid registration using extended free-form deformations," in *SPIE Medical Imaging*. International Society for Optics and Photonics, 2015, pp. 94131P–94131P.

[199] Suramo I., Päivänsalo M., and Myllylä V., "Cranio-caudal movements of the liver, pancreas and kidneys in respiration.," *Acta Radiologica: Diagnosis*, vol. 25, no. 2, pp. 129–131, 1983.

[200] Clifford M. A., Banovac F., Levy E., and Cleary K., "Assessment of hepatic motion secondary to respiration for computer assisted interventions," *Computer Aided Surgery*, vol. 7, no. 5, pp. 291–299, 2002.

[201] Siva S., Pham D., Gill S., Bressel M., Dang K., Devereux T., Kron T., and Foroudi F., "An analysis of respiratory induced kidney motion on four-dimensional computed tomography and its implications for stereotactic kidney radiotherapy," *Radiat Oncol*, vol. 8, pp. 248, 2013.

[202] O'Rahilly R. and Müller F., *Basic human anatomy: a regional study of human structure*, WB Saunders Company, 1983.

[203] Penney G. P., Weese J., Little J., Desmedt P., Hill D. L., Hawkes D. J., and others , "A comparison of similarity measures for use in 2-D-3-D medical image registration," *IEEE Transactions on Medical Imaging*, vol. 17, no. 4, pp. 586–595, 1998.

[204] Zhu C., Byrd R. H., Lu P., and Nocedal J., "Algorithm 778: L-BFGS-B: Fortran subroutines for large-scale bound-constrained optimization," *ACM Transactions on Mathematical Software (TOMS)*, vol. 23, no. 4, pp. 550–560, 1997.

[205] Brannon R., "Kinematics: The mathematics of deformation," http://www.mech.utah.edu/ brannon/public/Deformation.pdf, 2008.

[206] Papież B. W., Franklin J., Heinrich M. P., Gleeson F. V., and Schnabel J. A., "Liver motion estimation via locally adaptive over-segmentation regularization," in *International Conference on Medical Image Computing and Computer-Assisted Intervention*. Springer, 2015, pp. 427–434.

[207] Risser L., Vialard F.-X., Baluwala H. Y., and Schnabel J. A., "Piecewise-diffeomorphic image registration: Application to the motion estimation between 3D CT lung images with sliding conditions," *Medical Image Analysis*, vol. 17, no. 2, pp. 182–193, 2013.

[208] Nakagomi K., Shimizu A., Kobatake H., Yakami M., Fujimoto K., and Togashi K., "Multi-shape graph cuts with neighbor prior constraints and its application to lung segmentation from a chest CT volume," *Medical Image Analysis*, vol. 17, no. 1, pp. 62–77, 2013.

[209] Tomoshige S., Oost E., Shimizu A., Watanabe H., and Nawano S., "A conditional statistical shape model with integrated error estimation of the conditions; application to liver segmentation in non-contrast CT images," *Medical Image Analysis*, vol. 18, no. 1, pp. 130–143, 2014.

[210] Rebouças Filho P. P., Cortez P. C., da Silva Barros A. C., Albuquerque V. H. C., and Tavares J. M. R., "Novel and powerful 3D adaptive crisp active contour method applied in the segmentation of CT lung images," *Medical Image Analysis*, vol. 35, pp. 503–516, 2017.

[211] Ehrhardt J. and Lorenz C., *4D modeling and estimation of respiratory motion for radiation therapy*, Springer-Verlag, 2013.

[212] Kim Y. S., Park S. H., Do Ahn S., Lee J. E., Choi E. K., Lee S.-w., Shin S. S., Yoon S. M., and Kim J. H., "Differences in abdominal organ movement between supine and prone positions measured using four-dimensional computed tomography," *Radiotherapy and Oncology*, vol. 85, no. 3, pp. 424–428, 2007.

[213] Xi M., Liu M. Z., Li Q. Q., Cai L., Zhang L., and Hu Y. H., "Analysis of abdominal organ motion using four-dimensional CT," *Chinese Journal of Cancer*, vol. 28, no. 9, pp. 989–993, 2009.

[214] Hua R., Pozo J. M., Taylor Z. A., and Frangi A. F., "Multiresolution eXtended Free-Form Deformations (XFFD) for non-rigid registration with discontinuous transforms," *Medical Image Analysis*, vol. 36, pp. 113–122, 2017.

[215] Sanchez M., Fryazinov O., Fayolle P.-A., and Pasko A., "Convolution filtering of continuous signed distance fields for polygonal meshes," *Computer Graphics Forum*, vol. 34, no. 6, pp. 277–288, 2015.

[216] Virgin W., "Experimental investigations into the physical properties of the intervertebral disc," *Bone & Joint Journal*, vol. 33, no. 4, pp. 607–611, 1951.

[217] Saadé J., Didier A.-L., Villard P.-F., Buttin R., Moreau J.-M., Beuve M., and Shariat B., "A preliminary study for a biomechanical model of the respiratory system," in *Engineering and Computational Sciences for Medical Imaging in Oncology-ECSMIO 2010*, 2010, p. 7.

[218] Chen T., Huang T. S., Yin W., and Zhou X. S., "A new coarse-to-fine framework for 3D brain MR image registration," in *Computer Vision for Biomedical Image Applications*, pp. 114–124. Springer, 2005.

[219] Castillo E., Castillo R., Martinez J., Shenoy M., and Guerrero T., "Four-dimensional deformable image registration using trajectory modeling," *Physics in Medicine and Biology*, vol. 55, no. 1, pp. 305, 2009.

[220] Vandemeulebroucke J., Bernard O., Rit S., Kybic J., Clarysse P., and Sarrut D., "Automated segmentation of a motion mask to preserve sliding motion in deformable registration of thoracic CT," *Medical Physics*, vol. 39, pp. 1006, 2012.

[221] Klein S. and Staring M., "Elastix the manual," Tech. Rep., v4.7, Tech. rep. Utrecht: Image Sciences Institute, University Medical Center, 2014.

[222] Rühaak J., Heldmann S., Kipshagen T., and Fischer B., "Highly accurate fast lung CT registration," in *SPIE Medical Imaging*. International Society for Optics and Photonics, 2013, pp. 86690Y–86690Y.